Searches for the Lightest Supersymmetric Particle at LEP2 when R-parity is violated

Onuora Azubuikeogwu Awunor

Department of Physics
Royal Holloway
University of London.

A thesis submitted to the University of London
for the degree of Doctor of Philosophy.
December, 2002.

Abstract

Searches for the Lightest Supersymmetric Particle (LSP) are performed under the assumption that R-parity is violated via a single dominant $LL\bar{E}$, $LQ\bar{D}$ or $\bar{U}\bar{D}\bar{D}$ coupling. Data collected by the ALEPH detector at LEP with centre-of-mass energies from 189 GeV to 208 GeV and a total integrated luminosity of $628\mathrm{pb}^{-1}$ are used. Searches for direct and indirect decays of pair produced neutralinos and charginos are carried out. In the absence of signal, parameter space of the Minimal Supersymmetric Standard Model is constrained and limits on the mass of the LSP are obtained. Constraints from the Z width measurement, slepton, squark and Higgs searches are also used to exclude parameter space. The lower mass limits for direct decays at 95% confidence on the LSP are $60.2\,\mathrm{GeV}/c^2$, $42.3\,\mathrm{GeV}/c^2$ and $25.9\,\mathrm{GeV}/c^2$ for $LL\bar{E}$, $LQ\bar{D}$ and $\bar{U}\bar{D}\bar{D}$ coupling respectively. The lower mass limits for indirect decays at 95% confidence on the LSP are $58.7\,\mathrm{GeV}/c^2$, $44.2\,\mathrm{GeV}/c^2$ and $42.2\,\mathrm{GeV}/c^2$ for $LL\bar{E}$, $LQ\bar{D}$ and $\bar{U}\bar{D}\bar{D}$ coupling respectively. The limits are valid for all values of μ, $\tan\beta$, m_0 and M_2.

This thesis is dedicated to my father,

Ogbuefi Ucheonye Awunor,

my mother,

Mrs Elizabeth Awunor,

my sisters;

Mrs Nkeiruka Nwabah, Miss Onyebuchi Awunor,

Miss Kikiweji Awunor, Miss Agwunwa Awunor,

and my brothers;

Mr Obichime Awunor and Mr Ikeliakachi Awunor.

Without their support and belief in me, I would not have made it this far.

This thesis is also dedicated to the memory of my brother, Mr. Onyejiuwaka Awunor.

Acknowledgment

The last time I checked, no one said doing a PhD would be easy. Even so, the last three years have been quite brutal. There is no doubt that this journey would never have come to fruition without the help of certain people. They deserve my thanks and gratitude. I would like to thank Professor Michael Green, my supervisor, who, even though allowed me to do pretty much my own thing, did not fail to give me help, direction and criticism when necessary. I consider it a privilege to have been given the opportunity to experience first hand, his guidance and tutelage which can only be the result of decades of experience in the field of Particle Physics. I would also like to thank Dr. David Hutchcroft for his unstinting help and support in my analysis. Without his help there's no doubt I'd still be slugging it out on my analysis. My thanks to Dr. Grahame Blair, Dr. Pedro Teixeira-Dias and Dr. Glen Cowan for the help, support and advice they gave me at various times during the course of my PhD programme. My thanks also to Dr. Simon George, without whose help I'd still be knocking my head against my desktop. My deepest thanks goes to Mrs Denise Keable, an angel in disguise, without whom, I certainly wouldn't have had the financial capability to complete my PhD programme. I would also like to thank the Physics department for paying my tuition fees for the last two years of my programme. Lastly, my thanks to all my colleagues for putting up with me and bringing out the best in me. Every other person not mentioned, consider yourself included in the list.

"To find your center, you must first experience the pain and joy of looking into the abyss.....and realising that what you see is but a reflection - of you. Only then can you let go of fear. Only then will you have the power to shape your destiny."

Onuora Azubuikeogwu Awunor.

Declaration

Onuora Azubuikeogwu Awunor

Contents

List of Figures

List of Tables

Chapter 1

Thesis outline

This thesis describes a number of searches carried out for the Lightest Supersymmetric Particle (LSP) under the assumption that R-parity is violated for decays which occur via a single dominant $LL\bar{E}$, $LQ\bar{D}$ or $\bar{U}\bar{D}\bar{D}$ coupling. Searches were carried out at centre-of-mass energies from 189 GeV to 208 GeV. In the absence of a signal, mass limits were set on the LSP. In this thesis, some of the selection procedures that were used to carry out the analysis were taken from previous searches at lower centre-of-mass energies. Of these procedures, some were modified and all were used to extend the searches to current centre-of-mass energies over a wider range of parameter space. The remaining selections were developed entirely by me.

In chapter 1, a brief history of modern particle physics is given. The theory of supersymmetry and its simplest extension of the Standard Model, called the MSSM, are reviewed. The concept of R-parity and its phenomenological consequences are explained.

In chapter 2, the ALEPH detector is briefly described with emphasis being placed on areas which are important for supersymmetry searches, such as jet finding and identification of leptons. The Standard Model processes relevant to this analysis are introduced and the Monte Carlo programs required for event simulation

are described.

In chapter 3, the current limits on R-parity violating couplings are mentioned. Limits from collider searches are reviewed. Limits from sfermion and gaugino searches and from the measurement of Γ_Z are discussed. These limits play an important role in determining which particles are candidates for the LSP. They also define the mass range that is of interest for searches carried out in chapters 4 through 7.

Chapter 4 explains the technique used for analysis of Monte Carlo signal events, Standard Model processes and data from the ALEPH detector in the search for a signal. The methodology behind the scan of parameter space of the MSSM and the implementation of existing limits to exclude areas of parameter space are described in detail.

Chapter 5 describes the various decay modes and final state topologies arising from decays of gauginos via a single dominant $LL\bar{E}$, $LQ\bar{D}$ or $\bar{U}\bar{D}\bar{D}$ coupling and the various selections used to search for events with these topologies.

In chapter 6, the results on searches for decays via a single dominant $LL\bar{E}$, $LQ\bar{D}$ or $\bar{U}\bar{D}\bar{D}$ coupling are explained. Limits on the mass of the LSP are obtained.

In chapter 7, the results are summarized and conclusions are drawn.

Chapter 2

Theoretical overview

The desire to understand the fundamental laws governing the interaction of particles has been the driving force behind the evolution in theoretical and experimental physics. This evolution had its birth with the proposal of the existence of the atom by the Greeks, and has culminated in modern particle physics as we know it today.

Ground breaking work from theorists and experimentalists alike at the turn of the 20^{th} century saw the amalgamation of two fundamental forces: electricity and magnetism, and the discovery that atoms were composed of a nucleus surrounded by negatively charged particles called electrons. The nucleus was further discovered to consist of a composite of smaller neutral particles called neutrons and charged particles called protons. These were discovered to be made up of still smaller charged particles called quarks. Quarks carry a quantum number called *colour*. Experiments revealed a plethora of particles made up of quark constituents in various colour combinations.

Matter is known to consist of fundamental particles called fermions. The fermions in turn are subdivided into two classes of particles called leptons and quarks. This is illustrated in Table 2.1. The fermions possess internal angular momentum called spin. All fermions have spin in odd multiple integer units of

	Generation	Name	Symbol	Masses (MeV)	charge
Leptons	1^{st}	electron	e	0.511	-1
		e-neutrino	ν_e	$< 3 \times 10^{-6}$	0
	2^{nd}	muon	μ	106	-1
		μ-neutrino	ν_μ	< 0.19	0
	3^{rd}	tau	τ	1780	-1
		τ-neutrino	ν_τ	< 18.2	0
Quarks	1^{st}	up	u	1 - 5	$+\frac{2}{3}$
		down	d	3 - 9	$-\frac{1}{3}$
	2^{nd}	charm	c	$1150 - 1350$	$+\frac{2}{3}$
		strange	s	$75 - 170$	$-\frac{1}{3}$
	3^{rd}	top	t	$174 \times 10^3 \pm 5 \times 10^3$	$+\frac{2}{3}$
		bottom	b	$4 \times 10^3 - 4.4 \times 10^3$	$-\frac{1}{3}$

Table 2.1: Summary of the fundamental particles that make up matter [1].

$\frac{1}{2}\hbar$. Leptons are known to exist in three generations: electrons, muons and taus. The particles in each generation are accompanied by a neutrino. The neutrinos are neutral, almost massless and are weakly interacting. The first generation is stable and makes up the physical existence we *see* around us. The second and third generation particles, with the exception of their associated neutrinos, are less stable and eventually decay into the electron. Each lepton has an anti-lepton partner with opposite charge. Similarly the quarks exist in three generations. Each quark has an anti-quark associated with it possessing the same mass and spin but opposite colour and charge. The masses of the fermions increase from generation to generation.

The interactions between fermions occur by the exchange of particles which can only exist for a brief time under Heisenberg's uncertainty principle $\Delta t \lesssim \frac{\hbar}{\Delta E}$. These particles are called bosons and have integer spin.

It is known that there are four fundamental forces of nature. In the order of weakest to strongest they are: gravity, the weak force, electromagnetism and the strong force. The effect of the gravitational force in the microscopic world is

negligible. The weak force was introduced to explain experimental observations from the radioactive beta-decay of neutrons. Electromagnetism, the force experienced by charged particles, was the result of the amalgamation of electricity and magnetism by Maxwell. In addition to the electromagnetic force and the weak force, the quarks also experience the strong force. The leptons on the other hand, experience the electromagnetic and weak forces but not the strong force. With the knowledge of the complexity of the physical properties governing interactions between the fundamental constituents of matter, came the need for a quantitative calculable system that would be capable of describing, with a set of abstract rules, the laws that govern the interactions between particles. Standard non-relativistic quantum mechanics, which made use of Schrödinger's equation, was limited as it could not handle the creation and annihilation of particles as observed in neutron decays nor were they able to describe the highly relativistic particles encountered in routine cosmic ray experiments. The calculable systems derived to describe the interaction of particles under each of these forces were called gauge theories. Gauge theories are theories that utilize the property of symmetries [2] while at the same time obeying Lorentz invariance. A symmetry is a theory describing an observable such as spin, which is invariant under a set of transformations. Gauge theories in which the parameters are space-time dependent are termed *local* gauge theories. The gauge theory describing interactions between particles via the strong force is called Quantum Chromodynamics (QCD). Here the propagators of the strong force are quanta of the colour field and are called gluons. The gluons couple to the strong force with a coupling strength denoted by α_s. The gauge theory used to describe interactions between particles interacting via the electromagnetic force is called Quantum Electrodynamics (QED). The propagator in this case is the photon and couples to the electromagnetic force with a coupling strength denoted by α. The attempt to explain the observed phenomena of radioactive beta-decay led to

the discovery that the weak force must have weak field quanta which are massive, can be charged or neutral and couple to fermions with a coupling strength, α_W. The attempt to interpret the weak force in terms of a local gauge theory met with disaster since the requirement of local gauge invariance necessitated the existence of massless propagators. While this was compatible with the observed physical properties of the propagators of the electromagnetic and the strong force which had no mass, it was clearly in disagreement with experimental observation in weak force interactions. A way was needed to be found to "give" the propagator mass and at the same time retain the requirement of gauge invariance. This was achieved through the mechanism of *spontaneous symmetry breaking* [3]. Spontaneous symmetry breaking induces the breakdown of gauge symmetries giving rise to the Higgs field which leads to generation of mass for the fermions. The quantum of the Higgs field is a spin-0 particle called the Higgs boson.

The Standard Model [4] is a description of the strong, weak and electromagnetic interactions. It is represented mathematically as

$$SU(3)_C \times SU(2)_L \times U(1)_Y, \tag{2.1}$$

where $SU(3)_C$ and $SU(2)_L \times U(1)_Y$ describe the strong and electroweak forces respectively and C, L and Y represent the colour charge, weak isospin and hypercharge respectively [5]. Electric charge, Q, is related to the third component of weak isospin, T^3, and hypercharge by $Q = T^3 + Y$. The SU(3) symmetry is a special unitary group in three dimensions and is fundamentally represented as a triplet using the colour charges of the quarks. The SU(2) symmetry is a special unitary group in two dimensions and is fundamentally represented as a doublet using the weak isospin of fermions. In the Dirac Lagrangian [2] which describes interactions between fermions, the fermionic fields are split into left-handed and right-handed

components which are projected out by the operation of a Weyl spinor, $\psi = \frac{1\pm\gamma_5}{2}\psi$, where γ^5 is called the chirality operator. The spinor $\psi = \frac{1-\gamma_5}{2}\psi$ projects the left-handed component of the fermion fields and $\psi = \frac{1+\gamma_5}{2}\psi$ the right-handed component. Charged weak interactions are observed to occur only between left-handed fermions, i.e. the W boson only couples to the left-handed fermions and not to the right-handed fermions. The left-handed fermions transform as a doublet under the $SU(2)_L$ symmetry while the right-handed fermions transform as a singlet. In the Standard Model there is no right handed neutrino.

The Standard Model is a well tested theory, but it is not a complete theory [6]. This is made obvious by inconsistencies that become apparent at high energies. The Standard Model is regarded as a low-energy effective theory of a yet-more-fundamental theory. The search for a more complete theory that is consistent at the high energy scale has led to the proposal of a number of models of which *Supersymmetry* is one. The theories of *Technicolour* [7] and employment of large *Extra spatial dimensions*, which allow the lowering of the Planck scale down to the TeV scale [8], are also being considered.

In the next section, the motivation for supersymmetry is reviewed briefly, the essential ideas behind supersymmetry are described and the phenomenological consequences are outlined.

2.1 Supersymmetry

Supersymmetry is a symmetry which transforms bosons into fermions and vice-versa [6]. It predicts that fermions and bosons have partners that have identical properties in all respects except with regards to spin. It is described mathematically by the equation

$$Q\,|\,B\,\rangle = |\,F\,\rangle \;\;;\;\; \overline{Q}\,|\,F\,\rangle = |\,B\,\rangle. \tag{2.2}$$

Here Q represents a spinorial operator, i.e. an operator that generates supersymmetric transformations and obeys anticommutation relations. The conjugate operator is represented by $\bar{Q}$ and is also a spinorial operator. The single-particle states of a supersymmetric theory are arranged into *supermultiplets*. Each supermultiplet contains both fermion and boson states. These states are commonly referred to as superpartners of each other.

Supersymmetry is an attractive theory. Some aesthetic considerations which make this apparent are:

- In the Standard Model, the mass squared of the Higgs particle is subject to quadratic divergences as a result of contributions from couplings to fermions and bosons. This means that fine tuning of Standard Model parameters is required to keep the divergence within acceptable limits. Supersymmetry solves this problem neatly by the introduction of a fermion(boson) counterpart to each boson(fermion) of the Standard Model. This cancels out the quadratic divergences between members of the same multiplet.

- If Supersymmetry is formulated as a local symmetry, then a spin-2 graviton field must be introduced. This leads automatically to supergravity models in which gravity is unified with the strong and electroweak interactions [9].

- In the Standard Model, each group has a coupling constant α_i associated with it. The coupling constants are unrelated at a fundamental level and are scale-dependent through the renormalization group equations [10]. As a result of their scale-dependency, the coupling constants are referred to as *running* coupling constants. In Grand Unified Theories (GUT) [11], which assume that the symmetry groups $SU(3)_C \times SU(2)_L \times U(1)_Y$ are part of a larger

group, G, of which the smallest representation is the SU(5) group [12], the running coupling constants will become equal at some high energy scale. This is due to the fact that the strong coupling constant decreases with increasing energy while the electromagnetic constant increases with increasing energy. Hence at the unification scale, the group, G, has a single coupling constant for all interactions and the observed difference in the couplings at low energy are caused by radiative corrections. GUT predictions show that the proton will decay [13]. However, experimental limits on the proton lifetime require that the GUT scale be above 10^{15} GeV. In the Standard Model, the possibility of coupling unification is excluded as shown in Fig. 2.1. Extrapolation to high energies of the three coupling constants do not meet at a single point. In supersymmetric models, unification is achieved at an energy scale of the order 10^{16} GeV and is in accordance with the requirements imposed by experimental limits from the proton decay. This is because supersymmetry introduces extra parameters which result in a change in the slopes of the running coupling constants.

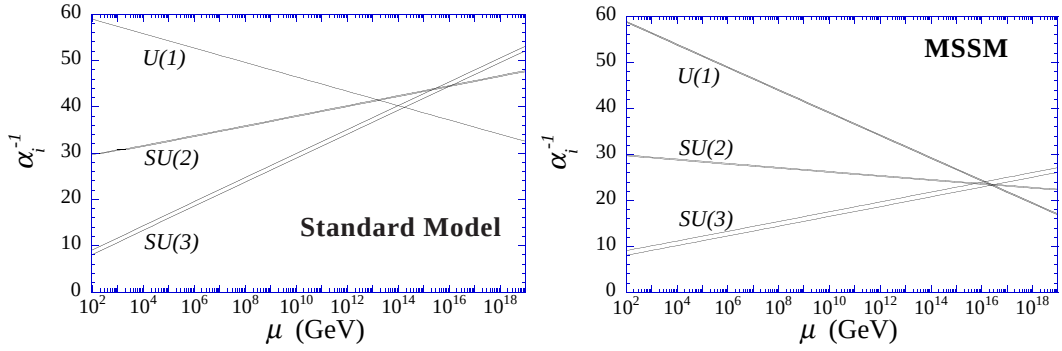

Figure 2.1: The running of the gauge coupling constants in the Standard Model and the Minimal Supersymmetric Standard Model [14].

- Supersymmetry is a necessary ingredient in the formulation of String Theories.

2.2 The Minimal Supersymmetric Standard Model (MSSM)

The Minimal Supersymmetric Standard Model (MSSM) [15] is the simplest supersymmetric extension of the Standard Model. It is renormalizable [16], invariant under the Standard Model gauge group and contains the minimal particle content. The particle content of the Standard Model is extended to include all the supersymmetric partners. Each of the known fundamental particles must be in either a chiral or gauge supermultiplet and have a superpartner with spin differing by 1/2 unit. Only chiral supermultiplets can contain fermions whose left-handed parts transform differently under the gauge group than their right-handed parts. The supersymmetic partners of Standard Model particles are named by placing the letter *s*, which is short for scalar, in front of the particle name, for example, the supersymmetric partners of quarks and leptons are labelled *squarks* and *sleptons*. The left-handed and right-handed states of the quarks and leptons each have their own complex scalar partner. The supersymmetric particle symbols are denoted by placing a tilde over the corresponding Standard Model particle symbol, for example, the superpartners of the left-handed and right-handed parts of the electron field are denoted $\tilde{e}_L$ and $\tilde{e}_R$. The "handedness" here does not refer to the helicity of the selectrons, as they are spin-0 particles, but to that of their superpartners. The same nomenclature applies for the rest of the sfermions. The gauge interactions of each of the slepton and squark fields are the same as for the corresponding Standard Model fermion. For example a left-handed squark such as $\tilde{u}_L$ will couple to the W boson while $\tilde{u}_R$ will not. In the Standard Model the neutrino is always left-handed and as such the superpartner is labelled only with a tilde. The partners of the gauge bosons are spin$-\frac{1}{2}$ *gauginos*. The charginos are the mixed eigenstates of the charged higgsino and the wino, while the neutralinos are the mixed eigen-

state of the photino, zino and neutral higgsino. In Table 2.2 the Standard Model particles and the corresponding superpartners are listed. In Table 2.3 the chiral

Particle	Supersymmetric Partner		
	Sparticle	Interaction Eigenstate	Mass Eigenstate
l	slepton	$\tilde{l}_R, \tilde{l}_L$	$\tilde{l}_1, \tilde{l}_2$
ν	sneutrino	$\tilde{\nu}$	$\tilde{\nu}$
q	squark	$\tilde{q}_R, \tilde{q}_L$	$\tilde{q}_1, \tilde{q}_2$
g	gluino	$\tilde{g}$	$\tilde{g}$
W^+, W^-	wino	$\tilde{W}^+, \tilde{W}^-$	charginos:
H_1^+, H_2^-	higgsino	$\tilde{H}_1^+, \tilde{H}_2^-$	$\tilde{\chi}_1^\pm, \tilde{\chi}_2^\pm$
γ	photino	$\tilde{\gamma}$	neutralinos:
Z	zino	$\tilde{Z}$	$\tilde{\chi}_i^0$
H_1^0, H_2^0	higgsino	$\tilde{H}_1^0, \tilde{H}_2^0$	(i=1,2,3,4)

Table 2.2: A summary of the various particles and their corresponding supersymmetric partners.

supermultiplets of the squarks and sleptons in the MSSM are listed. To break $SU(2)_L \times U(1)_Y$ to $U(1)_{em}$, the mechanism by which the Z and W bosons are given mass whilst keeping γ massless, a Higgs scalar doublet is required. However, such a doublet cannot give mass to the up-type quark in supersymmetry theory because the required term is not invariant under a supersymmetric transformation. Hence, a second doublet $\bar{H}_2$ with hypercharge $+\frac{1}{2}$ is introduced. Since there are two Higgs doublets, each of which has four real scalar fields, the number of degrees of freedom is eight before symmetry breaking. After spontaneous symmetry breaking three of the eight degrees of freedom are absorbed to provide the longitudinal polarisation states for the W^-, W^+ and Z bosons [14, 17]. They are said to have been *eaten* by the W and Z bosons. The remaining five massive Higgs bosons are:

- h^0, H^0: CP even neutral Higgses; h^0 is taken to be the lighter of the two;
- A^0: the CP odd neutral Higgs;
- H^+, H^-: the charged Higgses.

Supermultiplet		spin 0	spin $\frac{1}{2}$
squarks, quarks	Q	$\tilde{u}_L,\ \tilde{d}_L$	$u_L,\ d_L$
$\times 3$ families	$\bar{U}$	$\tilde{u}_R$	u_R
	$\bar{D}$	$\tilde{d}_R$	d_R
sleptons and leptons	L	$\tilde{\nu},\ \tilde{e}_L$	$\nu,\ e_L$
$\times 3$ families	$\bar{E}$	$\tilde{e}_R$	e_R

Table 2.3: Chiral supermultiplets for quarks and leptons in the Minimal Supersymmetric Standard Model. Q and L denote doublet supermultiplets while $\bar{U}$, $\bar{D}$ and $\bar{E}$ denote singlet supermultiplets for quarks and leptons, respectively.

The fermionic partners of the Higgs, the higgsinos, are

- $\tilde{H}_1^0$, $\tilde{H}_2^0$: the neutral higgsinos;
- $\tilde{H}_1^+$, $\tilde{H}_2^-$: the charged higgsinos.

2.2.1 Phenomenological consequences of supersymmetry

If supersymmetry were an unbroken symmetry, the theory predicts that all sparticles would have the same masses as their Standard Model partners. Since no sparticle has yet been discovered, it must be that supersymmetry is a broken symmetry. The uncertainty in phenomenology has led to numerous models with different mass scales at which supersymmetry is broken. This has led to many different predictions for the relations between masses of the sparticles and for the detailed experimental signatures that will be present when they are produced. Whatever model is used to describe supersymmetry breaking, the main constraint is that it should be *soft*, i.e. any additional terms added to the supersymmetric Lagrangian must break supersymmetry explicitly without violating gauge invariance and without introducing quadratically divergent contributions to the scalar masses [5, 18, 19]. Such models contain a number of independent parameters.

- $M_{i=1,2,3}$ denotes gaugino mass terms in the superpotential for SU(1), SU(2) and SU(3) symmetries, where the superpotential is the part of the Lagrangian

that describes the interactions between fermionic and bosonic components of chiral supermultiplets.

- $\tan\beta$ denotes the ratio of the vacuum expectation values (v_2/v_1) of the two Higgs doublets.

- μ is the charged higgsino mixing parameter in the superpotential. It is dimensioned as mass and can be negative.

- m_0 is the common squark and slepton mass at the unification (GUT) scale.

- $A_u,\ A_d$ are trilinear soft supersymmetry-breaking parameters. They determine the L-R squark mixing. They are dimensioned as masses and can be negative.

The terms μ, $\tan\beta$, m_0 and M_i constitute the *parameter space* in this analysis.

2.2.2 Charginos and neutralinos

The chargino mass [13, 20] can be obtained by using the mass terms of the Lagangian describing $SU(2)_L \times U(1)_Y$ charged winos $(\tilde{W}^+,\ \tilde{W}^-)$ and higgsinos $(\tilde{H}^+,\ \tilde{H}^-)$, which can be written as:

$$\mathcal{L}_m = -\frac{1}{2}(\psi^+, \psi^-) \begin{pmatrix} 0 & X^T \\ X & 0 \end{pmatrix} \begin{pmatrix} \psi^+ \\ \psi^- \end{pmatrix} + h.c. \tag{2.3}$$

where

$$X = \begin{pmatrix} M_2 & \sqrt{2}M_W \sin\beta \\ \sqrt{2}M_W cos\beta & \mu \end{pmatrix} \tag{2.4}$$

and $\psi_j^- = (-i\tilde{W}^-, \tilde{H}_2^-),\ \psi_j^+ = (-i\tilde{W}^+, \tilde{H}_2^+)$. The mass matrix is diagonalized using two (2×2) unitary matrices U and V [21] such that $\tilde{\chi}_i^+ = V^{ij}\psi_j^+$ and $\tilde{\chi}_i^- = U^{ij}\psi_j^-$. This yields two mass eigenstates $\tilde{\chi}_1^\pm,\ \tilde{\chi}_2^\pm$, where $\tilde{\chi}_1^\pm$ is the lighter of the two states.

Similarly, the neutralino mass can be obtained [22] by using mass terms in the Lagrangian describing $SU(2)_L \times U(1)_Y$ neutral gauginos ($\tilde{\gamma},\ \tilde{Z}$) and higgsinos ($\tilde{H_1^0},\ \tilde{H_2^0}$) which can be written as

$$\mathcal{L}_m = -1/2(\psi_i^0)^T Y^{ij} \psi_j^0 + h.c. \tag{2.5}$$

In the basis that $\psi_i^0 = (-i\tilde{\gamma}, -i\tilde{Z}, \tilde{H_1^0},\ \tilde{H_2^0})$, Eq. (2.5) can be expanded to give

$$\begin{pmatrix} \tilde{\gamma} & \tilde{Z} & \tilde{H_1^0} & \tilde{H_2^0} \end{pmatrix} \begin{pmatrix} M_1 & 0 & & \\ 0 & M_2 & \multicolumn{2}{c}{\mathbf{M_{mix}}} \\ & & 0 & -\mu \\ \multicolumn{2}{c}{\mathbf{M_{mix}^T}} & -\mu & 0 \end{pmatrix} \begin{pmatrix} \tilde{\gamma} \\ \tilde{Z} \\ \tilde{H_1^0} \\ \tilde{H_2^0} \end{pmatrix}, \tag{2.6}$$

where $\mathbf{M_{mix}}$ is a 2×2 matrix given by

$$\mathbf{M_{mix}} = \begin{pmatrix} -M_Z \cos\beta \sin\theta_W & M_Z \sin\beta \sin\theta_W \\ M_Z \cos\beta \cos\theta_W & -M_Z \sin\beta \cos\theta_W \end{pmatrix}. \tag{2.7}$$

Here θ_W is the weak mixing angle while $\mathbf{M_{mix}^T}$ denotes the transpose of $\mathbf{M_{mix}}$. Diagonalization reveals four mass eigenstates $\tilde{\chi}_i^0$, where $i = 1, 2, 3, 4$ and $\tilde{\chi}_1^0$ is defined as the lightest eigenstate. M_1 and M_2 are commonly assumed to be unified at the GUT scale. They are related through the renormalization group equations at the electroweak scale [18] by the equation

$$M_1 = \frac{\alpha_1(M_Z)}{\alpha_2(M_Z)} M_2 = \frac{5}{3} \tan^2\theta_W M_2, \tag{2.8}$$

where α_1 and α_2 are the coupling constants for the U(1) and SU(2) gauge symmetries respectively.

Using the renormalization group equations, the mass splittings between the left and right physical states of the squarks and sleptons can be calculated down to the

weak scale [23]. The following formulae are valid for all fermions excluding the top quark.

$$m^2_{\tilde{d}_L} = m_0^2 + 6.50 m_{1/2}^2 + M_Z^2 \cos 2\beta (\frac{1}{2} - \frac{1}{3}\sin^2\theta_W) \quad (2.9)$$

$$m^2_{\tilde{d}_R} = m_0^2 + 6.00 m_{1/2}^2 + M_Z^2 \cos 2\beta \frac{1}{3}\sin^2\theta_W \quad (2.10)$$

$$m^2_{\tilde{u}_L} = m_0^2 + 6.50 m_{1/2}^2 - M_Z^2 \cos 2\beta (\frac{1}{2} - \frac{2}{3}\sin^2\theta_W) \quad (2.11)$$

$$m^2_{\tilde{u}_R} = m_0^2 + 6.10 m_{1/2}^2 - M_Z^2 \cos 2\beta \frac{2}{3}\sin^2\theta_W \quad (2.12)$$

$$m^2_{\tilde{l}_L} = m_0^2 + 0.52 m_{1/2}^2 + M_Z^2 \cos 2\beta (\frac{1}{2} - \sin^2\theta_W) \quad (2.13)$$

$$m^2_{\tilde{l}_R} = m_0^2 + 0.15 m_{1/2}^2 + M_Z^2 \cos 2\beta \sin^2\theta_W \quad (2.14)$$

$$m^2_{\tilde{\nu}} = m_0^2 + 0.52 m_{1/2}^2 - M_Z^2 \frac{1}{2}\cos 2\beta, \quad (2.15)$$

where $m_{1/2}$ is the common gaugino mass term at the unification scale.

At the electroweak scale, the three gaugino masses, $M_{i=1,2,3}$, diverge. In this analysis, exclusion limits are quoted in terms of M_2 which is directly related to the physical neutralino masses as explained in section 2.2.2. M_2 and $m_{1/2}$ are related by

$$m_{1/2} = \frac{\alpha_{unification} \cdot \sin^2\theta_W}{\alpha_{em}} M_2 \sim \frac{1}{0.81} \cdot M_2, \quad (2.16)$$

where $\alpha_{unification}$ is the coupling at unification scale and is assumed to be 1/24, and α_{em} is the electromagnetic coupling and is evaluated at the scale of interest. The numerical value is obtained at the electroweak scale ($\sim M_W$). M_1 is given in terms of M_2 by Eq. 2.8. The gluino is described by M_3, which is $\approx 2.7 m_{1/2}$ [13] due to strong interactions, and so is too heavy to play a role in the phenomenology at low energies.

2.3 R-parity

R-parity is a discrete multiplicative symmetry [24]. It is described by the equation

$$R_p = (-1)^{3B+L+2S}, \tag{2.17}$$

where B denotes the baryon number, L the lepton number and S the spin. Standard Model particles have an R-parity value of $+1$. In supersymmetry this is altered because of the presence of scalars carrying non-zero values of B and L, and supersymmetric particles have an R-parity value of -1.

When extending the Standard Model with supersymmetry, the particle field content is doubled to accommodate the superpartners and an additional Higgs doublet superfield is added. The minimal symmetries required to construct the Lagrangian are the gauge symmetry of the Standard Model: $SU(3)_C \times SU(2)_L \times U(1)_Y$ and supersymmetry. The most general superpotentials describing these symmetries are given by

$$W = W_{MSSM} + W_{\not R_P}, \tag{2.18}$$

where

$$\begin{aligned} W_{MSSM} &= h^e_{ij} L_i H_1 \bar{E}_j + h^d_{ij} Q_i H_1 \bar{D}_j + h^u_{ij} Q_i H_2 \bar{U}_j + \mu H_1 H_2, \\ W_{\not R_P} &= \lambda_{ijk} L_i L_j \bar{E}_k + \lambda'_{ijk} L_i Q_j \bar{D}_k + \lambda''_{ijk} \bar{U}_i \bar{D}_j \bar{D}_k. \end{aligned} \tag{2.19}$$

Here $i, j = 1, 2, 3$ are generation indices and a summation is implied. $L_i(Q_i)$ are the lepton (quark) $SU(2)_L$ doublet superfields. $\bar{E}_j$ ($\bar{D}_j, \bar{U}_j$) are the electron (down/up-quark) $SU(2)_L$ singlet superfields. λ, λ' and λ'' are Yukawa couplings. The first term in $W_{\not R_p}$ is anti-symmetric in $\{i, j\}$ and the third term is anti-symmetric in $\{j, k\}$ [25]. The expansion into the Yukawa couplings of the $LL\bar{E}$ and $LQ\bar{D}$ terms

yields:

$$\mathcal{L}_{LL\bar{E}} = \lambda_{ijk}[\tilde{\nu}^i_L e^j_L \bar{e}^k_R + \nu^i_L \tilde{e}^j_L \bar{e}^k_R + (\bar{\nu}^i_L)^c e^j_L \tilde{e}^{k*}_R - (\tilde{e}^i_L \nu^j_L \bar{e}^k_R + e^i_L \tilde{\nu}^j_L \bar{e}^k_R + (\bar{e}^i_L)^c \nu^j_L \tilde{\nu}^{k*}_R)] + h.c. \tag{2.20}$$

$$\mathcal{L}_{LQ\bar{D}} = \lambda'_{ijk}[\tilde{\nu}^i_L d^j_L \bar{d}^k_R + \nu^i_L \tilde{d}^j_L \bar{d}^k_R + (\bar{\nu}^i_L)^c d^j_L \tilde{d}^{k*}_R - (\tilde{e}^i_L u^j_L \bar{d}^k_R + e^i_L \tilde{u}^j_L \bar{d}^k_R + (\bar{e}^i_L)^c u^j_L \tilde{d}^{k*}_R)] + h.c. \tag{2.21}$$

Here, the superscripts c denote the charge conjugate spinors and the $*$ the complex conjugate of scalar fields. Coefficients of λ_{ijk} are anti-symmetric under the inter-

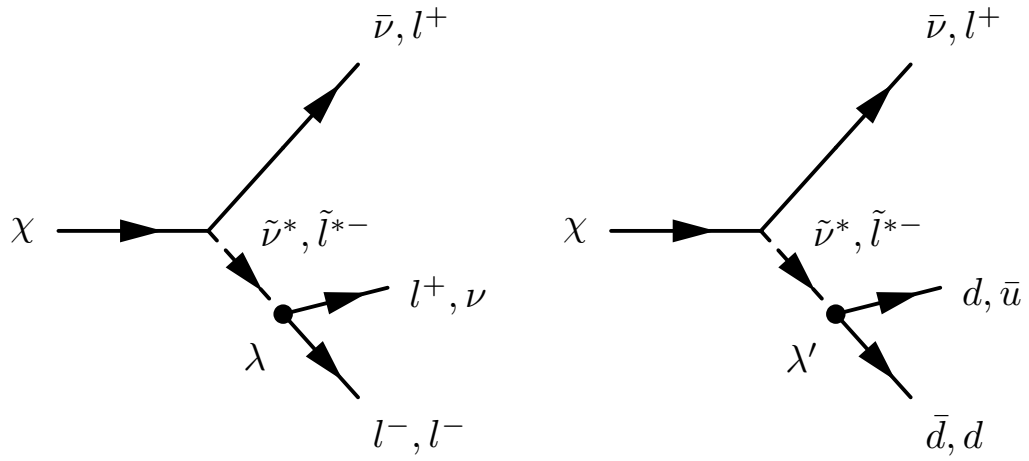

Figure 2.2: R-parity violating decays of supersymmetric particles via the λ and λ' coupling. The possible combinations of final state particles are shown.

change of the first two flavour indices $\{i \leftrightarrow j\}$ due to $\mathrm{SU(2)_L}$ invariance. This can be seen by comparing for example, the first and fourth term in Eq. (2.20). They are identical and would cancel each other out if the first two flavour indices are equal, i.e. if both particles are from the same generation. This is not the case for couplings via λ'_{ijk} as can be seen in Eq. (2.21), where no term is cancelled out by its counterpart. Similarly coefficients of λ''_{ijk} are anti-symmetric under the interchange of the last two flavour indices $\{j \leftrightarrow k\}$ due to $\mathrm{SU(2)_L}$ invariance. This results in

9+27+9=45 new terms beyond those of the MSSM as illustrated in Table 2.4. Fig. 2.2 shows the combinations of final state particles allowed under $LL\bar{E}$ and $LQ\bar{D}$ decays.

$LL\bar{E}$			$LQ\bar{D}$									$\bar{U}\bar{D}\bar{D}$		
121	122	123	111	112	113	121	122	123	131	132	133	112	113	123
131	132	133	211	212	213	221	222	223	231	232	233	212	213	223
231	232	233	311	312	313	321	322	323	331	332	333	312	313	323

Table 2.4: The allowed couplings for $LL\bar{E}$, $LQ\bar{D}$ and $\bar{U}\bar{D}\bar{D}$.

It was observed that the combination of lepton and baryon number violating operators in the Lagrangian would lead to rapid proton decay [26]. As illustrated in Fig. 2.3 the proton could decay via a combination of λ''_{ijk} and λ'_{ijk} couplings into a lepton and a hadron. Such diagrams would lead to a rapid decay of the proton which is in direct disagreement with experimental observation. The resulting bounds were so strict that only one coupling is assumed to be non-zero. In order to protect the proton as well as prevent the exclusion of the MSSM, R-parity was imposed by hand.

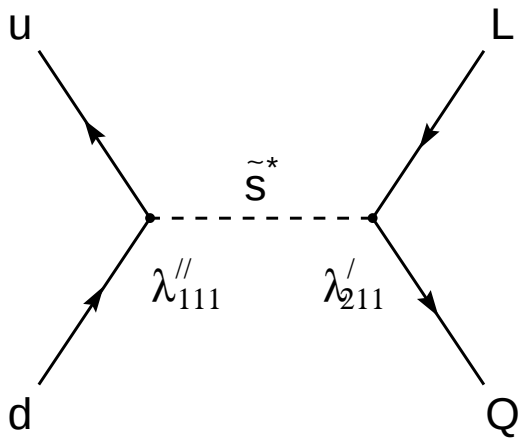

Figure 2.3: Feynman diagram showing an R-parity violating proton decay into a lepton and a hadron.

2.3.1 R-Parity conservation (RPC)

The conservation of R-parity has a number of implications in the search for supersymmetric particles [27]:

- Supersymmetric particles are produced in pairs, hence the kinematic limit for direct searches in a collider is the beam energy.
- The Lightest Supersymmetric Particle(LSP) is stable. It is weakly interacting and hence is a candidate for dark matter.
- The LSP is colourless and electrically neutral and hence will be either a sneutrino or the lightest neutralino.
- In a collider experiment the LSP will be undetected, thus events containing supersymmetric particles will be characterized by missing energy.

2.3.2 R-parity violation (RPV)

The imposition of R-parity by hand in the Lagrangian results in the exclusion of all terms in Eq. (2.19). Alternative symmetries which can still protect the decay of the proton and prevent the exclusion of all terms in $W_{\not R_p}$ are B-parity or L-parity, which forbid B-violating or L-violating interactions [25]. The phenomenological consequences of R-parity violation are:

- The supersymmetric particles need no longer be produced in pairs. This means that direct searches at a given collider can have a potentially higher mass reach.
- The LSP is no longer stable.
- The decay rate of the LSP will depend on the magnitude of the RPV couplings. This in turn affects whether the sparticle decays inside or outside the

detector (section 4.1). This results in a varied array of signatures consisting either of purely leptonic decays or multi-hadronic events with energetic leptons or just simply multi-jet decays. Section 6.1 gives a detailed review of the various signatures expected in all scenarios.

Chapter 3

Experimental overview

The ALEPH (Apparatus for LEP Physics) detector was one of four large experiments used to study e^+e^- collisions at the Large Electron Positron collider (LEP) in Geneva, Switzerland. Data collected from the ALEPH detector were used in this thesis. In this chapter, a brief history of LEP is given. The ALEPH detector is described and the functions and performance of its component parts are reviewed with emphasis placed on the elements relevant to supersymmetry searches. The method of data collection at ALEPH and the motivation for Monte Carlo simulation of Standard Model processes needed for this analysis are summarized.

3.1 LEP

LEP was completed at the European Centre for Particle Physics (CERN) in Geneva, Switzerland in 1988 and was designed to study the weak force. The LEP collider was situated in a circular tunnel of diameter 8.5km at a depth of between 50m and 150m, with an incline of about 1.4%. A view of the LEP ring situated underground is shown in Fig. 3.1. Electrons and positrons were stored in bunches and accelerated by the use of a radio frequency acceleration system. LEP produced its first collisions in 1989 and its last in 2000. There were two main phases of LEP. In the first

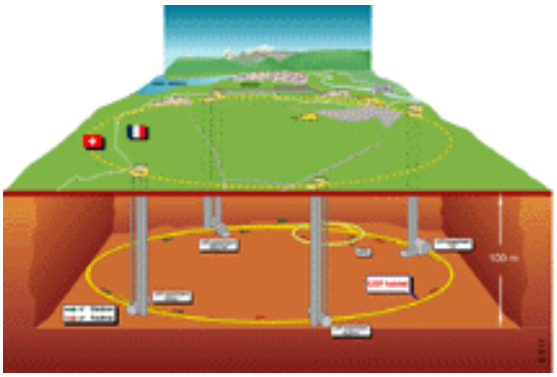

Figure 3.1: Underground view of the LEP ring.

phase, commonly referred to as LEP I, stringent tests were carried out on the Standard Model by performing detailed studies of e^+e^- collisions at energies very close to the Z boson resonance $\approx 91\,\text{GeV}$ [28]. In 1995, LEP was upgraded to enable the study of the W^+ and W^- bosons. An initial centre-of-mass energy of $\sqrt{s} \approx 130\,\text{GeV}$ was achieved and this was subsequently increased to the W-pair threshold of $\approx 161\,\text{GeV}$. This phase is commonly referred to as LEP II. By 2000, the last year of operation of the LEP collider, collisions at centre-of-mass energies of 208 GeV had been achieved, the Standard Model was firmly established as a corner-stone of modern particle physics and advances were made in the search for new physics phenomena. This has paved the way for the next generation of experiments.

3.2 ALEPH

ALEPH was situated in the beam of the LEP ring at one of the four points shown in Fig. 3.1. A cut-away diagram of the ALEPH detector is shown in Fig. 3.2. The ALEPH detector was designed to cover as much 4π solid angle as possible. It consisted of a collection of subdetectors put together to form a cylindrical structure with a barrel and two end-caps. It had a tracking system which consisted of a silicon

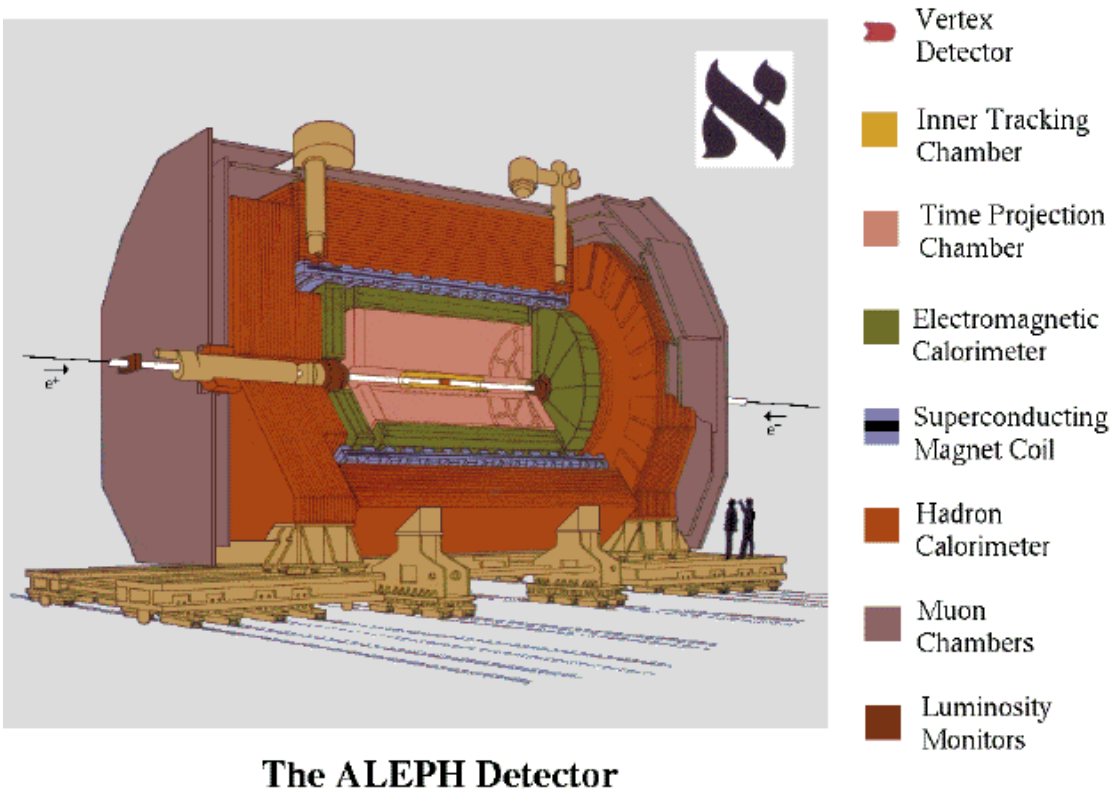

Figure 3.2: A schematic view of the ALEPH detector.

vertex detector, a cylindrical drift chamber and a large time projection chamber, all immersed in a 1.5T magnetic field provided by a superconducting solenoidal coil. Between the tracking system and the coil, a highly granular electromagnetic calorimeter was used to measure the energy deposited by electrons and photons. It was complemented at low angles by luminosity calorimeters. The iron return yoke for the magnetic field, besides serving as a structural support for the detector, was instrumented to act as a hadron calorimeter which was used to measure the amount of energy deposited by hadrons. The hadronic calorimeter was also used in conjunction with additional detectors to identify muons. This modular structure enabled ALEPH to perform to a high degree of efficiency the tasks for which it was designed [29]. A detailed description of the ALEPH detector and its component parts can be found in [30, 31].

The ALEPH detector was designed to

- measure the momenta of charged particles in a magnetic field of 1.5T;
- detect all three lepton flavours;
- measure the energy of neutral particles such as γ and π^0;
- measure the decay length of short-lived particles such as the τ lepton and the b and c hadrons;
- identify particles by virtue of their specific energy loss, dE/dx, due to ionisation;
- measure the luminosity (the rate of particle collisions per unit cross section) by the use of various low angle calorimeters;

The first three features above were of particular importance to this analysis.

A three-dimensional coordinate system was used by ALEPH to describe information obtained from particle interactions. The coordinate system was expressed in terms of (x, y, z) or (r, ϕ, z). In both cases the z direction represented the beam line, and was taken as positive in the direction followed by the electron. The positive x was taken as pointing in a direction towards the centre of LEP, and is horizontal by definition. The positive y direction was taken as being orthogonal to z and x. However y was not strictly vertical due to the inclination of LEP, resulting in the beam axis making a 3.6mrad angle with the horizontal. r and ϕ are standard cylindrical coordinates, r increases with radial distance from the beam line and ϕ circles around the detector in a right-handed sense to the z axis.

3.3 The tracking system

Charged particle tracking in ALEPH was carried out in the vertex detector, the inner track chamber and the time projection chamber.

3.3.1 The Minivertex Detector (VDET)

The purpose of the VDET was to pinpoint a track's location as near to the interaction point as possible. The VDET consisted of two layers of silicon wafers arrayed around the beam pipe, at radii of 6.3cm and 10.8cm. Coverage in z extended to about $\pm$20cm. Ionisation energy from particles passing through the VDET was deposited on each side of a wafer. Each side of the wafer had readout strips. Energy deposited was read out on one side in the z direction and in the $r-\phi$ direction on the other side. Improvements were carried out on the VDET [31] in 1995 by increasing its coverage in z to $\pm$40cm and by reducing the distance between readout strips by a factor of two. The reason for these changes was to increase the discovery potential for the Higgs searches by extending the angular coverage of the detector and reducing the material in the tracking volume. The improved VDET had a point resolution of $\approx 12\mu$m in the $r-\phi$ direction and $\approx 14\mu$m in the z direction for $\cos\theta < 0.4$. It had an angular acceptance range of $-0.95 < \cos\theta < 0.95$ for tracks required to hit at least one layer. This aided track reconstruction and enabled the resolution of tracks produced from the decay of short-lived particles at the Interaction Point (IP).

3.3.2 The Inner Tracking Chamber (ITC)

The ITC [33] was a cylindrical multi-wire drift chamber, approximately two metres in length and extending about 30cm from the beam pipe. It had eight layers of sensing wires which were spaced at about 1cm to 1.5cm apart. The function of these

wires was to detect the ionisation produced by charged particles passing close by. By measuring the drift time, the $r-\phi$ coordinate was measured to an accuracy of 150μm. z information was obtained by the division of charge between the two ends of the wire with an accuracy of 7cm. The function of the ITC was to provide precise $r-\phi$ coordinates along a track for reconstruction of position and direction. It also provided information on tracks for the Level-1 trigger. In the ITC, the triggering decision time was 500ns in the $r-\phi$ plane and 2μs in three dimensions.

3.3.3 The Time Projection Chamber (TPC)

Most of the information about charged particle tracks was provided by the TPC. It was a cylindrical structure about 4.7m long with its axis parallel to the magnetic field axis, and extended to a radius of 1.8m from the beam. It had a central membrane at a potential of 27kV which divided the chamber into two halves with end-plates at either end. The electric drift field extended from each end-plate towards the central membrane. The passage of a charged particle through the TPC left ionisation trails which drifted in the electric field with a drift velocity of 5.2cm/μs to either end-plate at the end of the chamber. A gas composition of argon and methane in a proportion of 91% : 9% was used to provide the medium for ionisation. The ionisation was recorded in up to three ways. Wires in the end-plates recorded the pulse height of the ionisation. An extra grid of wires called the TPC gating grid, served as a gate to prevent space charge passing from the wire chambers into the TPC. If allowed to pass into the TPC drift region, the space charge could alter the electric field causing unwanted track distortions. Finely spaced pads beneath the wires localized the ionisation in the $r-\phi$ direction with a spatial resolution of 173μm. The longitudinal resolution was 740μm for tracks with polar angles within 10° perpendicular to the beams [29]. Finally, larger trigger pads were spaced around the end-plates for triggering by the Level-2 trigger.

Three-dimensional images of charged tracks were provided from track information produced at the pads. Due to the presence of a magnetic field, the curvature of the track, apart from identifying the charge of the track, enabled the momentum to be measured with a resolution of

- $\Delta p/p^2 = 1.2 \times 10^{-3}(\,\mathrm{GeV}/c)^{-1}$ using information from the TPC only.
- $\Delta p/p^2 = 0.8 \times 10^{-3}(\,\mathrm{GeV}/c)^{-1}$ using information from the ITC+TPC.
- $\Delta p/p^2 = 0.6 \times 10^{-3}(\,\mathrm{GeV}/c)^{-1}$ using information from the VDET+ITC+TPC.

In the TPC, the rate of energy loss by ionisation dE/dx was used to separate charged electrons from kaons, pions and protons with a resolution of 4.5% for Bhabha electrons. Fig. 3.3a shows a plot of dE/dx as a function of momentum for various charged particles using a sample of 40,000 tracks. Each track was re-

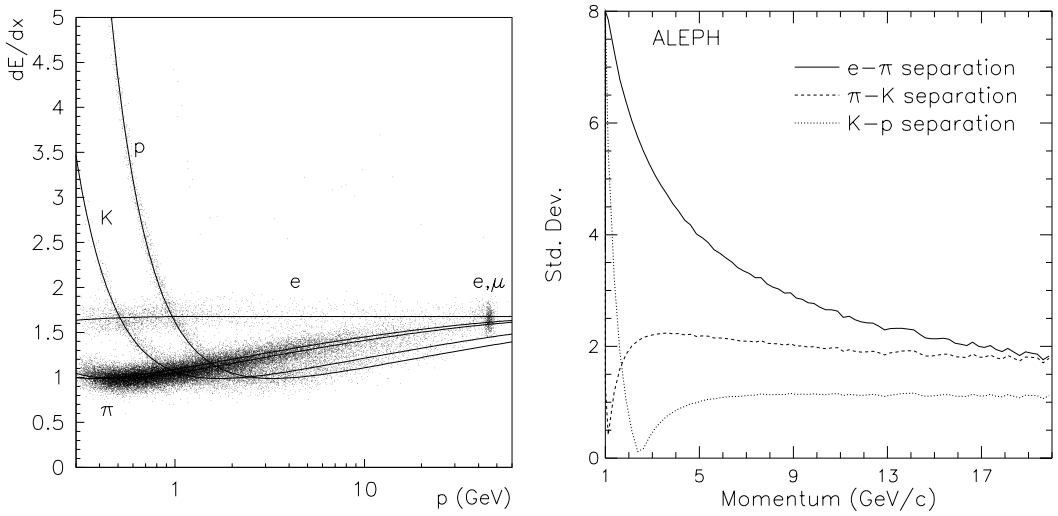

Figure 3.3: The separation of particles using; (a) the measured dE/dx versus particle momentum for a sample of about 40,000 tracks. Each track was required to have at least 150 dE/dx measurements. The fitted parameterization was superimposed for electrons, muons, pions, kaons and protons. (b) the average dE/dx separation in standard deviations between particle types, computed using all tracks in hadronic Z decays which have at least 50 dE/dx measurements [29].

quired to have at least 150 dE/dx measurements. The dE/dx method of separating

charged particles was only effective at low momentum.

3.4 The triggering system

The ALEPH triggering system aimed to identify all e^+e^- events of physics interest, while at the same time rejecting backgrounds such as beam gas, cosmic rays and scattered beam particles. It was divided into three levels: Level-1, Level-2 and Level-3. Level-1 was concerned with using information starting at the ITC to decide whether there was a good charged track and/or particle energy (from the calorimeters) to justify waiting for the Time Projection Chamber trigger signals. Level-1 had a fast response time 5μs, which enabled it to identify roughly the number and location of tracks and then reject non-interesting events before another beam crossing occurred (11.1μs). There were different types of level-1 triggers. One type involved requiring coincidence between tracks in the ITC and energy deposited in the electromagnetic calorimeter. Another type was based on the energy deposited into the electromagnetic calorimeter barrel and/or end-caps. A third type was based on the requirement of coincidence between tracks in the ITC and energy deposited in the hadronic calorimeter. A fourth was based on energy deposited in the luminosity calorimeter modules. A Level-1 Yes trigger initiated digitization keeping the TPC gate open for the full drift time of 45μs. Level-2 triggering was initiated after a Level-1 Yes decision and made using track information from the TPC and not the ITC. The Level-2 trigger had a decision time of 50μs after the beam crossing. A Level-2 Yes decision initiated a full digital readout of the detector. A Level-2 No decision resulted in the clearing of the ECAL and the resetting of the data acquisition system (DAQ). The Level-3 trigger was performed by software. It checked the trigger decision made at Level-2, using all the data from the whole detector after readout and rejected any event that clearly

should not have been accepted. It ensured a reduction of the trigger rate to 1-2Hz for data storage.

3.5 The calorimeters

A calorimeter is a device which measures the amount of deposited energy. In ALEPH, the calorimetry system measured the energy deposited when particles from e^+e^- collisions produced either electromagnetic or hadronic showers.

3.5.1 The Electromagnetic Calorimeter (ECAL)

In the ECAL, the showers were produced by bremsstrahlung and pair production allowing electrons and photons to be identified by their characteristic showering behaviour. The ECAL was divided into a barrel region and separate sections for each of the two end-caps of the detector. It consisted of alternating wire chambers and lead sheets. Charged particles were detected via their ionisation as they passed through the wire chambers. A gas combination of xenon and carbon-dioxide in a proportion of 80% : 20% provided the medium for ionisation to occur. The lead sheets caused electrons, positrons and photons to produce showers of many particles which created a much larger signal than a single minimum-ionizing particle. The wire planes at increasing distance from the beam measured the longitudinal penetration of a shower. Cathode pads were connected in *towers* covering $1^\circ \times 1^\circ$ regions of solid-angle as seen from the interaction point, in three *storeys* of depth. The fine granularity in solid angle provided good separation of particles in jets. In Fig.3.4 the resolution of the ECAL as a function of its dependence on energy and polar angle is illustrated. The ECAL had an energy resolution of $\sigma/E = 0.01 + 0.18/\sqrt{E\,(\mathrm{GeV})}$ and an angular resolution of $\sigma_\phi = \sigma_\theta/\sin\theta = 0.32 + 2.7/\sqrt{E\,(\mathrm{GeV})}$mrad .

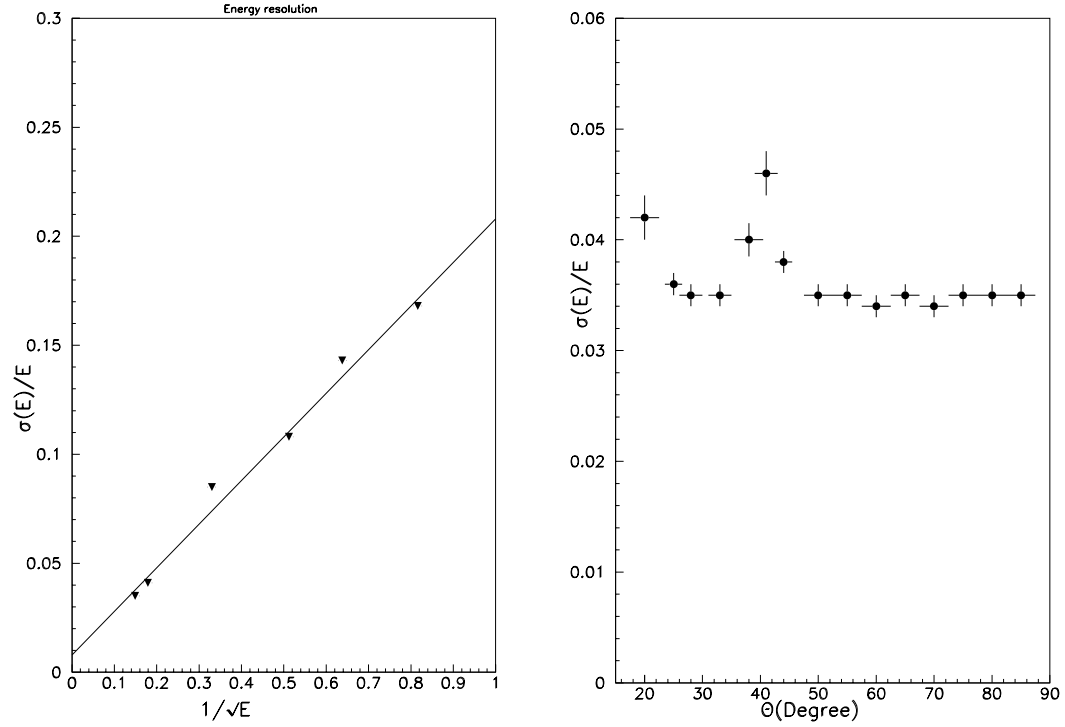

Figure 3.4: Energy resolution of the electromagnetic calorimeter showing, (a) dependence on energy, (b) dependence on polar angle for electrons from $Z \rightarrow e^+e^-$ decays. The peak seen in (b) at $\approx 20^\circ$ was due to effects from particles lost in the region between the ECAL and the luminosity monitors. The peak at $\approx 45^\circ$ occurs in the region where the barrel and the end-cap overlap.

3.5.2 The Hadronic Calorimeter (HCAL)

The HCAL consisted of alternate layers of iron and streamer tubes. Apart from being used as a hadron calorimeter, it served as a return yoke for the magnetic flux return and a muon filter. Like the ECAL, the barrel and end-cap regions were separate from each other. The streamer tubes detected ionisation caused by particles passing through them. Ionisation occurred in a gas based environment containing a mixture of argon, carbon-dioxide and isobutane in the proportion 22.5% : 47.5% : 30%. Hadrons passing through the iron layers resulted in hadronic interactions and generated showers of additional particles. In contrast muons did not interact with the HCAL but passed straight through. The HCAL was used to

identify hadrons - charged and neutral, by distinguishing hadronic showers from the cleaner penetrations of muons. Three types of signal were extracted from the HCAL. The signals from the streamer tube wires were used in the trigger as a measure of the energy deposition as a function of depth. Signals from pads which ran perpendicular to the tubes and were connected into $3.7^\circ \times 3.7^\circ$ towers in solid angle pointing towards the IP. Finally, signals from strips which ran along the tubes and were used to form a digital image of the path of a particle through the HCAL. The hadronic energy was measured with a resolution of $\sigma/E = 84\%/\sqrt{E}$.

3.5.3 The Muon Chambers

The muon chambers consisted of two double layers of streamer tubes situated on the outside of the HCAL and were used in conjunction with the HCAL to identify muons. The detector elements were similar to those of the HCAL. In addition to the information received from the individual strips in the HCAL, the streamer tubes were used to identify tracks crossing the full iron and to measure their angles. They had the same gas composition as the HCAL. They measured one or more three-dimensional points on tracks leaving the HCAL. Additional streamer tubes called middle-angle chambers were used to cover the gaps left open in the boundary region between the HCAL and the muon chambers. This resulted in all angles down to the beam pipe and superconducting quadrupole being monitored. Monte Carlo estimates for the typical muon misidentification probability at 5 GeV for 95% efficiency were 0.7% to mistake a π for a μ and 1.6% to mistake a K for a μ.

3.6 The luminosity monitors

The luminosity monitors were used to provide a measurement of the beam luminosity and also to provide coverage at angles very close to the beam pipe. In

ALEPH, the luminosity was measured using the QED Bhabha scattering process ($e^+e^- \rightarrow \gamma^* \rightarrow e^+e^-$). The luminosity was obtained by dividing the number of events detected in a suitable detector by the Bhabha cross section integrated over the detectors acceptance. However, due to the fact that the electroweak process $e^+e^- \rightarrow Z \rightarrow e^+e^-$ interferes with the QED process and introduces poorly known corrections to the cross section, the acceptance was restricted to low angles only. At low angles Bhabha rates are dominated by small values of four-momentum transfer and are well described by QED alone.

3.6.1 The Luminosity Calorimeter (LCAL)

The LCAL was a lead/wire calorimeter and operated in a similar manner as the ECAL. It consisted of two semi-circular modules placed around the beam-pipe at each end of the detector, between the beam-pipe and the ECAL end-caps. It monitored angles from 45mrad to 190mrad from the beam axis. As in the ECAL, both pad and wire signals were available. The wire signals were used for triggering and determination of shower depth. The pads were used to determine the position of the incident particle. The pads formed projective towers, each of three storeys, in solid-angle viewed from the IP. Electrons and positrons from Bhabha scattering were found by requiring hits directly opposite each other in the LCAL modules on either side of the ALEPH detector.

3.6.2 The Silicon Luminosity Calorimeter (SICAL)

In 1995 the SICAL was added to the ALEPH detector to provide more precise measurements than the LCAL. This was done by sampling smaller angles to the beam so as to reduce the systematic error by eliminating contributions from dead zones. It covered an angular region of 24mrad to 58mrad away from the beam direction and was mounted around the beam-pipe in front of the LCAL.

3.6.3 The Very Small Angle Bhabha Calorimeter (BCAL)

The BCAL was designed to provide an on-line measurement of the beam luminosity. It consisted of two calorimeters placed behind (as seen from the interaction point) the superconducting quadrupole magnets, above and below the beam-pipe at either end of the ALEPH detector. Each calorimeter consisted of ten tungsten sheets alternated with sampling layers of plastic scintillators read out in pairs. A single plane of silicon strips was also embedded at a depth of eight radiation lengths. The BCAL was situated at a distance of 7.7m from the IP and covered an angle of $\theta_{min} \approx$ 5mrad to $\theta_{max} \approx$ 9mrad. It had only a partial coverage in azimuth ϕ. Despite its partial coverage in azimuth, the BCAL recorded rates at twenty times that recorded by the LCAL due to the rise in Bhabha cross section at small angles.

3.7 Identification of particles

In ALEPH, electrons were identified using the two independent but complementary processes of dE/dx measurements and the measurement of energy deposited in the ECAL compared to track momentum and the expected shape of the shower [29]. The dE/dx is only effective for low momentum tracks while the shape of showers in the ECAL is effective at high momentum. In this analysis only the latter was used. Muons were identified by making use of the tracking capabilities of the HCAL together with information from the muon chambers. Taus were more difficult to identify due to the presence of neutrinos which made it impossible to to reconstruct its invariant mass. In leptonic events, they were identified by their track multiplicity, acollinearity and missing mass.

3.7.1 Electron identification using estimators

Measurements from the ECAL are combined into estimators that, for an electron should be normally distributed around zero. Two such estimators are constructed. The first, R_T, measures the transverse extent of the shower and the other, R_L measures the longitudinal extent.

Transverse shower shape: R_T

An electron loses most of its energy in the ECAL as opposed to a hadron. A consequence of this is that the resultant showers are more compact in the transverse direction than showers formed from the passage of a hadron. The estimator R_T exploits this characteristic by comparing the energy recorded close to an extrapolation of the charged track with the expected energy deposition for an electron of a given momentum. To determine R_T, charged tracks are extrapolated from the ITC and their crossing point is computed in each of the three segments in depth of the calorimeter. R_T is defined using the four storeys closest to the extrapolated track in each segment and is given by:

$$R_T = \frac{E_4/p - \langle E_4/p \rangle}{\sigma_{E_4/p}}, \tag{3.1}$$

where E_4 is the total energy deposited in the selected storeys, p is the momentum of the charged track measured in the TPC, $\langle E_4/p \rangle$ is the mean energy fraction deposited by an electron in the four central towers, and $\sigma_{E_4/p}$ is the resolution expected for this ratio.

Longitudinal shower shape: R_L

An electromagnetic shower has a characteristic longitudinal shape. R_L is based on the inverse of the mean depth of the longitudinal energy deposition in the shower

which is described by:

$$X_L = \frac{E_4}{\sum_{ij} E_i^j S_j}, \tag{3.2}$$

where E_i^j is the energy deposited in a selected storey $i = 1, 4$ of segment $j = 1, 3$ in depth of the calorimeter, and S_j is the mean depth of energy deposition in that segment. X_L is independent of the angle of the incoming particle [34] and is computed using an iterative procedure which attempts to fit the longitudinal deposition to the standard shape [35] expected for an electromagnetic shower. The normally distributed estimator R_L is thus defined by

$$R_L = \frac{X_L - \langle X_L \rangle}{\sigma_{X_L}}. \tag{3.3}$$

Conversions

Electrons may be produced from the conversion of photons in the material of the detector. It is important to avoid selecting electrons which result from conversions as they would reduce the ability to distinguish between supersymmetry signal events, where the leptons are produced by the decays of supersymmetric particles and Standard Model background processes. Conversions are identified by trying to find pairs of tracks that could come from a single displaced vertex. The most likely displaced vertex point is the point where the tracks are parallel in the xy plane and pass closest to each other. Conversions are identified if the distance between the two tracks in the xy plane at the point in which they pass closest together is less than 2cm. Also, the distance between the two tracks in the z direction at this point must be less than 3cm. Finally, the invariant mass of the two tracks at this point assuming they are both electrons must be less than 40 MeV.

In this analyses, for a track to be considered as an electron

- it must be a *good* track and not identified as a conversion. A good track is

a charged particle track with at least four hits in the TPC originating from within a cylinder of radius 2cm and length 20cm, coaxial with the beam and centred on the interaction point.

- $p \geq 2\,\mathrm{GeV}/c$.
- $R_T \geq -3$.
- $-2.4 \leq R_L \leq 3$.

Electrons were identified by the ECAL with a mean efficiency of $(78.5 \pm 0.06)\%$ with the probability of misidentification, i.e, identifying a hadron for an electron, given by $(3.44 \pm 0.05)^{-3}$ [29].

3.7.2 Muon identification

Muons were identified by making use of the tracking capabilities of the HCAL together with the muon chamber information. Muons interact in the HCAL by ionisation and therefore the hits caused by muons are concentrated around the extrapolated path and not scattered over a large area. Also, the fact that muons were expected to travel further through the HCAL than hadrons meant that planes further away from the interaction point were more likely to fire if a track was a muon than if it was a hadron. A hit in the muon chamber was an indication that the track had escaped the detector altogether and this greatly aided the identification process.

Tracks were extrapolated through the HCAL material taking into account a detailed magnetic field map and estimated energy losses. A road was then defined around the extrapolated track with a width of three times the estimated extrapolation uncertainty to take into account multiple scattering. HCAL planes were expected to fire if the extrapolated track intersected it within an active region and the plane was said to have fired if a digital hit lay within the multiple scattering

road. For a hit to be counted, the number of firing tubes must not be greater than three. A track was defined to have a hit in the muon chambers if at least one of the two double-layers yielded a space point whose distance from the extrapolated track was less than four times the estimated deviation from multiple scattering. Tracks were considered for muon identification if they had a momentum greater than 3 GeV/c. The variable quantities N_{exp} and N_{fire}, where N_{exp} was defined as the number of expected planes and N_{fire} the number of actual firing planes, were used to define the penetration of a track. Since a muon was more likely to penetrate more HCAL planes than hadrons, the ratio N_{fire}/N_{exp} was expected to be larger for muons. The number of firing planes within the last ten expected for the track, N_{10}, was also used to assess the penetration of the track. Finally the typical features of the digital pattern created by a hadron shower in the hadron calorimeter were used to enhance the rejection power against the hadron background. This was done by identifying the number of digital hits in the last eleven planes of the HCAL within a wide road, increasing from 20cm to 30cm, around the extrapolated track and dividing this by the number of firing planes to give the average hit multiplicity per fired plane. This quantity was defined by the variable X_{mult}.

A good penetrating track must satisfy the following criteria:

$$\begin{aligned} N_{fire}/N_{exp} &\geq 0.4. \\ N_{exp} &\geq 10. \\ N_{10} &> 4. \\ X_{mult} &\leq 1.5. \end{aligned} \tag{3.4}$$

Fig. 3.5 shows the distributions of N_{fire}/N_{exp}, N_{10} and X_{mult} for muons coming from $Z \to \mu^+\mu^-$ events compared to those of pions produced in τ decays. In the analyses presented here, candidates were accepted as muons if they satisfied at

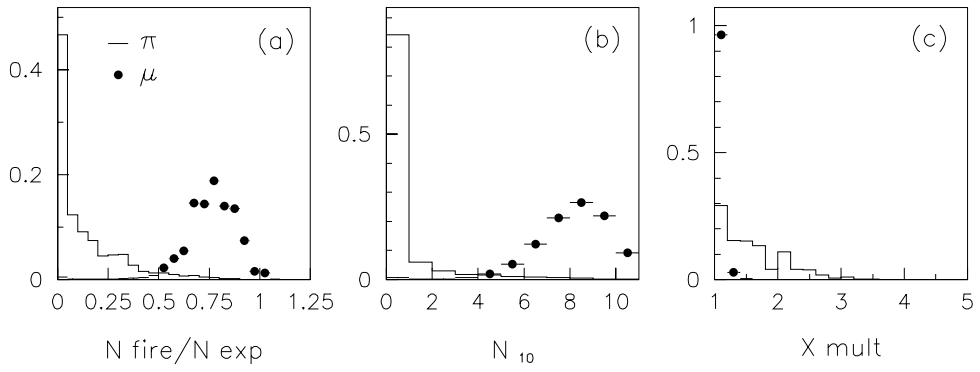

Figure 3.5: Distribution of (a) N_{fire}/N_{exp}, (b) N_{10} and (c)X_{mult} for muons (points) and pions (solid line), with N_{exp} greater than 10. The plots have been normalized to equal areas and the vertical scale is arbitrary [29].

least one of three selections:

- A selection based on the HCAL information alone.
- A selection based on a combination of HCAL and muon chamber information. In this case a good penetrating track must be associated with at least one muon chamber hit.
- A selection based only on muon chambers, in which case a track must be associated with at least one muon chamber hit in each layer.

Muons were identified with a mean efficiency of 86%. The probability of misidentifying a hadron as a muon was 0.008 [29].

3.8 Data taking from ALEPH

The search described in this thesis for supersymmetric particles which decay via an R-parity violating coupling, was performed using data with a total integrated luminosity of 628 pb^{-1} over an energy range of 189 GeV to 208 GeV and recorded

between 1998 and 2000. Table 3.1 gives a summary of the integrated luminosities recorded by ALEPH at various centre-of-mass energies. The figures quoted under the first column represent the nominal energy obtained from the averaged luminosity weighted centre-of-mass energy spread as illustrated in Fig. 3.6. A

Energy (GeV)	Year	Integrated Luminosity (pb^{-1})
188.6	1998	174.2
191.6	1999	28.9
195.5	1999	79.9
199.5	1999	86.3
201.6	1999	41.9
199.8	2000	0.8
201.8	2000	0.7
202.7	2000	1.8
203.8	2000	7.2
205.0	2000	72.3
206.3	2000	19.1
206.6	2000	107.5
208.0	2000	7.8

Table 3.1: Integrated luminosities recorded by ALEPH at each centre-of-mass energy achieved by LEP between 1998 and 2000. The figures in the first column were obtained by averaging out the weighted centre-of-mass energy distributions as shown in Fig. 3.6.

reconstruction program JULIA [37] used as input, the raw data produced by the ALEPH detector or from Monte Carlo simulation runs to reconstruct events. JULIA performed the majority of track fitting and calorimeter reconstruction needed for physics analysis. The output from JULIA was called a Production Output Tape (POT). It is a file type with a BOS bank structure [38], where BOS (Bank Object Structure) was a set of memory management and input/output routines used to allow handling of data-structures having arbitrary size and format. The reconstructed events were then stored on to Data Summary Tapes (DSTs) if they satisfied one or more of the following conditions:

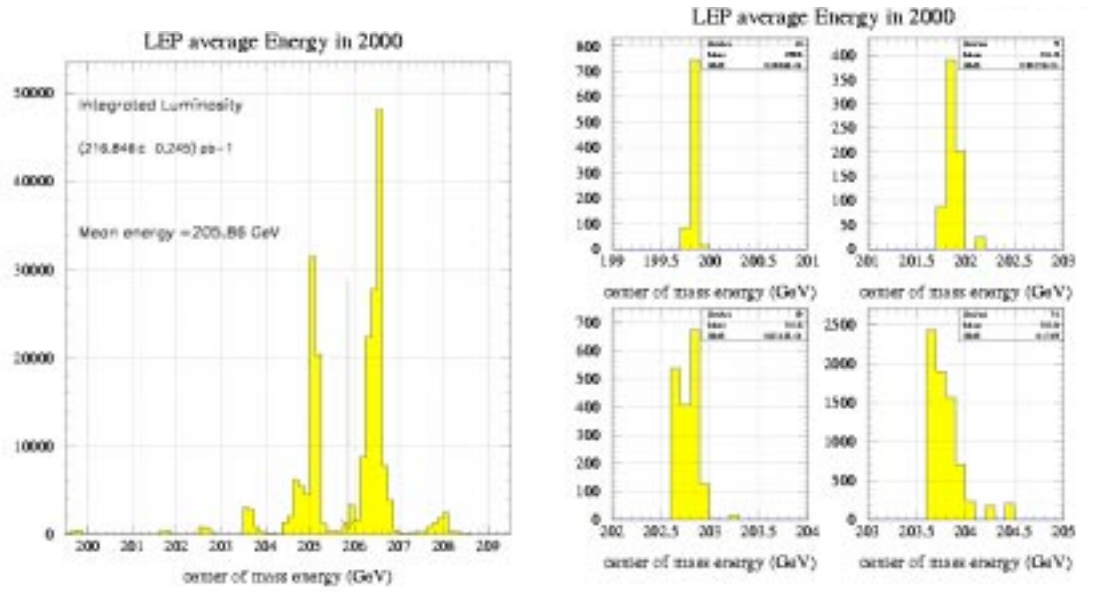

Figure 3.6: (a) The luminosity weighted centre-of-mass energy distribution for data collected by the ALEPH detector in 2000. (b) The same distribution shown for data collected at 200 GeV, 202 GeV, 203 GeV and 204 GeV. The spread at each nominal energy can clearly be seen. The plots were obtained from [36].

- An event must have at least 3 GeV of charged energy coming from within 5cm in d_0 and 20cm in z_0, where d_0 is the distance of closest approach to the z-axis and z_0 is the z coordinate at that point.
- An event must have two or more charged tracks with d_0 and z_0 within this range.
- An event must have at least one photon candidate and no charged tracks.
- An event must have a total ECAL wire energy greater than 15 GeV and ECAL $\mid t_0 \mid < 500$ns where t_0 is the difference between the time of the event as recorded by the ECAL wires and the time of the nearest LEP bunch crossing. Typically t_0 for e^+e^- collisions have absolute values less than 100ns.

Events on the DSTs were further compressed to produce a mini-DST and additional banks used in reconstruction were removed. Either the DST's or Mini-DST files formed the starting point in most physics analyses at ALEPH.

3.9 Event simulation

In order to develop procedures to distinguish between events from the process being searched for (*signal*) and events from known Standard Model processes (*background*), Monte Carlo programs were used. This allowed a set of selections to be developed to extract the signal from the background and subsequently applied to the real data. The results were compared to results that would be expected in the absence of signal as given by the background and the degree of evidence for the signal process was quantified.

Three types of programs were used to generate Monte Carlo events.

- Event Generators: These were programs which randomly generated a particular interaction by choosing the final state particles and the momenta of the final state particles according to the differential cross section for the chosen process. ALEPH maintains a library of event generators called KINGAL [39].

- Auxiliary programs: These were programs used to simulate the time evolution of final state particles. Some of the more popular programs are JETSET [40] (for the simulation of final state QCD showers, hadronisation processes and the decay of hadrons) and PHOTOS [41] (for the simulation of final state QED radiation). In some cases these programs were fully incorporated into an event generator and were intrinsic to it. In many other cases the event generators required interfacing to these auxiliary programs.

- Detector Simulation: These were programs to simulate the interactions of the final state particles with the detector. GALEPH [42] was the Monte Carlo program used to simulate the ALEPH detector. It was based on the GEANT [43] package which stored a whole library of routines containing information on the interaction of particles with different materials. GALEPH contained a detailed description of the geometry of ALEPH and the materials that

made up the different components. Making use of the GEANT package, the particles were transported through the geometric description of ALEPH taking into account the boundaries between the detector elements as well as the electric and magnetic fields. The output from GALEPH was stored in the same format as the raw data from the detector. This enabled the same reconstruction programs to be run on both simulation and data.

3.9.1 Monte Carlo signal

The event generator used to simulate the production of MSSM sparticles was called SUSYGEN [44]. All signal events in this analysis were generated using SUSYGEN, which was designed to handle a wide range of supersymmetry signals in e^+e^- collisions. The events generated by SUSYGEN were passed through GALEPH and JULIA.

The following assumptions were maintained for all events generated.

- Though decays via $LL\bar{E}$, $LQ\bar{D}$ and $\bar{U}\bar{D}\bar{D}$ couplings are addressed in this analysis, only one coupling for a specific set of indices (i, j and k) in Eq. 2.19 is considered non-zero at any one time.

- The lifetime of the LSP is negligible, i.e. the LSP has a decay length of less than 1cm (Section 4.1).

- There is no mixing between sfermions within the first and second generation.

- There is no mixing between direct decays and indirect decays.

- Events were produced with both Initial State Radiation (ISR) and Final State Radiation (FSR) switched on. ISR is the process where the incident $e^-(e^+)$ emits a low energy photon during collisions. In FSR, an outgoing final state particle emits a photon.

3.9.2 Background

A large array of Standard Model processes form significant backgrounds to the search for supersymmetric particles which decay via R-parity violating couplings. Table 3.2 lists all the major backgrounds together with their cross sections and the

Standard Model processes				
Name	Process	σ (pb) at 208 GeV	No of Events	Generator
di-lepton production	$e^+ e^- \to e^+ e^-$	794.2	480000	BHWIDE
	$e^+ e^- \to \mu^+ \mu^-$	6.64	50000	KORALZ
	$e^+ e^- \to \tau^+ \tau^-$	6.56	50000	KORALZ
	$e^+ e^- \to q \bar{q}$	78.52	125000	PYTHIA
two-photon production	$\gamma\gamma \to e^+ e^-$	194.0	600000	PHOT02
	$\gamma\gamma \to \mu^+ \mu^-$	187.0	600000	PHOT02
	$\gamma\gamma \to \tau^+ \tau^-$	88.8	300000	PHOT02
	$\gamma\gamma \to u\bar{u}/d\bar{d}$	487.1	500000	PHOT02
	$\gamma\gamma \to c\bar{c}$	94.74	100000	PHOT02
	$\gamma\gamma \to s\bar{s}$	23.4	25000	PHOT02
	$\gamma\gamma \to b\bar{b}$	0.6	5000	PHOT02
four-fermion WW, Weν	$e^+ e^- \to W^+ W^-$	17.61	100000	KORALW
	$e^+ e^- \to W^+ e^- \nu$	0.9	20000	PYTHIA
four-fermion ZZ, Zee	$e^+ e^- \to Z Z$	2.8	50000	PYTHIA
	$e^+ e^- \to Z ee$	98.65	400000	PYTHIA

Table 3.2: Standard Model processes at 208 GeV that are relevant to this analysis. At least 200 times the number expected in data was analysed for each process.

generators used for their production.

- Bhabha scattering was simulated with BHWIDE [45].
- Muon and tau pair production was simulated with KORALZ [46].
- Two-photon events were simulated using the PHOT02 [47] generator.
- Pairs of W bosons were generated with KORALW [48].

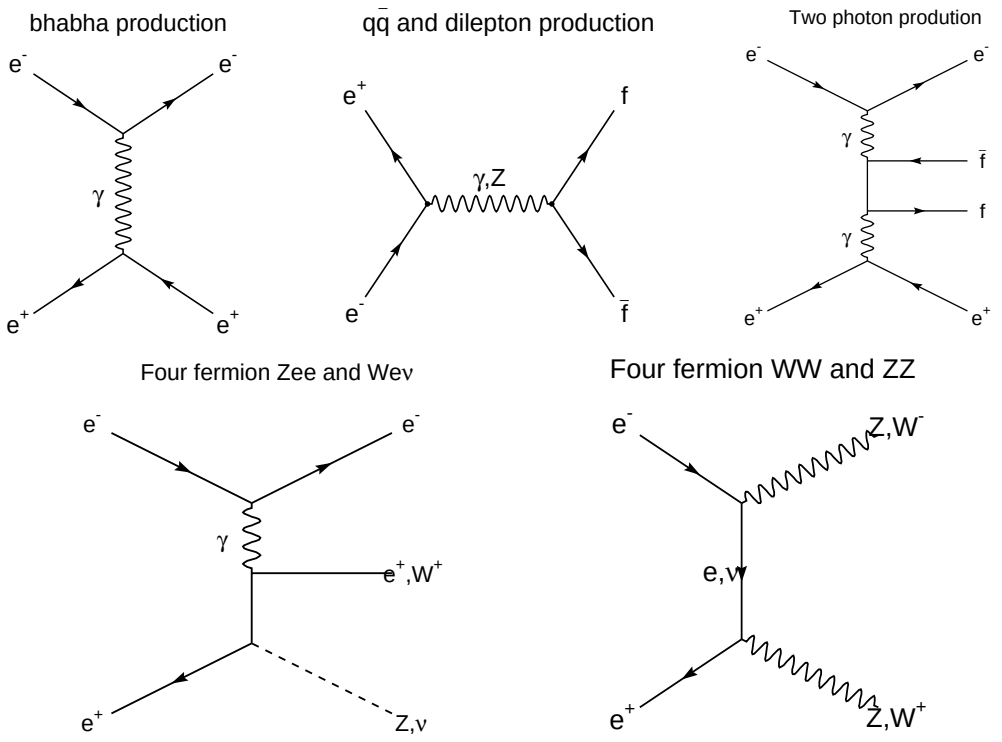

Figure 3.7: Some of the backgrounds that were considered for this analysis.

- The PYTHIA generator [49] was used to produce $q\bar{q}$ events and four-fermion final states from Weν, ZZ and Zee.

The generated events were processed by GALEPH and then JULIA. Before the events were stored in a format ready to be used for analysis, kinematic cuts were applied to some four-fermion processes and all the two-photon processes. This was done primarily to discard very low energy events that have been triggered but will not contribute in any way to the analysis. This also reduced the data size by a large factor. For the two-photon to quark processes, events were required to have a final invariant mass of at least $2.5\,\mathrm{GeV}/c^2$ and a scattering angle of more than 5mrad. Events from Two-photon to all lepton processes were required to have a transverse momentum of at least $0.15\,\mathrm{GeV}/c$ and an invariant mass of greater than $10\,\mathrm{GeV}/c^2$ for $\gamma\gamma \to e^+\,e^-$ and $\gamma\gamma \to \mu^+\,\mu^-$ and greater than $9.5\,\mathrm{GeV}/c^2$ for $\gamma\gamma \to \tau^+\,\tau^-$. Four-fermion Zee and ZZ events were required to have an invariant mass of at least

$0.2\,\mathrm{GeV}/c^2$.

All the background samples were produced by various working groups in the ALEPH collaboration. The Feynman diagrams for some of these processes are illustrated in Fig. 3.7.

Chapter 4

Limits from collider searches

In this chapter, a brief review of the existing limits which are relevant to the phenomenology of R-parity violation is presented. The limits on couplings and the importance of these couplings with respect to searches carried out in this analysis are discussed. Limits from sfermion masses are mentioned and limits from the Z width are described.

4.1 Limits on RPV couplings

R-parity violating interactions can contribute to various low energy processes via the virtual exchange of supersymmetric particles [50]. The absence of observation of the effects of these modifications to Standard Model predictions has led to bounds on the $\not{R}_p$ operators. For example, the non-observation of proton decay places strong bounds on the simultaneous presence of lepton and baryon violating couplings. For couplings involving light generations, the product of $LQ\bar{D}$ and $\bar{U}\bar{D}\bar{D}$ couplings is bounded by $|\lambda'\lambda''| < 10^{-24}$ [51]. The upper limit for any product combination of λ' and λ'' in the absence of squark flavour mixing is 10^{-9} [52]. Similarly, upper limits on product combinations of $LL\bar{E}$ and $LQ\bar{D}$ couplings are set at $\approx 10^{-8}$ [53].

ijk	λ_{ijk}	λ'_{ijk}	λ''_{ijk}
111	-	$5.2 \times 10^{-4} \times X$	-
112	-	$0.021 \times \frac{m_{\tilde{s}_R}}{100\,\mathrm{GeV}/c^2}$	$10^{-15} \times \left(\frac{M_{\tilde{q}}}{\mathrm{TeV}}\right)^{5/2}$
113	-	$0.021 \times \frac{m_{\tilde{b}_R}}{100\,\mathrm{GeV}/c^2}$	10^{-4}
121	$0.049 \times \frac{m_{\tilde{e}_R}}{100\,\mathrm{GeV}/c^2}$	$0.043 \times \frac{m_{\tilde{d}_R}}{100\,\mathrm{GeV}/c^2}$	-
122	$0.049 \times \frac{m_{\tilde{\mu}_R}}{100\,\mathrm{GeV}/c^2}$	$0.043 \times \frac{m_{\tilde{s}_R}}{100\,\mathrm{GeV}/c^2}$	-
123	$0.049 \times \frac{m_{\tilde{\tau}_R}}{100\,\mathrm{GeV}/c^2}$	$0.043 \times \frac{m_{\tilde{b}_R}}{100\,\mathrm{GeV}/c^2}$	(1.23)
131	$0.062 \times \frac{m_{\tilde{e}_R}}{100\,\mathrm{GeV}/c^2}$	$0.019 \times \frac{m_{\tilde{\tau}_L}}{100\,\mathrm{GeV}/c^2}$	-
132	$0.062 \times \frac{m_{\tilde{\mu}_R}}{100\,\mathrm{GeV}/c^2}$	$0.28 \times \frac{m_{\tilde{\tau}_L}}{100\,\mathrm{GeV}/c^2}$	-
133	$0.0060\sqrt{m_{\tilde{\tau}}/100\,\mathrm{GeV}/c^2}$	$1.4 \times 10^{-3}\sqrt{m_{\tilde{b}}/100\,\mathrm{GeV}/c^2}$	-
211	-	$0.059 \times \frac{m_{\tilde{d}_R}}{100\,\mathrm{GeV}/c^2}$	-
212	-	$0.059 \times \frac{m_{\tilde{s}_R}}{100\,\mathrm{GeV}/c^2}$	(1.23)
213	-	$0.059 \times \frac{m_{\tilde{b}_R}}{100\,\mathrm{GeV}/c^2}$	(1.23)
221	-	$0.18 \times \frac{m_{\tilde{s}_R}}{100\,\mathrm{GeV}/c^2}$	-
222	-	$0.21 \times \frac{m_{\tilde{s}_R}}{100\,\mathrm{GeV}/c^2}$	-
223	-	$0.21 \times \frac{m_{\tilde{b}_R}}{100\,\mathrm{GeV}/c^2}$	(1.23)
231	$0.070 \times \frac{m_{\tilde{e}_R}}{100\,\mathrm{GeV}/c^2}$	$0.18 \times \frac{m_{\tilde{b}_R}}{100\,\mathrm{GeV}/c^2}$	-
232	$0.070 \times \frac{m_{\tilde{\mu}_R}}{100\,\mathrm{GeV}/c^2}$	0.56	-
233	$0.070 \times \frac{m_{\tilde{\tau}_R}}{100\,\mathrm{GeV}/c^2}$	$0.15\sqrt{m_{\tilde{b}}/100\,\mathrm{GeV}/c^2}$	-
311	-	$0.11 \times \frac{m_{\tilde{d}_R}}{100\,\mathrm{GeV}/c^2}$	-
312	-	$0.11 \times \frac{m_{\tilde{s}_R}}{100\,\mathrm{GeV}/c^2}$	0.50
313	-	$0.11 \times \frac{m_{\tilde{b}_R}}{100\,\mathrm{GeV}/c^2}$	0.50
321	-	$0.52 \times \frac{m_{\tilde{d}_R}}{100\,\mathrm{GeV}/c^2}$	-
322	-	$0.52 \times \frac{m_{\tilde{s}_R}}{100\,\mathrm{GeV}/c^2}$	-
323	-	$0.52 \times \frac{m_{\tilde{b}_R}}{100\,\mathrm{GeV}/c^2}$	0.50
331	-	0.45	-
332	-	0.45	-
333	-	0.45	-

Table 4.1: 2σ limits on the magnitudes of weak trilinear R-parity violating couplings from indirect decays and perturbativity. The explicit dependence on the relevant sparticle mass is shown. The figures in parenthesis are obtained from perturbative bounds [54].

Table 4.1 shows the upper bounds on the size of the couplings λ, λ', λ'' [54]. Here, $X = (m_{\tilde{e}}/100\,\mathrm{GeV}/c^2)^2 \times (m_{\tilde{\chi}^0}/100\,\mathrm{GeV}/c^2)^2$ and $\tilde{H}$ is a hadronic scale and can be varied from 0.003 to $1\,\mathrm{GeV}/c^2$ and $\left(\frac{M_{\tilde{q}}}{\tilde{H}}\right)^{5/2}$ from 2×10^{11} to 10^5. The most stringent limits which are heavily influenced by results from proton decay experiments [25] require that

$$\begin{aligned} \lambda_{133} &< 0.006\sqrt{\left(\frac{M_{\tilde{\tau}}}{100\,\mathrm{GeV}/c^2}\right)} \\ \lambda'_{133} &< 0.0014\sqrt{\left(\frac{M_{\tilde{b}}}{100\,\mathrm{GeV}/c^2}\right)} \\ \lambda''_{112} &< 10^{-15} \times \left(\frac{M_{\tilde{q}}}{\tilde{H}}\right)^{5/2} . \end{aligned} \tag{4.1}$$

In Table 4.1, the following bounds were derived from the following processes:

- $\lambda_{121},\ \lambda_{122},\ \lambda_{123}$, from charged current universality [55].
- $\lambda_{131},\ \lambda_{132},\ \lambda_{231},\ \lambda_{232}$ and λ_{233} [55] from measurements of $R_\tau = \Gamma(\tau \to e\nu\bar{\nu})/\Gamma(\tau \to \mu\nu\bar{\nu})$ and $R_{\tau\mu} = \Gamma(\tau \to \mu\nu\bar{\nu})/\Gamma(\tau \to e\nu\bar{\nu})$ [1].
- λ_{133} [56] from the experimental limit on the electron neutrino mass [1].
- $\lambda'_{112},\ \lambda'_{113},\ \lambda'_{121},\ \lambda'_{122}$ and λ'_{123} from charged current universality [55].
- λ'_{111} from neutrinoless double beta decay [57].
- λ'_{131} from atomic parity violation [55, 58].
- λ'_{132} from the forward-backward asymmetry in e^+e^- collisions [55].
- $\lambda'_{211},\ \lambda'_{212},\ \lambda'_{213}$ from $R_\pi = \Gamma(\pi \to e\nu)/\Gamma(\pi \to \mu\nu)$ [55].
- $\lambda'_{222},\ \lambda'_{223}$ from the D-meson decays, $D \to Kl\nu$.
- $\lambda'_{232},\ \lambda'_{331},\ \lambda'_{332},\ \lambda'_{333}$ from $R_l = \Gamma(Z \to had)/\Gamma(Z \to l\bar{l})$ for $m_{\tilde{q}} = 100\,\mathrm{GeV}/c^2$ [59].

- $\lambda'_{311},\ \lambda'_{312},\ \lambda'_{313}$ from $R_{\tau\pi} = \Gamma(\tau \to \pi\nu_\tau)/\Gamma(\pi \to \mu\nu_{mu})$ [55].
- $\lambda'_{321},\ \lambda'_{322},\ \lambda'_{323}$ from D_s decays, i.e. $R_{D_s} = \Gamma(D_s \to \tau\nu_\tau)/\Gamma(D_s \to \mu\nu_\mu)$.
- λ''_{112} from double nucleon decay [26].
- λ''_{113} from neutron oscillations [60, 26] for $m_{\tilde{q}} = 100\,\mathrm{GeV}/c^2$.
- λ''_{3jk} from $R_l = \Gamma(Z \to had)/\Gamma(Z \to l\bar{l})$ at 1σ for $\tilde{m} = 100\,\mathrm{GeV}/c^2$ [61].

The coupling strength determines the mean decay length of direct decays of the LSP. For example, for decays via an $LL\bar{E}$ coupling, the decay length [62] is given by:

$$\begin{aligned} L_\chi(cm) &= 0.3\lambda^{-2}\left(\frac{M_{\tilde{f}}}{100\,\mathrm{GeV}/c^2}\right)^4\left(\frac{\mathrm{GeV}/c^2}{M_\chi}\right)^5(\beta\gamma) \\ L_{\tilde{l}}, L_{\tilde{\nu}}(cm) &= 10^{-12}\lambda^{-2}\left(\frac{\mathrm{GeV}/c^2}{M_{\tilde{l},\tilde{\nu}}}\right)(\beta\gamma) \end{aligned} \tag{4.2}$$

for neutralino and slepton/sneutrino decays respectively, where L is the decay length and the Lorentz factor is $\beta\gamma = p/M$.

This influences how far from the interaction point the LSP will travel before it decays. This has important phenomenological consequences that are relevant to this analysis. As illustrated in Fig. 4.1, the LSP may decay within the detector, i.e. in the region $0 < \mathrm{L} < 3\mathrm{m}$ or it may decay outside the detector ($\mathrm{L} > 3\mathrm{m}$). For cases where the LSP is neutral and decays outside the detector, the signatures are identical to R-parity conserving signals. For cases where the LSP is charged, the signature would resemble heavy stable charged signatures. If the LSP decays within the detector in the region $1\mathrm{cm} < \mathrm{L} < 3\mathrm{m}$, displaced vertices would be produced. The last possibility is that the LSP would decay within the detector but with a mean decay length of less than 1cm. In this case, the particle would have negligible lifetime and would hence restrict sensitivity to neutralino masses exceed-

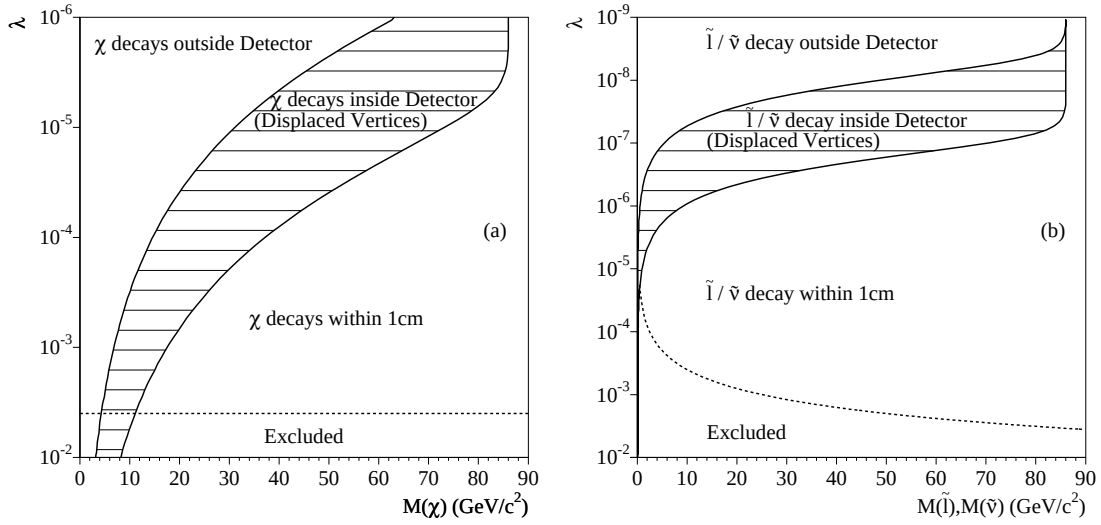

Figure 4.1: Regions in the $(\tilde{M}, \lambda)$ - plane where pair-produced LSPs are produced and have a mean decay length L of L < 1cm, 1cm < L < 3m (displaced vertices), and 3m < L (the LSP decays outside the ALEPH detector) for (a) neutralinos (with $m_{\tilde{f}} = 100\,\mathrm{GeV}/c^2$)and (b) sleptons and sneutrinos. The dashed lines show the low energy limit on λ_{133} from Eq. 4.1. The plots are taken from [62].

ing $M_{\tilde{\chi}} \gtrsim 10\,\mathrm{GeV}/c^2$ with the result that in regions close to the kinematic limit, gauginos can be probed down to $\lambda \gtrsim 10^{-5}$ for $M_{\tilde{f}} = 100\,\mathrm{GeV}/c^2$, and sleptons and sneutrinos down to $\lambda \gtrsim 10^{-7}$.

In this analysis, the neutralino is assumed to have negligible lifetime, i.e. it has a decay length of less than 1cm. This means that only masses greater than $10\,\mathrm{GeV}/c^2$ are considered.

4.2 Limits from collider searches

In this section, the existing limits from direct searches at collider experiments are briefly reviewed. All direct searches have assumed that the supersymmetric particles decay very close to the interaction point, i.e. within 1cm.

4.2.1 Sfermions

Collider searches have been carried out for pair produced sparticles [63] which decay via $LL\bar{E}$, $LQ\bar{D}$ or $\bar{U}\bar{D}\bar{D}$ couplings at all the detectors at LEP [63, 64, 65, 66, 67, 68]. Searches using data at centre-of-mass energies up to 172 GeV [62] were extended and applied to new data up to 202 GeV and the results published in [69]. The

	Lower mass limit (GeV/c^2)					
	$LL\bar{E}$		$LQ\bar{D}$		$\bar{U}\bar{D}\bar{D}$	
Sparticle	Direct	Indirect	Direct	Indirect	Direct	Indirect
$\tilde{\mathrm{t}}$	-	91	97	85	-	71.5
$\tilde{\mathrm{b}}$	-	90	-	80	-	71.5
$\tilde{\mathrm{e}}_R$	87	96	-	93	-	94
$\tilde{\mu}_R$	96	96	-	90	-	85
$\tilde{\nu}_e$	100	98	-	91	-	88
$\tilde{\nu}_{\mu,\tau}$	89	83	79	78	-	65

Table 4.2: The lower mass limits at 95% confidence level for sparticles decaying via each of the three R-parity violating couplings.

most current results are published in [70]. The limits on sfermions were obtained as bounds on sparticle masses. These limits are summarized in Table 4.2.

4.2.2 Gauginos

Searches from LEP I excluded the chargino at masses below 45.6 GeV/c^2 [75]. At LEP II, this was extended to higher energies [63, 69, 70] to exclude chargino masses below 103 GeV/c^2 for large scalar masses ($m_0 = 500$ GeV/c^2) and $\tan\beta = \sqrt{2}$. This limit is valid for all μ and M_2 irrespective of the R-parity violating operator. Direct searches have been carried out for the neutralino for decays via $LL\bar{E}$ couplings in all regions of parameter space with the exception that $\tan\beta$ was restricted to $\tan\beta = \sqrt{2}$ [62]. Existing limits for the lightest and second lightest neutralino decays via the $LL\bar{E}$ operator excludes the lightest neutralino at masses below 23 GeV/c^2. There are no existing limits from direct searches for the neutralino for

decays via $LQ\bar{D}$ and $\bar{U}\bar{D}\bar{D}$ couplings.

In this analysis, searches are done to cover all μ, $\tan\beta$, m_0 and M_2 as explained in chapter 5, for decays via $LL\bar{E}$, $LQ\bar{D}$ and $\bar{U}\bar{D}\bar{D}$ couplings.

4.3 Limits from Γ_Z

Particles with masses less than $45\,\mathrm{GeV}/c^2$ that couple to the Z boson cause an increase in the total Z width, Γ_Z. The total Z width has been measured with great precision at LEP [28] and this measurement is in very good agreement with the Standard Model. This agreement can be interpreted as bounds on new physics coupling to the Z boson. Limits are determined by using the interval obtained from comparing results from the Standard Model which is set as a lower bound and results from experiments as an upper bound. Measurements on observables such as the strong coupling constant, α_s, and the top quark mass, m_t, are used to determine a Standard Model prediction. A theoretical lower limit is obtained by taking advantage of the uncertainty introduced from the error on input variables. A 95% confidence level limit is determined assuming that the probability of Γ_Z being less than the Standard Model bound is zero. Limits on supersymmetric models are then derived with the assumption that each channel saturates the bound by itself.

Calculation of Γ_Z

The differential cross section for fermion pair production at centre-of-mass energies close to the Z resonance consists of three s-channel contributions: Z exchange, photon exchange and an interference term. The Z exchange term can be described in a model independent manner by the Breit-Wigner resonance [1]

$$\sigma_{f\bar{f}}(s) = \frac{s}{(s - M_Z^2)^2 + s^2\Gamma_Z^2/M_Z^2}\frac{12\pi\Gamma_{ee}\Gamma_{f\bar{f}}}{M_Z^2}, \tag{4.3}$$

where s is the centre-of-mass energy squared, M_z is the Z mass, Γ_Z is the total Z width and Γ_{ee} and $\Gamma_{f\bar{f}}$ are the partial widths of e^+e^- and $f\bar{f}$ respectively. The Z exchange term is dominant over the other two terms, each of which provides small corrections. The photon exchange term can be evaluated in the framework of QED, a well tested theory and as such this assumption does not significantly compromise the model independence of the approach. The interference term cannot be written as a function of the Breit-Wigner parameters even if QED is assumed. The Standard Model value of this term is assumed, and since it is small, it only introduces a small level of model dependence. The resulting expressions for the cross sections are corrected for initial and final state radiation.

The determination of Γ_Z is obtained [28] by measuring the cross sections for fermion pair production at a number of centre-of-mass energies around the Z resonance and fitting the $\sqrt{s}$ dependence using the method outlined above. This gives the result

$$\Gamma_Z^{exp} = 2495.6 \pm 1.6\,\mathrm{MeV}. \tag{4.4}$$

This is a nearly model independent determination of Γ_Z and as such can be used to place bounds on possible extensions of the Standard Model.

In order to determine the Standard Model prediction of Γ_Z, the program ZFITTER [71] was used. The calculation of Γ_Z depends on the strong coupling constant, α_s, the Higgs mass, m_H, the electromagnetic coupling constant, α_{em}, the bottom quark mass, m_b and the top quark mass, m_t. The variables and their allowed ranges are:

- m_t: $174.3 \pm 5.1\,\mathrm{GeV}/c^2$.
- m_H: $60 < m_H < 150\,\mathrm{GeV}/c^2$.
- α_s: 0.118 ± 0.003.

- α_{em}^{-1}: 128.896 ± 0.090.
- m_b: $4.7 \pm 0.3\,\mathrm{GeV}/c^2$.

The values of m_t, α_{em}^{-1} and α_s are taken from [28]. The value of m_t is derived from the latest results from the CDF [72, 73] and DØ [74] experiments. At LEP, results using measurements from R_l, the ratio of the partial width of the Z for decays into hadrons (Γ_{had}) to the decay into a pair of charged leptons (Γ_{ll}) [28], show α_s to have a value of 0.123 ± 0.004. However measurements from the leptonic pole cross section, σ_l^0, which is defined as [28]

$$\sigma_l^0 \equiv \frac{12\pi\Gamma_{ll}^2}{m_Z^2\Gamma_Z^2}, \tag{4.5}$$

and has higher sensitivity to QCD corrections, show α_s to have a value of 0.118 ± 0.003. This is in very good agreement with the world average of $\alpha_s(m_Z^2) = 0.119 \pm 0.002$ [1]. In the MSSM, the lightest Higgs mass is constrained to be less than the Z mass at tree level. However, large radiative corrections can shift its mass to $120 - 130\,\mathrm{GeV}$ [19]. In the MSSM, a conservative upper bound on the Higgs mass is $150\,\mathrm{GeV}/c^2$.

The contributions to the error are combined in quadrature with the exception of the Higgs mass and α_s which are assumed to be correlated. This leads to the following Standard Model prediction:

$$\Gamma_Z^{SM} = 2494.4 \pm 2.4\,\mathrm{MeV}. \tag{4.6}$$

Contribution to the Z width is then determined by:

- Using Eq. (4.6) to define a 1σ lower bound of $\Gamma_Z^{SM} > 2492.0\,\mathrm{MeV}$.
- Using Eq. (4.4) which is assumed to have a Gaussian distribution with the exception of the region below the Standard Model bound, to establish an

upper bound at 95% confidence level to obtain $\Gamma_Z < 2498.7\,\mathrm{MeV}$.

- The contribution is obtained from the difference between the upper and lower bounds, $\Gamma_Z^{SUSY} = \Gamma_Z - \Gamma_Z^{SM}$ to give $6.7\,\mathrm{MeV}$.

In the context of MSSM, the limit from Γ_Z is interpreted to mean that all points in the μ, $\tan\beta$, m_0 and M_2 parameter space are excluded for sparticle masses contributing greater than $6.7\,\mathrm{MeV}$ to the Z width. This in addition to implementation of limits from sfermion and gaugino searches, forms the first step in the methodology behind searches for the LSP in parameter space, and is described in section 5.1.

Chapter 5

Methodology

In order to carry out searches for signal, parameter space is scanned and at each point, MSSM parameters such as sparticle masses, branching ratios and cross sections are computed. Constraints from existing searches are implemented to exclude points. Events are generated at selected points and searches for signal carried out. The purpose of this analysis is to carry out searches for the LSP. The possible LSP candidates are the gluino, chargino, squark, slepton and sneutrino and neutralino. The gluino is disqualified from being the LSP by virtue of the fact that the gaugino masses are assumed to be universal at GUT scale [6, 22]. This makes it too heavy to play a role in the phenomenology at LEP. Searches at LEP I have disqualified the chargino as the LSP [75]. Squark LSPs are not considered in the case of $LL\bar{E}$ couplings as they cannot decay via the purely leptonic $LL\bar{E}$ operator. Instead they would need to undergo a four-body decay, thus acquiring a substantial lifetime. This would fall outside the assumption made in section 4.1 for negligible lifetime. This leaves squarks decaying via $LQ\bar{D}$ and $\bar{U}\bar{D}\bar{D}$ couplings, sleptons, sneutrinos and neutralinos as the only LSP candidates.

In this chapter the process of scanning over parameter space and selecting points to generate events for analysis is reviewed. The process of setting limits using

information from the signal, background and data is explained.

5.1 Scan of parameter space

A four-dimensional scan of the MSSM parameter space was carried out to cover the regions of μ, $\tan\beta$, m_0 and M_2. This was done using an iterative process which kept $\tan\beta$ and m_0 fixed in the step sizes shown in Table 5.1 and divided μ and M_2 into forty step sizes each. This resulted in a four-dimensional $\mu - \tan\beta - m_0 - M_2$ space consisting of $\approx 400,000$ points. At each point, the masses, cross section and contribution to Γ_Z of the MSSM particles were calculated using using a collection of Fortran subroutines kept in a library called the MSMLIB, which used as input, the MSSM parameters μ, $\tan\beta$, m_0, M_2, the gauge unification condition Eq. (2.8), the CP-odd neutral Higgs mass, m_{A^0}, the trilinear couplings and Standard Model constants such as M_Z, m_t, α_s, α_{em},.., etc. The trilinear coupling was set to be zero. All masses and cross sections were calculated to two-loop radiative corrections. The regions of parameter space scanned were split into sections to enable manipulation of the huge data set involved. The data sets were stored in ntuples and contained a list of every four-dimensional $\mu - \tan\beta - m_0 - M_2$ point and the masses, cross section and contribution to the Z width of all MSSM sparticles at each point.

In this analysis, the lowest value of $\tan\beta$ used was two. This limit has been set using constraints from Higgs searches [78] which have shown that in the MSSM, the neutral CP-even Higgs mass, m_h, and the neutral CP-odd mass, m_{A^0}, are both excluded for masses less than $89.6\,\mathrm{GeV}/c^2$ and $90.0\,\mathrm{GeV}/c^2$ at 95% confidence level respectively. For a scenario where there is mixing in the $\tilde{t}$ sector, $\tan\beta$ can be excluded between 0.7 and 2.3 as illustrated in Fig. 5.1.

$\tan\beta$ (step size)	m_0 (step size) GeV/c^2	μ GeV/c^2	m_2 GeV/c^2
2 - 4(1)	0 - 50(10)	-200 : +200	0 - 500
2 - 4(1)	60 - 100(10)	-200 : +200	0 - 500
2 - 4(1)	200 - 500(100)	-200 : +200	0 - 500
5 - 7(1)	0 - 50(10)	-200 : +200	0 - 500
5 - 7(1)	60 - 100(10)	-200 : +200	0 - 500
5 - 7(1)	200 - 500(100)	-200 : +200	0 - 500
8 - 10(1)	0 - 50(10)	-200 : +200	0 - 500
8 - 10(1)	60 - 100(10)	-200 : +200	0 - 500
8 - 10(1)	200 - 500(100)	-200 : +200	0 - 500
20 - 50(10)	0 - 50(10)	-200 : +200	0 - 500
20 - 50(10)	60 - 100(10)	-200 : +200	0 - 500
20 - 50(10)	200 - 500(100)	-200 : +200	0 - 500

Table 5.1: Region of the MSSM parameter space scanned. The scan consisted of approximately 400000 points. In the third column, μ ranges from $-200\,\mathrm{GeV}/c^2$ to $+200\,\mathrm{GeV}/c^2$.

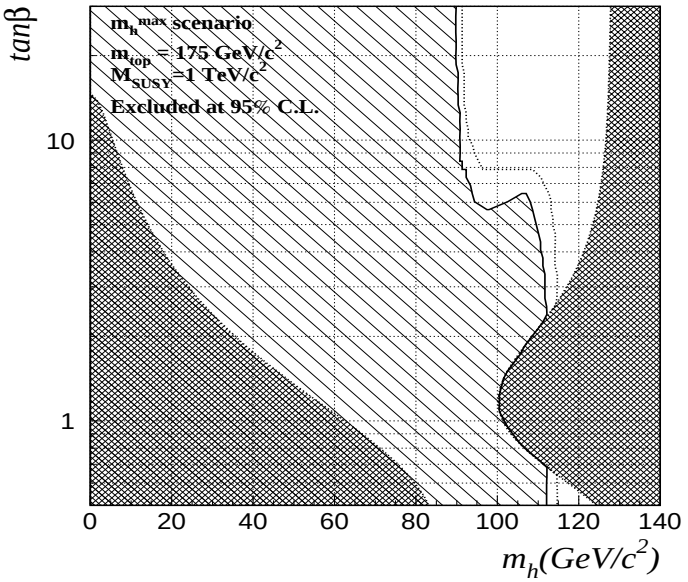

Figure 5.1: Constraints on $\tan\beta$ in the maximal mixing m_h^{max} benchmark scenario. In this scenario, supersymmetric parameters are chosen such that the maximum possible Higgs boson mass as a function of $\tan\beta$ is obtained. The lightly-hatched area is excluded experimentally. The dotted line indicates the expected exclusion limit. The dark-hatched areas indicate theoretically forbidden parts of parameter space. This plot was taken from [78].

After the scan of parameter space, the following steps were carried out:

- Limits from the Z width measurements were implemented. This constrains parameter space by excluding all points in parameter space in which the MSSM particles (sfermions and gauginos) have masses that would contribute greater than $6.7\,\mathrm{MeV}/c^2$ to the width of the Z boson.

- Parameter space was constrained further by implementing limits from sfermion searches (section 4.2). As a result, all points with sfermion masses less than the masses listed in Table 4.2 are excluded.

- Finally, the remaining sfermion and gaugino masses were compared at each of the remaining points to determine which particle is the LSP. There were no points for which $m_{sfermions} < m_{\tilde{\chi}_1^0}$. This leaves $\tilde{\chi}_1^0$ as the only LSP candidate.

Constraining parameter space reduced the number of points to be covered in the analysis. The implementation of limits from the Z width measurements reduced the number of points from $\approx 400,000$ to $\approx 93,000$ points. Implementing limits from sfermion searches reduced this further to $\approx 78,000$ points. This includes the exclusion of points for $m_{\tilde{\chi}_1^0} < 10\,\mathrm{GeV}/c^2$ and for which the lightest neutralino pair $\tilde{\chi}_1^0\ \tilde{\chi}_1^0$, the lightest and next-lightest neutralino pair $\tilde{\chi}_1^0\ \tilde{\chi}_2^0$ falls outside the kinematic limit (208 GeV). The implementation of limits also resulted in the removal of points for which $10\,\mathrm{GeV}/c^2 < m_{\tilde{\chi}_1^0} < 20\,\mathrm{GeV}/c^2$. The effects of the implementation of limits on the reduction of points in parameter space can clearly be seen on comparing Figs. 5.2 and 5.4 with Figs. 5.3 and 5.5 which show plots of the production cross section of $\tilde{\chi}_1^0\ \tilde{\chi}_1^0$ and $\tilde{\chi}_1^0\ \tilde{\chi}_2^0$ as a function of the lightest neutralino mass. In Figs. 5.2 and 5.4 only limits from Z width measurements are implemented while in Figs. 5.3 and 5.5, limits from both Z width measurements and sfermion searches are implemented. Figs. 5.3 and 5.5 show that a significant proportion of the points were reduced in the region m_0: 10 — 50. This is because the mass of the sfermion

is dependent on m_0. Hence in this region the sfermions have low mass at majority of the points.

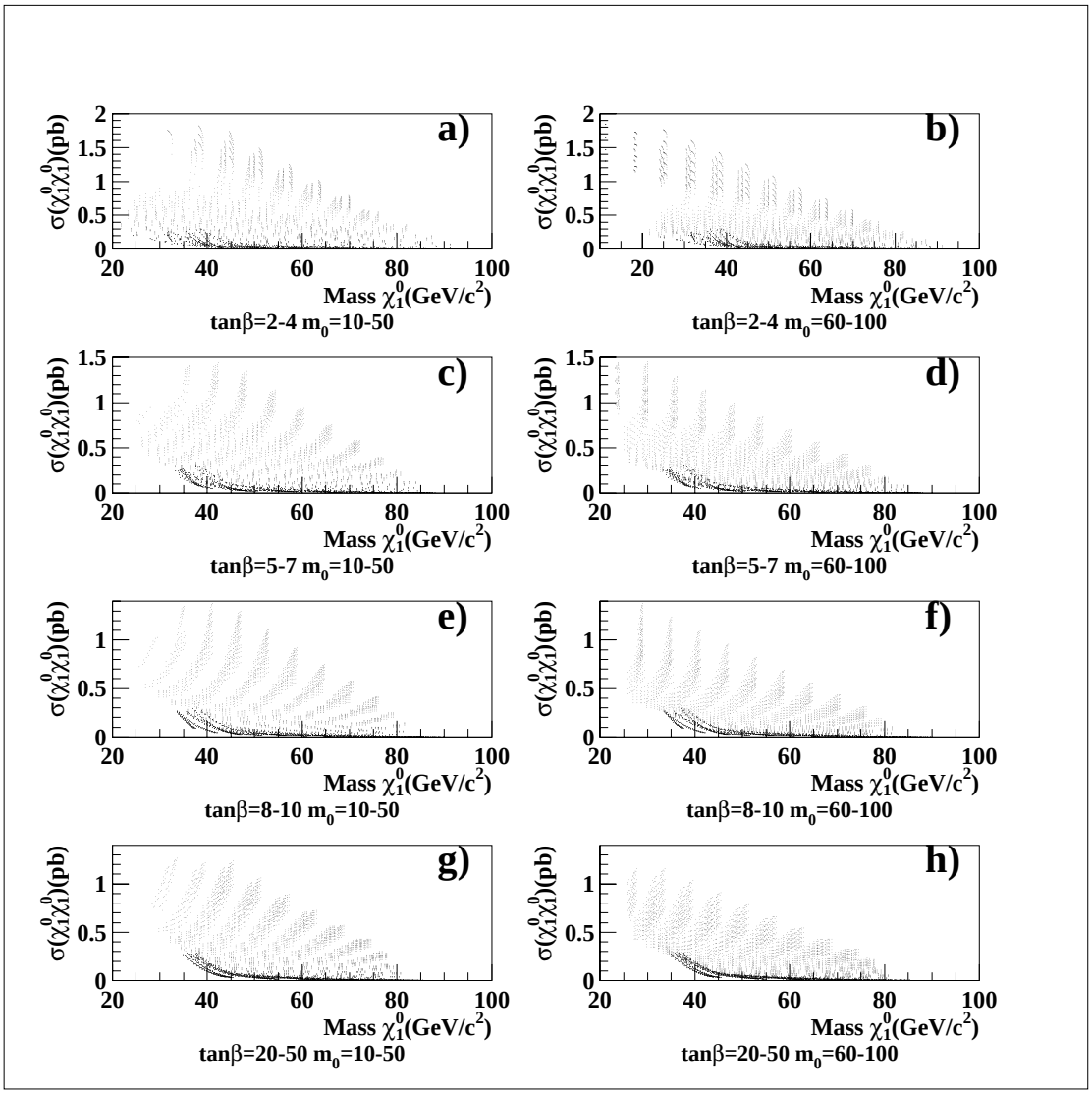

Figure 5.2: The production cross section of the lightest neutralino pair as a function of $m_{\tilde{\chi}_1^0}$ after the implementation of constraints from the Z width. Each plot represents a region of $\tan\beta$ and m_0 scanned. In each region, all μ and M_2 were covered.The distinct bands are as a result of single M_2 values for all μ with M_2 increasing in the direction of increasing $m_{\tilde{\chi}_1^0}$.

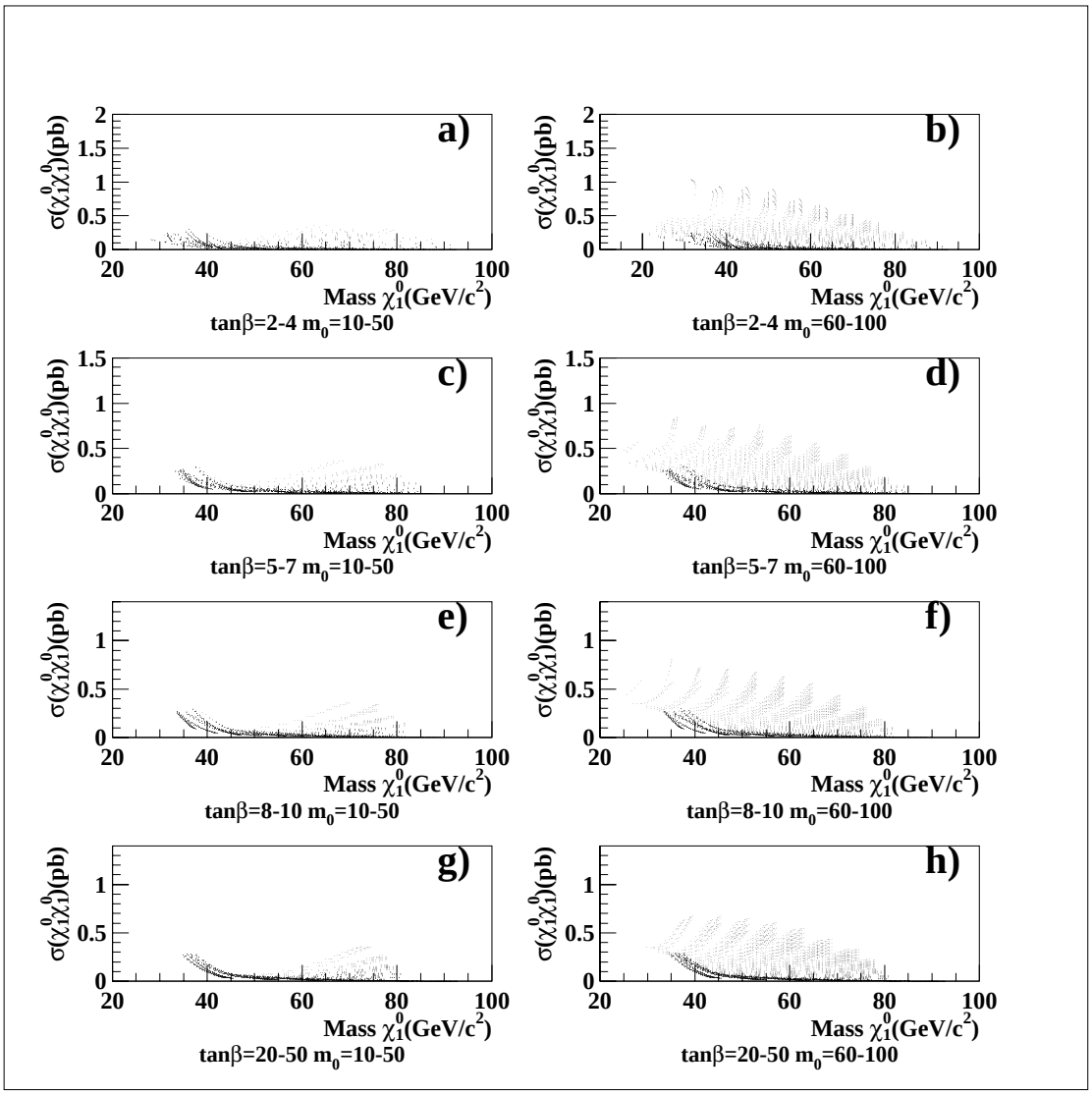

Figure 5.3: The production cross section of the lightest neutralino pair as a function of $m_{\tilde{\chi}_1^0}$ which was used for the $LL\bar{E}$ analysis. The plots were obtained after the implementation of constraints from sfermion searches and the Z width. A fine scan was done to select points with the lowest production cross section as a function of mass. Each plot represents a region of $\tan\beta$ and m_0 scanned. In each region, all μ and M_2 were covered. The distinct bands are as a result of single M_2 values for variable μ with M_2 increasing in the direction of increasing $m_{\tilde{\chi}_1^0}$.

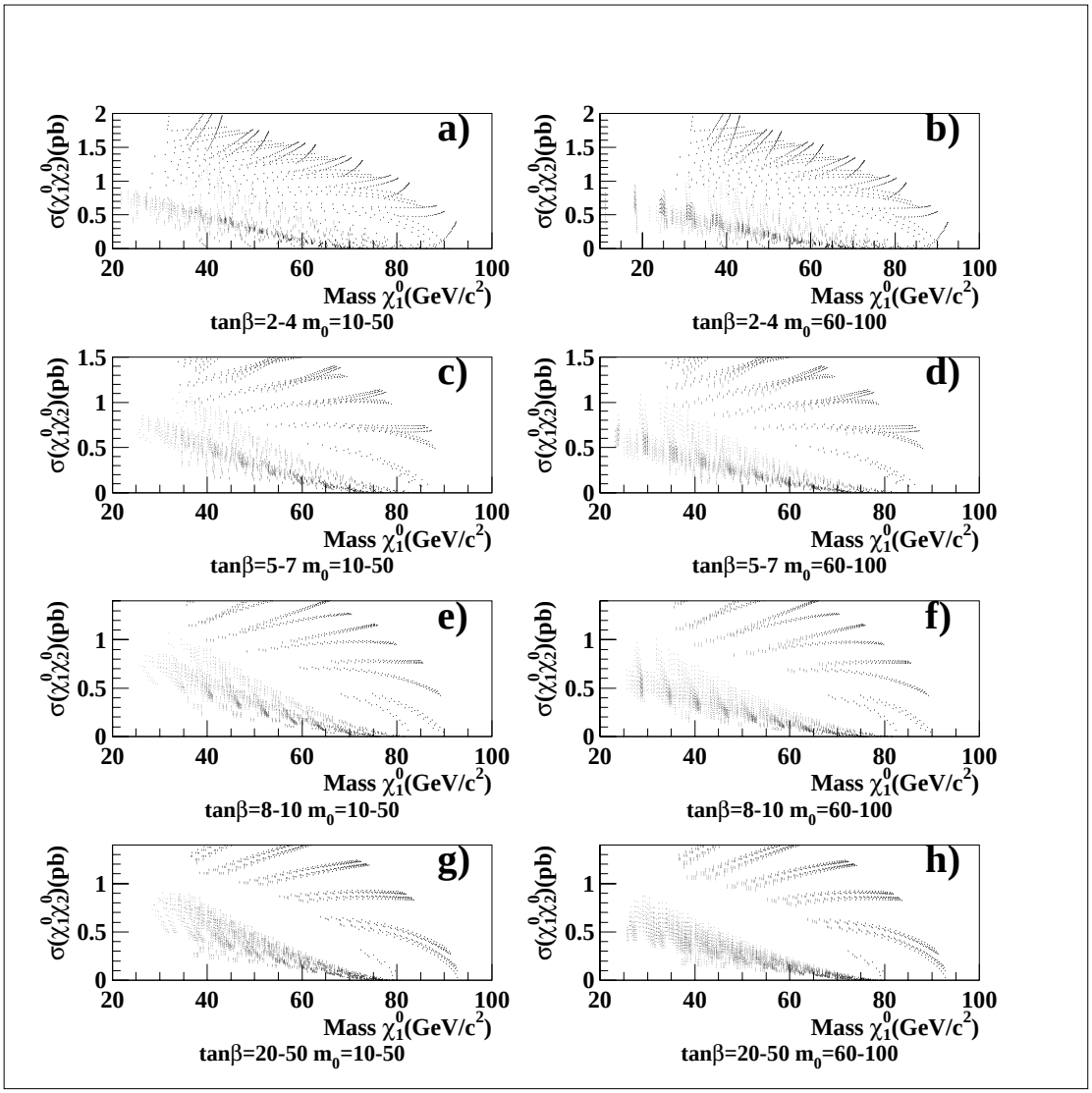

Figure 5.4: The production cross section of the lightest and second lightest neutralino pair as a function of $m_{\tilde{\chi}_1^0}$ after the implementation of constraints from the Z width . Each plot represents a region of $\tan\beta$ and m_0 scanned. In each region, all μ and M_2 were covered. Two distinct group of bands can be seen in the plots. The first group of bands at the upper half of the plots are as a result of single μ values for variable m_2 values with μ increasing in the direction of increasing $m_{\tilde{\chi}_1^0}$. The second group of bands at the lower half of the plots are a result of single M_2 values for variable μ with M_2 increasing in the direction of increasing $m_{\tilde{\chi}_1^0}$.

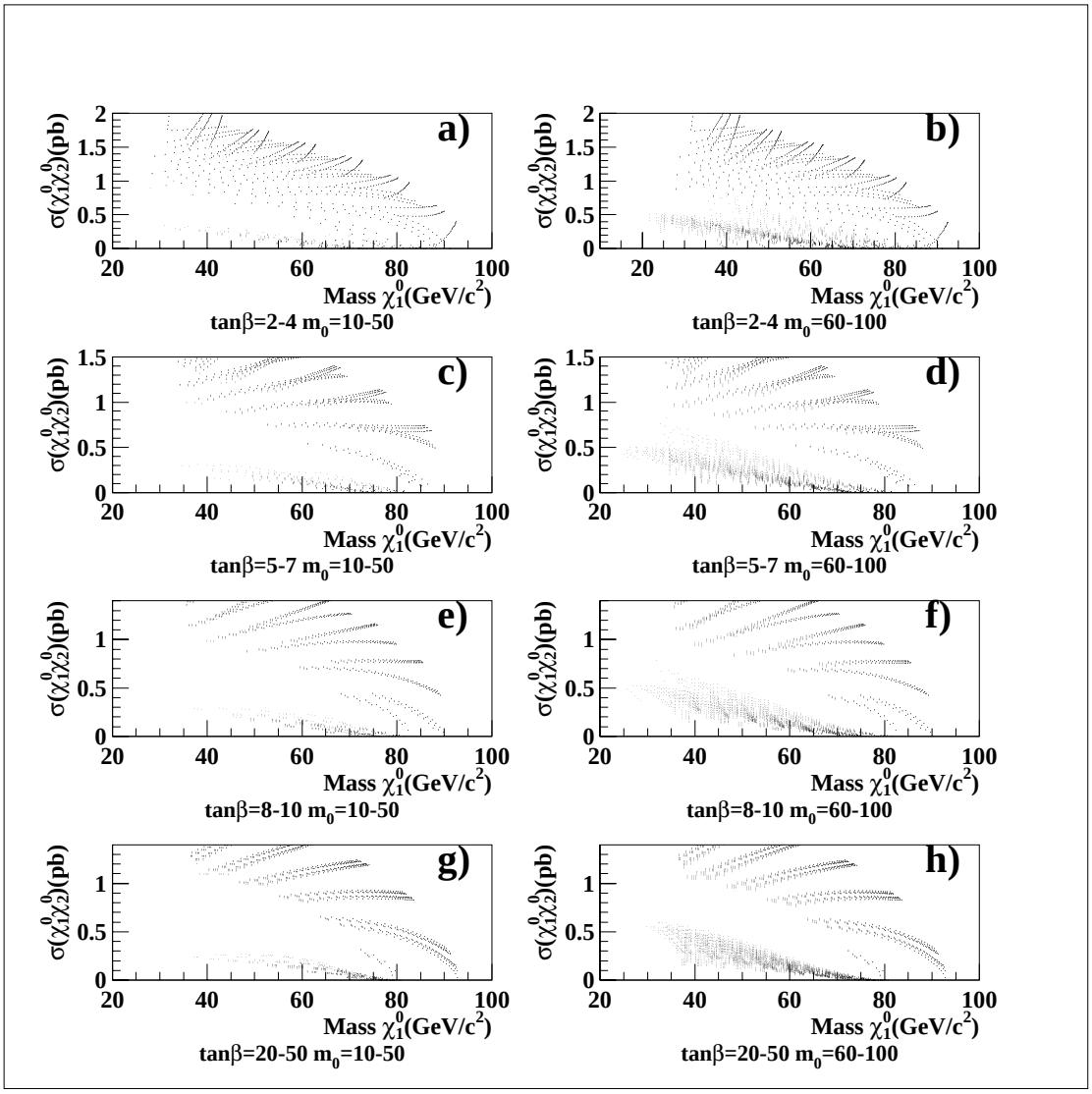

Figure 5.5: The production cross section of the lightest and second lightest neutralino pair as a function of $m_{\tilde{\chi}_1^0}$ which was used for the $LL\bar{E}$ analyses. The plots were obtained after the implementation of constraints from sfermion searches and the Z width. A fine scan was done to select points with the lowest production cross section as a function of mass. Each plot represents a region of $\tan\beta$ and m_0 scanned. In each region, all μ and M_2 were covered. Two distinct group of bands can be seen in the plots. The first group of bands at the upper half of the plots are as a result of single μ values for variable m_2 values with μ increasing in the direction of increasing $m_{\tilde{\chi}_1^0}$. The second group of bands at the lower half of the plots are a result of single M_2 values for variable μ with M_2 increasing in the direction of increasing $m_{\tilde{\chi}_1^0}$.

5.2 Selection of points for analysis

Pair produced neutralino events were generated at points in Fig. 5.3 in regions which gave the lowest cross section as a function of mass. This would mean that any point excluded would also exclude all other points for the given mass with larger cross sections. At each point selected, pair produced $\tilde{\chi}_1^0\ \tilde{\chi}_1^0$ events were generated and selections, which are obtained as described in section 6.2, were applied to the signal, background and data. The results obtained were used to derive limits as explained in the next section. In order to increase sensitivity to searches, pair produced $\tilde{\chi}_1^0\ \tilde{\chi}_2^0$ events were generated and analysed in a manner analogous to $\tilde{\chi}_1^0\ \tilde{\chi}_1^0$ events using points selected in Fig. 5.5. The increase in production cross section of $\tilde{\chi}_1^0\ \tilde{\chi}_2^0$ compared to $\tilde{\chi}_1^0\ \tilde{\chi}_1^0$ enabled greater sensitivity to the neutralino searches. Points in Figs. 5.3 and 5.5 were used to carry out searches for decays via $LL\bar{E}$ couplings. This because the sfermion limits implemented to produce the plots were from sfermion decays via the $LL\bar{E}$ coupling. For decays via $LQ\bar{D}$ and $\bar{U}\bar{D}\bar{D}$ couplings, the corresponding limits were implemented in Figs. 5.2 and 5.4 to obtain the appropriate plots and the process of selection of points for analysis was repeated.

In regions for which m_0 was high, i.e. $m_0 \geq 200\,\mathrm{GeV}/c^2$, the production cross section of the neutralino was too low to be sensitive to signal. Chargino searches were carried out in these regions in a manner analogous to the neutralino searches and results were used to set bounds on the mass of the lightest neutralino. This was done by using plots of the production cross section of the lightest chargino pair $\tilde{\chi}_1^+\ \tilde{\chi}_1^-$ as a function of its mass as shown in Fig. 5.6, and selecting points at the lowest cross section for a given mass. Monte Carlo signal events were generated at all of the points selected and selections, which are obtained as described in section 6.2, were applied to the signal, background and data. The results obtained were used to derive limits as explained in the next section. The limits were used to set

bounds on the mass of the lightest neutralino.

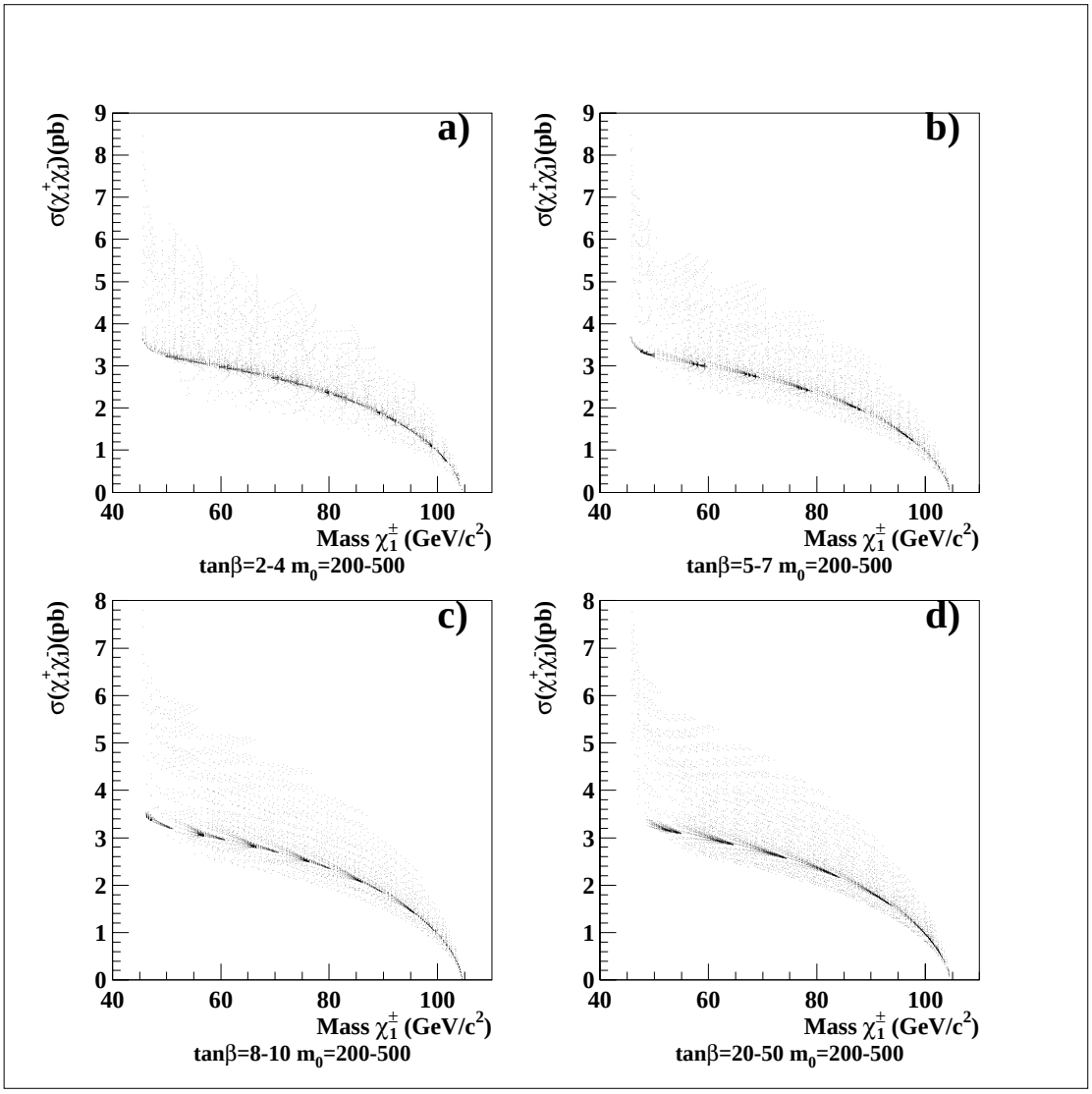

Figure 5.6: The production cross section of the lightest chargino pair as a function of $m_{\tilde{\chi}_1^\pm}$ which was used for the $LL\bar{E}$, $LQ\bar{D}$ and $\bar{U}\bar{D}\bar{D}$ analyses. The plots were obtained after the implementation of constraints from sfermion searches and the Z width. A fine scan was done to select points with the lowest production cross section as a function of mass. The plots were obtained after the implementation of constraints from sfermion searches and the Z width. Each plot represents a region of $\tan\beta$ and m_0 scanned. In each region, all μ and M_2 were covered.

5.3 Setting limits

Chapter 7 discusses the limits derived following the procedure discussed in section 5.2. In this section, the way in which cross section limits at 95% confidence level are set, is discussed.

The standard technique used for searches at LEP is a two step process. First, the output from JULIA is passed through the ALEPH Physics Analysis package (ALPHA) [76]. ALPHA includes an extensive set of utility routines such as secondary vertex finding and b quark tagging. Preliminary event candidates are identified using some simple preselection. Physical variables are then calculated for events satisfying the preselection. The physical variables calculated are designed to be sensitive to the differences between signal and background. The variables are written to HBOOK [77] ntuples forming a much reduced data set. HBOOK ntuples are tables of data in which rows correspond to successive events and columns to variables. The signal, background and real data are treated and stored via exactly the same process as explained in section 3.8.

The second step is the application of selections (section 6.2) to the ntuples. The selections are made up of *cuts*. A cut is a constraint made on one or more physical variable and is designed to distinguish between the signal and background.

Application of selections to signal ntuples yields efficiency values $\mathcal{E}$, where efficiency is defined as the ratio of the number of events that pass the selections to the total number of events generated.

Selections are applied to background ntuples and the number of events that pass are normalized to the luminosity of the ALEPH data to give $N_{bkg(SM)}$ by using

$$N_{bkg(SM)} = \frac{N_{pass(SM)}}{N_{gen(SM)}} \times \sigma_{bkg(SM)} \times \mathcal{L}, \tag{5.1}$$

where $N_{pass(SM)}$ is the number of events that pass the selection for a single Standard

Model process, $N_{gen(SM)}$ is the number of events generated for a single Standard Model process, $\sigma_{bkg(SM)}$ is the cross section for the Standard Model process at $\sqrt{s}$, $\mathcal{L}$ is the integrated luminosity of the data at $\sqrt{s}$ and $N_{bkg(SM)}$ is the number of events expected in the absence of signal for the Standard Model process. To obtain the total number of events N_{bkg} for all Standard Model processes, Eq. (5.1) is repeated for each of the Standard Model processes listed in Table 3.2 and added together.

Application of selections to data from the ALEPH detector yields the number of observed events, N_{obs}. In order to find what the expected number of events in the presence of signal N_{exp} would be, an upper limit on the expected number of signal events is obtained by using the Poisson distribution properties of N_{bkg} and N_{obs} in:

$$1-\varepsilon \;=\; 1-\frac{e^{-(N_{bkg}+N_{exp})}\sum_{n=0}^{N_{obs}}\frac{(N_{bkg}+N_{exp})^n}{n!}}{e^{-N_{bkg}}\sum_{n=0}^{N_{obs}}\frac{(N_{bkg})^n}{n!}}, \tag{5.2}$$

where ε is the confidence coefficient. In this analysis, the value of ε value is chosen to be 0.05. Thus solving Eq. (5.2) for N_{exp} would give an upper limit N_{CL} on the number of events expected in the presence of signal at 95% Confidence Level (C.L). This implies that if the experiment was performed with a mean number of signal events equal to N_{95} and the same N_{bkg}, there would exist a 95% probability of observing more than N_{obs} events with $N_{bkg} \leq N_{obs}$. An upper limit on the cross section σ_{CL} can be obtained using the formula

$$\sigma_{CL} \;=\; \frac{N_{CL}}{\mathcal{L}\mathcal{E}}, \tag{5.3}$$

where $\mathcal{L}$ is the luminosity of the data. The production cross section of the process

σ_{pr} searched for is then compared to σ_{95} and the result mapped onto the mass plane to set a limit for the point with the least mass for which $\sigma_{pr} < \sigma_{95}$.

The process of obtaining N_{95} and σ_{95} as explained above, is valid only for data collected at a specific centre-of-mass energy. For a scenario where searches are carried out over a range of energies and luminosities, a modified approach is used that was developed for previous ALEPH analyses [69]. The procedure yields a limit, σ_{lim}, on the cross section at the highest centre-of-mass energy. In this analysis, searches were carried out over a centre-of-mass energy range from $189\,\text{GeV} - 208\,\text{GeV}$ and an integrated luminosity of $623\ \text{pb}^{-1}$ (Table 3.1). The modification is as follows:

- σ_{pr} evolves as a function of $\sqrt{s}$ for a given sparticle mass. It can be represented by σ_{pr_i} where $i = 1, 2, 3, ..., 11$ for $\sqrt{s} = 189\,\text{GeV}, 192\,\text{GeV}, ..., 208\,\text{GeV}$.
- It is not necessary to generate Monte Carlo signal at $\sqrt{s}$ for all i as $\mathcal{E}_i$ does not evolve rapidly as a function of $\sqrt{s}$. A linear interpolation is done between 189 GeV and 208 GeV.
- N_{bkg_i} is obtained for all values of σ_{bkg_i}.
- N_{obs_i} is obtained by applying the selections to the ALEPH data ntuples for events generated at $\sqrt{s}$ for all i.

Finally, the required cross section limit, σ_{lim}, is evaluated at the highest centre-of-mass energy by combining the limits at all $\sqrt{s}$ for $i = 1, 2, 3, ..., 11$ and iterating towards 0.95 using:

$$0.95 = \left(1 - \frac{e^{-(N_{(bkg,i)}+N_{(exp,i)})} \sum_{n=0}^{N_{(obs,i)}} \frac{(N_{(bkg,i)}+N_{(exp,i)})^n}{n!}}{e^{-N_{(bkg,i)}} \sum_{n=0}^{N_{(obs,i)}} \frac{(N_{(bkg,i)})^n}{n!}} \right)_{i=1} \times, ..., \times \Big(\Big)_{i=11}, \tag{5.4}$$

where $N_{(exp,i)}$ is given by

$$N_{(exp,i)} = \left(\frac{\sigma_{pr\_i}}{\sigma_{lim}} \times \sigma_{pr\_i} \right) \times \mathcal{L}_i \times \mathcal{E}_i, \tag{5.5}$$

where, σ_{pr_i}, $\mathcal{L}_i$ and $\mathcal{E}_i$ are the production cross section, luminosity and efficiency at $\sqrt{s}$ for $i = 1, 2, 3, ..., 11$ and σ_{lim} is the cross section limit at 208 GeV and returns a value such that Eq. (5.4) is satisfied.

5.4 Summary

Searches for the LSP were carried out by scanning through parameter space of the MSSM, obtaining points at which $\tilde{\chi}_1^0\ \tilde{\chi}_1^0$ and $\tilde{\chi}_1^0\ \tilde{\chi}_2^0$ events were pair produced and using results from the application selections derived in chapter 6, over the signal, background and data. The results were used to obtain limits on the mass of the lightest neutralino in the absence of signal. In regions of high m_0, the production cross section of the neutralino was too low to be sensitive to signal. Chargino searches were carried out in these regions and the results were used to set bounds on the mass of the lightest neutralino.

Chapter 6

Gaugino decays and topology selections

In this analysis only the pair production of gauginos, i.e. charginos and neutralinos are considered since limits from Γ_Z and from sfermion searches exclude all points in parameter space for which $m_{sfermions} < m_{\tilde{\chi}_1^0}$. Existing limits from neutralino searches place a lower mass limit of 23 GeV/c^2 for decays via $LL\bar{E}$ coupling. There are no existing limits from direct searches for neutralino decays via $LQ\bar{D}$ and $\bar{U}\bar{D}\bar{D}$ couplings. This leaves the neutralino as the only LSP candidate. Chargino searches were carried out to cover areas of parameter space in which the neutralino cross section was not sensitive to signal.

In the previous chapter, the methodology behind the scan of parameter space, the implementation of existing limits to exclude points and the identification of points in the unexcluded regions which were used to carry out searches, were discussed. At each point selected, depending on whether it was in a high m_0 region or low m_0 region, pair produced chargino or neutralinos were generated and used to carry out searches. In this chapter the various decay modes and topologies (signal) arising from the decay of gauginos via a single dominant $LL\bar{E}$, $LQ\bar{D}$ or $\bar{U}\bar{D}\bar{D}$

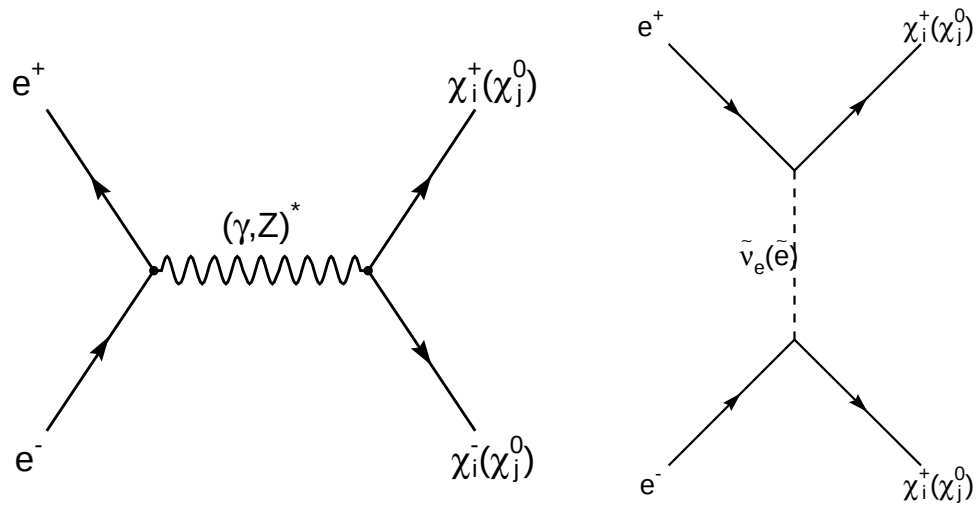

Figure 6.1: Feynman diagrams for the s-channel and t-channel production of charginos and neutralinos where $i = 1, 2$ and $j = 1, 2, 3, 4$. In the s-channel diagram, the chargino and neutralino are produced through the exchange of the γ or Z-boson. In the t-channel diagram they are produced via slepton exchange.

coupling are described. The various analyses developed to search for events with these topologies are explained.

6.1 Chargino and neutralino decays

Charginos ($\tilde{\chi}_1^{\pm}$, $\tilde{\chi}_2^{\pm}$) and neutralinos ($\tilde{\chi}_1^0$, $\tilde{\chi}_2^0$, $\tilde{\chi}_3^0$, $\tilde{\chi}_4^0$) can be pair produced via s-channel and t-channel Feynman diagrams (Fig.6.1). In the t-channel, the charginos are produced via sneutrino exchange while the neutralinos are produced via slepton exchange. For large sneutrino and slepton masses, the s-channel diagram dominates. For small sneutrino (slepton) masses, the t-channel contributions can be large, resulting in destructive (constructive) interference for the chargino (neutralino) production [79]. The production cross sections depend therefore on the chargino and neutralino masses and their couplings (and hence on $m_{i=1,2}$, μ and $\tan\beta$) as well as on the selectron and sneutrino masses. Consequently, light sneutrinos are associated with a lower production cross section for pair produced charginos

Direct Decay Mode	Sparticle	
	$\tilde{\chi}_1^+ \ \tilde{\chi}_1^-$	$\tilde{\chi}_1^0 \ \tilde{\chi}_1^0, \ \tilde{\chi}_1^0 \ \tilde{\chi}_2^0, \ \tilde{\chi}_2^0 \ \tilde{\chi}_2^0$
$\underline{LL\bar{E}}$		
λ_{ijk}	$\overbrace{\underbrace{\nu_i\nu_j l_k^+, \ l_i^+ l_j^+ l_k^-, \ l_i^+\nu_j\nu_k, \ \nu_i l_j^+\nu_k}}^{\ddagger}$	$\underbrace{\bar{\nu}_i l_j^+ l_k^-, \ \bar{\nu}_j l_i^+ l_k^-, \ \nu_i l_j^- l_k^+, \ \nu_j l_i^- l_K^+}$
	$4L + \not{E}$	$4L + \not{E}$
	$2L + \not{E}$	
	$6L$	
$\underline{LQ\bar{D}}$		
λ'_{ijk}	$\underbrace{\nu_i u_j \bar{d}_k, \ l_i^+ \bar{d}_j d_k, \ l_i^+ \bar{u}_j u_k, \ \bar{\nu}_i \bar{d}_j u_k}$	$\underbrace{l_i^- u_j \bar{d}_k, \ l_i^+ \bar{u}_j d_k, \ \nu_i d_j \bar{d}_k, \ \bar{\nu}_i \bar{d}_j d_k}$
	$4J + 1L + \not{E}$	$4J + 1L + \not{E}$
	$4J + 2L$	$4J + 2L$
	$4J + \not{E}$	$4J + \not{E}$
$\underline{\bar{U}\bar{D}\bar{D}}$		
λ''_{ijk}	$\underbrace{\bar{u}_i \bar{d}_j \bar{u}_k, \ u_i u_j d_k, \ u_i d_j u_k}$	$\underbrace{\bar{u}_i \bar{d}_j \bar{d}_k, \ u_i d_j d_k}$
	$6J$	$6J$

Table 6.1: Direct R-parity violating decay modes for non-zero λ_{ijk}, λ'_{ijk}, λ''_{ijk} for the chargino and neutralino pairs. Here i, j, k are generation indices, J = quark jet, L = lepton and $\not{E}$ = missing energy from neutrinos. Each fermion subset indicated by ‡ is the result of the decay of a single $\tilde{\chi}_1^\pm$ or $\tilde{\chi}_1^0$ as illustrated in Fig. 6.2. The combination of these subsets give rise to the various final state topologies shown.

and light selectrons with high production cross section for neutralino pairs. The production cross sections of gauginos do not depend on the size of the R-parity violating Yukawa coupling, since the pair-production of sparticles only involves gauge couplings.

The chargino and the three heaviest neutralinos can decay either directly or indirectly, while the lightest neutralino can only decay directly. In Fig. 6.2, Feynman diagrams illustrating the mechanism for direct decay are shown. Direct decays involve the decay of the gauginos into sfermions which in turn decay via R-parity violating couplings to fermions. In indirect decays, the gaugino decays first into the lightest neutralino and two fermions via a W^* or a $(Z/\gamma)^*$ exchange for the chargino and neutralino respectively. This is illustrated by the Feynman diagrams in Figs. 6.3a and 6.3b respectively. In Tables 6.1 and 6.2, the final state topologies

Indirect Decay Mode	Sparticle	
	$\tilde{\chi}_1^+ \; \tilde{\chi}_1^-$ $\tilde{\chi}_1^+ \to W^* \tilde{\chi}_1^0 \to f\bar{f}^* \tilde{\chi}_1^0$	$\tilde{\chi}_1^0 \; \tilde{\chi}_2^0, \; \tilde{\chi}_2^0 \; \tilde{\chi}_2^0$ $\tilde{\chi}_2^0 \to \tilde{\chi}_1^0 f\bar{f}$
	$f\bar{f} \to \underbrace{l^+l^-}, \; \nu\bar{\nu}, \; \underbrace{q\bar{q}}$ $4L, \not{E}, 4J, 2L+\not{E}, 2L+2J, 2J+\not{E}$	
λ_{ijk}	$4L+\not{E} \oplus f\bar{f} \left\{ \begin{array}{c} 8L+\not{E}, \\ 4L+\not{E}, \\ 4L+4J+\not{E}, \\ 6L+\not{E}, \\ 6L+2J+\not{E}, \\ 4L+2J+\not{E}. \end{array} \right.$	$4L+\not{E} \oplus f\bar{f} \left\{ \begin{array}{c} 8L+\not{E}, \\ 4L+\not{E}, \\ 4L+4J+\not{E}, \\ 6L+\not{E}, \\ 6L+2J+\not{E}, \\ 4L+2J+\not{E}. \end{array} \right.$
λ'_{ijk}	$4J+L+\not{E} \oplus f\bar{f} \left\{ \begin{array}{c} 4J+5L+\not{E}, \\ 4J+L+\not{E}, \\ 8J+L+\not{E}, \\ 6J+2L+\not{E}, \\ 6J+L+\not{E}. \end{array} \right.$	$4J+L+\not{E} \oplus f\bar{f} \left\{ \begin{array}{c} 4J+5L+\not{E}, \\ 4J+L+\not{E}, \\ 8J+L+\not{E}, \\ 6J+2L+\not{E}, \\ 6J+L+\not{E}. \end{array} \right.$
	$4J+2L \oplus f\bar{f} \left\{ \begin{array}{c} 4J+6L, \\ 4J+2L+\not{E}, \\ 8J+2L, \\ 4J+4L+\not{E}, \\ 6J+4L, \\ 4J+2L+\not{E}. \end{array} \right.$	$4J+2L \oplus f\bar{f} \left\{ \begin{array}{c} 4J+6L, \\ 4J+2L+\not{E}, \\ 8J+2L, \\ 4J+4L+\not{E}, \\ 6J+4L, \\ 4J+2L+\not{E}. \end{array} \right.$
	$4J+\not{E} \oplus f\bar{f} \left\{ \begin{array}{c} 4J+4L+\not{E}, \\ 4J+\not{E}, \\ 8J+\not{E}, \\ 4J+2L+\not{E}, \\ 6J+2L+\not{E}, \\ 4J+\not{E}. \end{array} \right.$	$4J+\not{E} \oplus f\bar{f} \left\{ \begin{array}{c} 4J+4L+\not{E}, \\ 4J+\not{E}, \\ 8J+\not{E}, \\ 4J+2L+\not{E}, \\ 6J+2L+\not{E}, \\ 4J+\not{E}. \end{array} \right.$
λ''_{ijk}	$6J \oplus f\bar{f} \left\{ \begin{array}{c} 6J+4L, \\ 6J+\not{E}, \\ 10J, \\ 6J+2L+\not{E}, \\ 8J+2L, \\ 8J+\not{E}. \end{array} \right.$	$6J \oplus f\bar{f} \left\{ \begin{array}{c} 6J+4L, \\ 6J+\not{E}, \\ 10J, \\ 6J+2L+\not{E}, \\ 8J+2L, \\ 8J+\not{E}. \end{array} \right.$

Table 6.2: Indirect R-parity violating decay modes for non-zero λ_{ijk}, λ'_{ijk} and λ''_{ijk} for chargino and neutralino pairs. Here i, j, k are generation indices, J = quark jet, L = lepton and $\not{E}$ = missing energy from neutrinos. The various topologies arising from the combination of final state particles (Fig. 6.3) and a $f\bar{f}$ pair are shown.

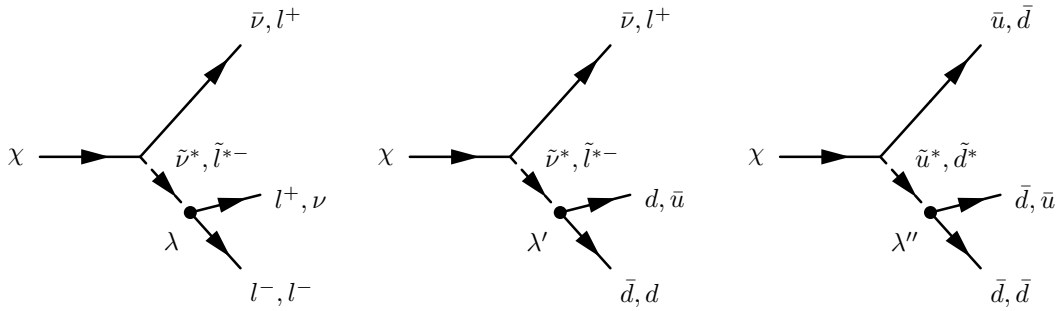

Figure 6.2: Direct R-parity violating decays of the lightest neutralino via the λ, λ' and λ'' couplings. The points mark the R-parity violating vertex in the decay.

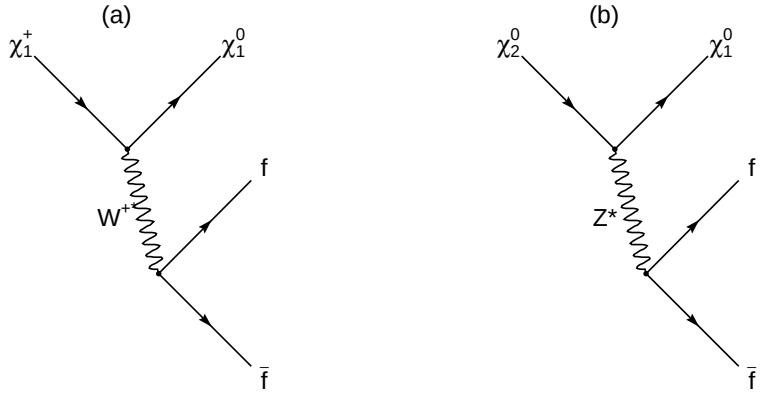

Figure 6.3: Indirect decay of (a) the chargino and (b) the next-lightest neutralino into the lightest neutralino and a $f\bar{f}$ pair. The neutralino subsequently decays directly via an R-parity violating coupling as shown in Fig. 6.2.

resulting from the direct and indirect decay of chargino and neutralino pairs are shown. In Table 6.2, each topology is the result of the combination of the topology resulting from the decay of $\tilde{\chi}_1^0$ as shown in Table 6.1 with topologies arising from the decay of $f\bar{f}$. The similarity of many of the resultant topologies made it difficult to design cuts for single topologies. As a result, searches were carried out by clustering topologies together.

Final state topologies are dependent on the leptonic decay branching ratios. They are also dependent on the *a priori* unknown size of the Yukawa coupling, λ_{ijk}, the masses and couplings of the decaying sparticle and the lighter SUSY states as well as the nature of the LSP [80].

The dependence of final state topologies on the *a priori* unknown size of the Yukawa coupling can lead to the domination of certain topologies over other topological states in channels within a decay mode. This can be understood when one considers for example, a decay mode in which the final state particles x_1 and x_2 decay in the form $x_1 \rightarrow A,\ B$ and $x_2 \rightarrow C,\ D$, resulting in the separate channels A, B, C and D, the final state particles in each channel will combine in the form $(\mathrm{A}+\mathrm{B}+\mathrm{C}+\mathrm{D})(\mathrm{A}+\mathrm{B}+\mathrm{C}+\mathrm{D})$ to produce different topologies. If the final state particles are assumed to have an equal probability of being produced in each channel, then the resulting topology would take the form

$$\mathrm{A}^2+\mathrm{B}^2+\mathrm{C}^2+\mathrm{D}^2+2\mathrm{AB}+2\mathrm{AC}+2\mathrm{AD}+2\mathrm{BC}+2\mathrm{BD}+2\mathrm{CD}. \tag{6.1}$$

Applying this to the topologies in the direct decay of the $\tilde{\chi}_1^0\ \tilde{\chi}_1^0$ via an $LQ\bar{D}$ coupling to produce the topologies $4Jets+2Leptons$, $4Jets+1Lepton+\not{E}$ and $4Jets+\not{E}$, we see from Table 6.1 that:

$$\begin{aligned}
\tilde{\chi}_1^0\ \tilde{\chi}_1^0 \rightarrow\ & \mathrm{A}: l_i^- u_j \bar{d}_k, \quad llqqqq^{\mathrm{A}}\ llqqqq^{\mathrm{B}}\ \nu lqqqq^{\mathrm{C}}\ l\nu qqqq^{\mathrm{D}} \\
& \mathrm{B}: l_i^+ \bar{u}_j d_k, \quad llqqqq\ \ llqqqq\ \ \nu lqqqq\ \ l\nu qqqq \\
& \mathrm{C}: \nu_i d_j \bar{d}_k, \quad l\nu qqqq\ l\nu qqqq\ \nu\nu qqqq\ \nu\nu qqqq \\
& \mathrm{D}: \bar{\nu}_i \bar{d}_j d_k, \quad l\nu qqqq\ l\nu qqqq\ \nu\nu qqqq\ \nu\nu qqqq.
\end{aligned} \tag{6.2}$$

Here A, B, C and D in column one represent the separate channels. In columns three through six, the indices and charge signs have been dropped for simplicity. The charged leptons are denoted by the symbol l and the quarks are denoted by q. In columns 3 through 6, the combination states are obtained by combining each channel with the channel denoted by the superscript. For example the combination state in column-3:row-1 is obtained by combining the channels AA, column-3:row-

2 AB, column-4:row-1 BA, and so forth. The combination $llqqqq$ denotes the $4Jets + 2Leptons$ topology, $l\nu qqqq$ denotes the $4Jets + 1Lepton + \not{E}$ topology and $\nu\nu qqqq$ denotes the $4Jets + \not{E}$ topology. With the assumption that each column has a 25% probability of being formed, we would obtain final state topologies with branching ratios of:

$$\begin{aligned} 4\text{Jets} + 2\text{Leptons} &\rightarrow 25\% \\ 4\text{Jets} + 1\text{Lepton} + \not{E} &\rightarrow 50\% \\ 4\text{Jets} + \not{E} &\rightarrow 25\%. \end{aligned}$$

In this analysis, this is seen not to be true. The $4Jets + \not{E}$ topology is completely dominant over the other two topologies with branching ratios in excess of 90%. This observation is only relevant to direct decays of certain couplings involving multiple topologies, i.e. neutralino/chargino decays via the $LQ\bar{D}$ couplings and chargino decays via the $LL\bar{E}$ couplings. For indirect decays it is not relevant because the selections used were designed to be flexible over the various topologies.

In order to be as model independent as possible, direct decays of the lightest chargino pair ($\tilde{\chi}_1^+ \ \tilde{\chi}_1^-$), the lightest neutralino pair ($\tilde{\chi}_1^0 \ \tilde{\chi}_1^0$) and the lightest and next-lightest neutralino pair ($\tilde{\chi}_1^0 \ \tilde{\chi}_2^0$) as well as indirect decays of $\tilde{\chi}_1^+ \ \tilde{\chi}_1^-$ and $\tilde{\chi}_1^0 \ \tilde{\chi}_2^0$ are considered. In regions where the production cross section of $\tilde{\chi}_1^0 \ \tilde{\chi}_1^0$ and $\tilde{\chi}_1^0 \ \tilde{\chi}_2^0$ were not sensitive to signal, $\tilde{\chi}_2^0 \ \tilde{\chi}_2^0$ decays were considered.

6.2 Decay selections

In this section the various decay modes for the chargino and neutralino via the $LL\bar{E}$, $LQ\bar{D}$ and $\bar{U}\bar{D}\bar{D}$ couplings are discussed and the selections developed to search for the resulting topologies are described. The selections used to carry out

searches for gaugino decays via the $LL\bar{E}$ were taken from previous searches carried out at lower energies [62]. In the case of decays via $LQ\bar{D}$ couplings, three of the four selections were taken from [81] and optimized. For decays via $\bar{U}\bar{D}\bar{D}$ couplings, three of the four selections used were developed for this analysis and the last was taken from [81] and optimized.

The selections used in this analysis consisted of a collection of cuts on physical variables. The variables are separated into three categories: variables linked to global event properties, to the event separation into hemispheres and to the jet reconstruction.

Global event properties

Some of the physical variables used in this analysis which have global event properties are listed.

- N_{ch} refers to the number of charged tracks. Good tracks are charged particle tracks with at least four hits in the TPC originating from within a cylinder of radius 2cm and length 20cm, coaxial with the beam and centred on the interaction point.

- E_{vis} and M_{vis} denote the visible energy and mass carried by all reconstructed particles.

- P_T and P_Z denote the transverse and longitudinal momentum carried by all reconstructed particles.

- θ_{miss} and ϕ_{miss} denote the polar and azimuthal angles of the missing momentum. These variables are used to reject events with energy lost along the beam axis or in insensitive areas of the detector such as the separation regions between modules.

- E_{12} denotes the total energy detected in the luminosity calorimeters within 12° of the beam axis. It is useful in reducing low energy events such as $\gamma\gamma$ events.

- E_W^{30} denotes the amount of energy detected in a 30° wedge around the missing momentum vector, in a plane transverse to the beam axis. It is a measurement of the isolation of the missing momentum. Although there are neutrinos in τ decays or heavy quark semi-leptonic decays, they are not in general isolated in this respect. Only the transverse plane is considered since there might be energy lost along the beam direction, for example, photons from radiative returns to the Z resonance. Radiative returns to the Z resonance are due to Initial State Radiation (ISR), occurring at energies above the Z resonance and resulting in the production of events which contribute to the interaction cross section at the Z peak. In Fig. 6.4, the mechanism of ISR, which occurs when the incident e^+ (e^-) emits a photon, is illustrated. The probability for the emission of the photon by the incident e^+ (e^-) is inversely proportional to the energy of the photon. The remaining e^+e^- system interacts with a cross section corresponding to an effective interaction energy determined from the difference between the beam energy and the energy of the emitted photon. In radiative returns to the Z, the effective energy is brought close to the Z resonance. The histogram in Fig. 6.4b illustrates the effects from radiative returns to the Z resonance. This is seen clearly by the peak at $\approx 0.45(M_{vis}/\sqrt{s})$.

Hemisphere properties

The thrust, T, is a measure of the collinearity of the particles around a thrust axis

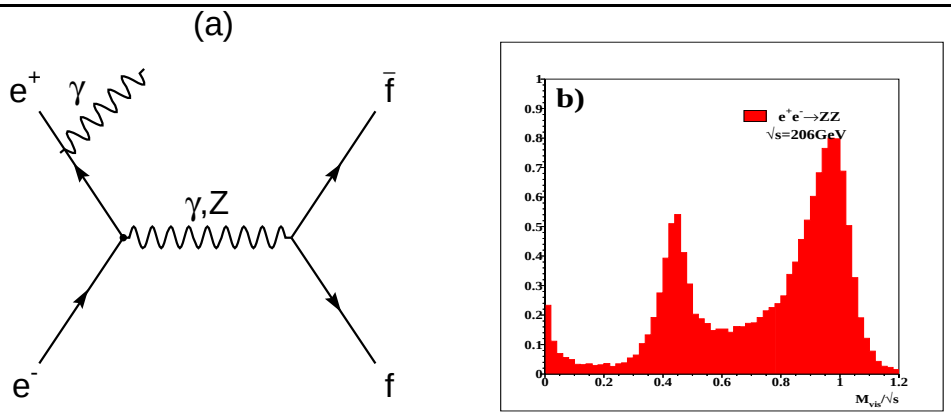

Figure 6.4: (a) Feynman diagram illustrating the mechanism of ISR for e^+e^- collisions. (b) Histogram plot of the visible mass M_{vis}, in terms of the centre-of-mass energy, $\sqrt{s}$, for 50,000 $e^+e^- \rightarrow$ ZZ events. When ISR occurs at energies above the Z resonance, the effective interaction energy, which is the difference between the beam energy and the energy of the emitted photon, is brought close to the Z peak. This is shown by the peak at $\approx 0.45(M_{vis}/\sqrt{s})$.

which is defined by a unit vector, $\mathbf{n}_T$, such that the equation

$$T = \frac{\sum_i |\mathbf{p}_i \cdot \mathbf{n}_T|}{\sum_i \mathbf{p}_i} \tag{6.3}$$

is a maximum. Here T is the thrust and $\mathbf{p}_i$ is a momentum vector of the i^{th} particle and the sums extend over all particles in the event. The thrust axis is used to separate events into two hemispheres. Hemisphere mass, energy and momentum have similar definitions to event mass, energy and momentum, but for particles in the relevant hemisphere. The acollinearity, Φ_{acol} is the space angle between the hemisphere momenta. The acoplanarity, Φ_{acop}, is the angle between the projections of these momenta onto a plane perpendicular to the beam axis. The inverse boost, $InvB$ is a physical variable that is used to measure the mean boost of the hemispheres using the formula, $InvB = (\sqrt{\frac{1}{2}(\gamma_1^{-2} + \gamma_2^{-2})})$ where $\gamma_i = E_i/m_i$ and E_i and m_i are the hemisphere mass and energy respectively.

Jet properties

For processes which involve the production of quark jets, a jet finding algorithm is

used to cluster the events into jets. The two standard algorithms used for physics analysis in ALEPH are the JADE [82] and Durham [83] algorithms. The algorithms work on the principle that tracks from the same jet are generally close together and therefore the invariant mass of any two tracks inside a jet should be less than that of any two tracks in different jets. Jets are built by running a loop over all pairs of tracks to find a pair with the smallest invariant mass M_{inv}. If

$$\left(\frac{M_{inv}}{E_{vis}}\right)^2 < y_{cut} \ , \tag{6.4}$$

where E_{vis} is the visible energy of the event, and y_{cut} is an arbitrary parameter, it merges the two tracks together by adding their momenta. The loop is rerun over the new list of tracks which have lost 2 particles but gained a merged pair. This is repeated until no pairs of tracks with a low enough mass to satisfy Eq. 6.4 are left. The smallest value of y_{cut} at which the number of jets found in any given event is i, is called y_i [84]. For example, y_2 (when $i = 2$) denotes an event with a two-jet topology. Similarly, y_3, y_4, y_5 and y_6 denote events with three-jet, four-jet, five-jet and six-jet topologies respectively. The difference between the JADE and Durham algorithms is due to a difference in the definition of M_{inv}. In the JADE algorithm, this is defined as

$$M_{inv}^2 = 2E_1E_2(1 - \cos\theta_{12}), \tag{6.5}$$

where E_1 and E_2 are the energies of the tracks and θ_{12} is the angle between them. The Durham algorithm defines M_{inv} as

$$M_{inv}^2 = 2(min(E_1, E_2))^2(1 - \cos\theta_{12}), \tag{6.6}$$

The definition of M_{inv} in Eq. (6.6) is slightly different from Eq. (6.5) and reduces the sensitivity to soft gluon radiation. In this analysis both algorithms were used

as they both gave equivalent results.

6.3 Decays via a dominant $LL\bar{E}$ coupling

The direct decay of pair produced $\tilde{\chi}_1^0\ \tilde{\chi}_1^0$ and $\tilde{\chi}_1^0\ \tilde{\chi}_2^0$ gives rise to a $4L + \not{E}$ topology, while $\tilde{\chi}_1^+\ \tilde{\chi}_1^-$ production gives a mixed topology of $2L + \not{E}$, $4L + \not{E}$ and $6L$ (Table 6.1). Indirect decays of $\tilde{\chi}_1^+\ \tilde{\chi}_1^-$ and $\tilde{\chi}_1^0\ \tilde{\chi}_2^0$ give rise to the topologies shown in Table 6.2. The topologies are produced with a branching ratio that is dependent on the region of parameter space in which the events are produced. This excludes events from the direct decay of $\tilde{\chi}_1^0\ \tilde{\chi}_1^0$ and $\tilde{\chi}_1^0\ \tilde{\chi}_2^0$ since the only possible topology is $4L + \not{E}$. For events decaying via a direct mode, searches were carried out for $4L + \not{E}$ only. For events decaying via an indirect mode, searches were carried out for $6L + \not{E}$ ($\tilde{\chi}_1^0\ \tilde{\chi}_2^0$) and an inclusive combination of $6L + \not{E}$ and $Lepton + Hadron$ selections ($\tilde{\chi}_1^+\ \tilde{\chi}_1^-$). The selections implemented for these decays are listed in Table 6.3 and are taken from previous searches at lower energies [62]. It was not necessary to optimize any of the cuts.

6.3.1 Four leptons plus missing energy ($4\mathbf{L} + \not{\mathbf{E}}$)

This topology was selected by requiring that events should have four, five or six good tracks, with at least one being identified as an electron or muon. It required a total visible mass of at least $16\,\mathrm{GeV}/c^2$ and a missing transverse momentum of greater than $5\,\mathrm{GeV}/c^2$. The total neutral hadronic energy in the event was required be less than the total leptonic energy. The background from $q\bar{q}$ and $\tau^+\tau^-$ was reduced by demanding y_4 to be greater than 6×10^{-4}. Also events were clustered into jets using the JADE algorithm and a y_{cut} of m_τ^2/s to form tau-like jets where m_τ^2 was the reconstructed mass squared of the tau and s was the centre-of-mass energy squared. It was required that at least four of these tau-like jets must contain good

<table>
<tr><th colspan="3">$\mathbf{LL\bar{E}}$</th></tr>
<tr><td colspan="3">$\mathbf{4L + \not{E}}$</td></tr>
<tr><td colspan="3">$3 < N_{ch} < 7$, $M_{vis} > 16\,\mathrm{GeV}/c^2$, $P_{\perp}^{miss} > 5\,\mathrm{GeV}/c$
$E_{had} < E_{lep}$, $y_4 > 0.0006$</td></tr>
<tr><td colspan="3">$\mathbf{6L + \not{E}}$</td></tr>
<tr><td colspan="3">$4 < N_{ch} < 12$, $25\%\sqrt{s} < M_{vis} < 85\%\sqrt{s}$, $N_{lep} > 1$
$E_{had} < 6\%\sqrt{s}$, $E_{ch} > 6E_{had}$, $y_4 > 0.004$, $P_{\perp}^{miss} > 2\%\sqrt{s}$</td></tr>
<tr><td colspan="3">$\mathbf{Leptons + Hadrons}$</td></tr>
<tr><td>subselection I</td><td>subselection II</td><td>subselection III</td></tr>
<tr><td>$N_{ch} \geq 5$
$M_{vis} < 25\,\mathrm{GeV}/c^2$</td><td>$15 \geq N_{ch} \geq 5$
$20\,\mathrm{GeV}/c^2 < M_{vis} < 75\%\sqrt{s}$</td><td>$N_{ch} \geq 11$
$55\%\sqrt{s} < M_{vis} < 80\%\sqrt{s}$</td></tr>
<tr><td>$P_{\perp}^{miss} > 3.5\%\sqrt{s}$
$\lvert P_z^{miss}\rvert < 27\,\mathrm{GeV}/c$</td><td>$P_{\perp}^{miss} > 2.5\%\sqrt{s}$</td><td>$P_{\perp}^{miss} > 5\%\sqrt{s}$
$N_{ch}^{jet} \geq 1$</td></tr>
<tr><td>$y_5 > 0.006$</td><td>$y_3 > 0.009$
$y_4 > 0.0026$</td><td>$y_3 > 0.025$
$y_4 > 0.012$
$y_5 > 0.004$
$T < 0.85$</td></tr>
<tr><td>$N_{lep} \geq 1$
$E_{nlep} < 50\%\sqrt{s}$
$E_{had} < 28\%E_{vis}$</td><td>$N_{lep} \geq 1$
$E_{nlep} < 50\%\sqrt{s}$
$E_{had} < 22\%E_{lep}$</td><td>$N_{lep} \geq 1$

$E_{lep} > 20\%E_{had}$</td></tr>
<tr><td colspan="3">$\chi_{WW} > 3.8$ or $N_{lep} > 2.5$</td></tr>
</table>

Table 6.3: Selections for direct and indirect decays via a dominant R-parity violating $LL\bar{E}$ coupling.

tracks. The remaining background was composed of mainly four-fermion events and is shown in Table 6.6.

6.3.2 Six leptons plus missing energy ($\mathbf{6L + \not{E}}$)

This topology was selected by requiring at least 5 but not more than 11 good tracks. At least two of the charged tracks were required to be identified as leptons. This cut was effective in rejecting WW background events as shown in Fig. 6.5a. The visible mass was required to be at least $0.25\sqrt{s}$. It was also required that the neutral hadronic energy be less than $6\%\sqrt{s}$ and 17% of the total energy of all good tracks. To take into account the fact that missing energy is expected in the signal,

it was required that the visible mass be not more than $85\%\sqrt{s}$ and that the missing transverse momentum must be at least $2\%\sqrt{s}$. Finally to reduce the $q\bar{q}$ and $\tau^+\tau^-$ background, y_4 was required to be greater than 0.004. The remaining background was composed mainly of $q\bar{q}$ and four-fermion events as shown in Table 6.6.

6.3.3 Leptons+Hadrons

The $Leptons + Hadrons$ selection was designed for the various possible topologies arising from the indirect decay of gauginos (Table 6.2). Depending on the gaugino mass and the lepton flavour composition in the decay, the indirect decays populate different regions in track multiplicity, visible mass and leptonic energy. For this reason, three different sub-selections were used [63], covering topologies with large leptonic energies and at least two jets (Subselection I), topologies with small multiplicities and large leptonic energy fractions (Subselection II) and topologies with a moderate leptonic energy fraction (Subselection III). All three subselections (Table 6.3) were based on a central requirement of large leptonic energy, supplemented with cuts on the amount of neutral hadronic energy E_{had} and non-leptonic energy E_{nlep}. The presence of at least two neutrinos means that signal events will contain some missing energy. This was taken into account by imposing cuts on the transverse momentum $P_{\perp}^{miss}$. Background from hadronic events with energetic initial state radiation (ISR) photons which escape at small polar angles, was reduced by rejecting events with large missing momentum P_Z^{miss} along the beam axis. ISR photons which made their way into the detector were rejected by requiring that the charged multiplicity N_{ch}^{jet} in all jets found with $y_{cut} = 0.0005$ must be at least 1. In order to reduce most of the remaining background, the variables y_3, y_4, y_5 and event thrust T were used to select spherical events. The WW background was

greatly suppressed by defining

$$\chi^2_{WW} = \left(\frac{m_{qq} - m_W}{10\,\mathrm{GeV}/c^2}\right)^2 + \left(\frac{m_{l\nu} - m_W}{10\,\mathrm{GeV}/c^2}\right)^2 + \left(\frac{p_l + (\sqrt{s} - E_{vis} - 94.0\,\mathrm{GeV})}{10\,\mathrm{GeV}}\right)^2 \quad (6.7)$$

Here m_{qq} is the hadronic mass, $m_{l\nu}$ is the mass of the leading lepton and the missing momentum and p_l is the momentum of the leading lepton. χ_{WW} is required to be at least 3.8. This is illustrated in Fig. 6.5b.

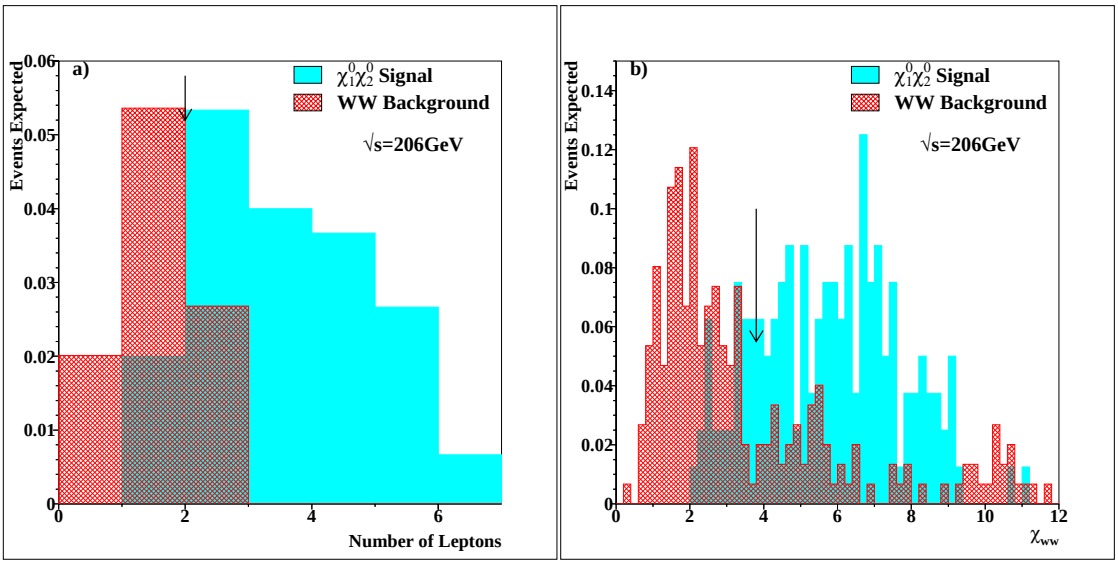

Figure 6.5: The $\tilde{\chi}_1^0\ \tilde{\chi}_2^0$ signal for events decaying indirectly via the $LL\bar{E}$ coupling compared to the WW background after all other cuts have been applied, in terms of the variables: (a) The Number of identified leptons. (b) The χ distribution. The arrows indicate the position of the cuts. The WW background has been normalised to the luminosity of the data.

6.3.4 Summary

The selections listed above were used to carry out searches for $\tilde{\chi}_1^0\ \tilde{\chi}_1^0$, $\tilde{\chi}_1^0\ \tilde{\chi}_2^0$ and $\tilde{\chi}_1^+\ \tilde{\chi}_1^-$ events decaying via the $LL\bar{E}$ coupling. The selections were taken from previous searches carried out at centre-of-mass energies of $130\,\mathrm{GeV}/c^2$ to $172\,\mathrm{GeV}/c^2$ and over a parameter region of all μ and M_2 and $\tan\beta = \sqrt{2}$ and $m_0 = 500\,\mathrm{GeV}/c^2$. In this analysis the selections were used to extend the searches at centre-of-mass

energies from 189 GeV/c^2 to 208 GeV/c^2 and over all μ, $\tan\beta$, m_0 and M_2 as described in section 5.1. No optimizations were carried out on the selections. $\tilde{\chi}_1^0\ \tilde{\chi}_1^0$ searches were carried out using the $4L + \not{E}$ selection. $\tilde{\chi}_1^0\ \tilde{\chi}_2^0$ searches were carried out using the $4L + \not{E}$ and $6L + \not{E}$ selections. $\tilde{\chi}_1^+\ \tilde{\chi}_1^-$ searches were carried out using the $4L + \not{E}$ and an inclusive combination of $6L + \not{E}$ and $Leptons + Hadrons$ selections. The results of the searches are presented in chapter 7.

6.4 Decays via a dominant $LQ\bar{D}$ coupling

For a dominant $LQ\bar{D}$ operator, the event topologies are mainly characterized by large hadronic activity, possibly with some leptons and/or missing energy. The direct decay of $\tilde{\chi}_1^+\ \tilde{\chi}_1^-$, $\tilde{\chi}_1^0\ \tilde{\chi}_1^0$, $\tilde{\chi}_1^0\ \tilde{\chi}_2^0$ and $\tilde{\chi}_2^0\ \tilde{\chi}_2^0$ give rise to a mix of $4J+\not{E}$, $4J+2L$ and $4J+1L+\not{E}$ topologies (Table 6.1). Indirect decays of $\tilde{\chi}_1^+\ \tilde{\chi}_1^-$, $\tilde{\chi}_1^0\ \tilde{\chi}_1^0$, $\tilde{\chi}_1^0\ \tilde{\chi}_2^0$ and $\tilde{\chi}_1^0\ \tilde{\chi}_2^0$ lead to multi-jet, multi-lepton and/or multi-neutrino states (Table 6.2). For events that decay directly, searches were carried out for $4J+\not{E}$ and $4J+2\tau$. *Multijet+Lepton* and *Broadjet+Lepton* selections were used to search for indirect decays. All selections used are listed in Table 6.4. All the selections except the $4J+\not{E}$ selections were taken from previous searches at centre-of-mass energies $130\,\mathrm{GeV}/c^2$ to $172\,\mathrm{GeV}/c^2$ [81] and optimized.

6.4.1 Four jets plus missing energy ($4\mathrm{J}+\not{\mathrm{E}}$)

This topology has a distinct missing energy signature resulting from the production of two neutrinos. After a preselection of at least eight charged tracks, a minimum jet energy of $24\%\sqrt{s}$ and a visible energy of not greater than $80\%\sqrt{s}$, it was required that the missing transverse momentum must be greater than $10\,\mathrm{GeV}/c$. This rejects a large proportion of the $q\bar{q}$ background (Fig. 6.6a). The energy in a 30° azimuthal wedge around the direction of the missing momentum was required to be not greater than $25\%\sqrt{s}$. To reduce $q\bar{q}$ and four-fermion backgrounds, a cut of at least 0.9 was implemented on the thrust, T (Fig. 6.6b). Since the topology only involves the production of quarks and neutrinos, a cut vetoing the presence of identified leptons was implemented. This also reduced the WW background as illustrated in Fig. 6.6c. Depending on the mass of the neutralino, the boost on the final state quarks could be high, in which case instead of a distinct four-jet topology with missing energy, the event could have a broad two-jet topology with missing energy. To take

LQD̄	
4J + $\not{E}$	**4J + 2τ**
$N_{ch} > 8$	
$E_{vis} < 80\%\sqrt{s}$, $P_T > 10\,\mathrm{GeV}/c$ $E_W^{30} < 25\%\sqrt{s}$, $\Theta_{Thrust} < 0.97$ $T > 0.9$ $Min(E_{j1}, E_{j2}) > 12\%\sqrt{s}$	$E_{ch} > 29\%\sqrt{s}$, $E_{vis} < 95\%\sqrt{s}$ $\lvert P_Z\rvert < 64\,\mathrm{GeV}/c$, $E_1^1 < 33\,\mathrm{GeV}$ $\cos\theta_{miss} < 0.96$ ≥ 1 lepton identified with $\phi_1 > 15.9°$ $M_W > 90\,\mathrm{GeV}/c^2$, $\Phi_{aco} < 175°$
$y_2 > 0.002$ $y_4 > 0.0001$	$y_4 > 0.0029$ $y_5 > 0.0005$
$N_{lep} < 1$, $E_{jet}^{em} < E_{jet}$	$23\,\mathrm{GeV} < E_{miss} + E_{lep}$
Broadjets + Leptons	**Multijets + Leptons**
$N_{ch} \geq 10$	
$E_{vis} > 50\%\sqrt{s}$ $E_{10}^{iso} < 2\,\mathrm{GeV}$	$E_{vis} > 45\,\mathrm{GeV}$ $E_{10}^{iso} < 5\,\mathrm{GeV}$
$E_{vhad} > 50\%\sqrt{s}$, $\Theta_{miss} > 30°$ $E_T > 80\,\mathrm{GeV}$, $T < 0.9$	
$y_2 > 0.03$ $y_4 > 0.01$	$y_5 > 0.003$ $y_6 > 0.0015$
$E_{jet}^{em} < 100\%E_{jet}$ $\Phi'_{acop} + (E_{vhad} - 120) \times 0.55 < 180$	

Table 6.4: Selections for direct and indirect decays via a dominant R-parity violating $LQ\bar{D}$ coupling.

this into consideration, it was required that $y_2 > 0.002$ and $y_4 > 0.0001$. These cuts were not very tight due to the fact that at low $m_{\tilde{\chi}_1^0}$, the boost on the quark jets results in a topology very similar to the $q\bar{q}$ background. This is illustrated in Fig. 6.7. To remove far-forward events that may arise from low energy processes, it was required that all events found around the thrust axis within 14° of the beam axis be rejected. To reduce background from ISR photons seen in the detector, the electromagnetic energy, E_{jet}^{em}, in any jet was required to be less than the jet energy, E_{jet}. The remaining background is composed mainly of $q\bar{q}$ and WW events

as shown in Table 6.6.

6.4.2 Four jets plus two taus ($4J + 2\tau$)

This selection was taken from [81] and optimized. After a preselection of at least eight charged tracks, a minimum total track energy of $29\%\sqrt{s}$ and a visible energy of not more than $95\%\sqrt{s}$, the taus were tagged through their decays by demanding that there be at least one well isolated identified lepton which must exist in an azimuthal cone at least 15.9° from the nearest charged track. This was also useful in rejecting the $q\bar{q}$ background as illustrated in Fig. 6.8a. The leading lepton was required to have an energy of at not more than 33 GeV/c^2. In order to reject events from WW background, the invariant hadronic mass was required to be at least 90 GeV/c^2 (Fig. 6.8b). Background from hadronic WW decays was further reduced by rejecting events for which $(E_{miss} + E_{lep})$ is large, where E_{miss} is the total missing energy and E_{lep} is the LEP energy. To ensure that the missing momentum vector, did not point along the beam axis, events with a missing momentum vector within a 16° cone around the beam axis were rejected. The acoplanarity angle between the quark jets was required to be no more than 175°. The jet finding variables, y_4 and y_5 were required to be greater than 0.0029 and 0.0005 respectively. This was effective in rejecting $q\bar{q}$ events as illustrated in Fig. 6.8c. The remaining background is composed of mainly $q\bar{q}$, WW and ZZ events and is shown in Table 6.6.

6.4.3 Broadjets plus leptons

This selection was taken from [81] and optimized for events in which the lightest neutralino has a mass of less than 70 GeV/c^2. Such events result in topologies with broad jets rather than distinct jets. After a preselection of at least ten charged tracks and a visible energy of at least $50\%\sqrt{s}$, the visible hadronic energy was required to be at least $50\%\sqrt{s}$. This is effective in rejecting four fermion Zee events as

illustrated in Fig.6.9a. Events from $q\bar{q}$ background are rejected by requiring that the polar angle of the missing momentum vector must be greater than 30° (Fig. 6.9b). It is further reduced by selecting spherical events using the event thrust, T, and also by requiring that y_2 and y_4 be greater than 0.03 and 0.01 respectively (Figs. 6.9c and 6.9d). The transverse energy, E_T, was required to be high. The isolation of the missing momentum vector was ensured by removing events with large deposits of energy, E_{10}^{iso}, within a 10° degree cone. To reduce background from hadronic events with ISR photons seen in the detector, it was required that the electromagnetic energy in any jet be less than 90% of the jet energy. In order to further reduce the hadronic background, a cut $\Omega = \Phi'_{acop} + (E_{vhad} - 120) \times 0.55$ was applied to the (E_{vhad}, Φ'_{acop}) plane, where E_{vhad} is the visible hadronic energy and Φ'_{acop} is the acoplanarity angle of the hadronic system (Fig. 6.10a). The remaining background was composed mainly of WW events as illustrated in Table 6.6.

6.4.4 Multijets plus leptons

This selection was taken from [81] and optimized. It was designed for events with distinct rather than broad jets. The requirements are similar to those implemented for the *Broadjet+lepton* selection with the exception that the visible energy should be at least 45 GeV and that y_5 and y_6 should be greater than 0.003 and 0.0015 respectively (Figs. 6.10b and 6.10c).

6.4.5 Summary

The selections discussed above were used to carry out searches for $\tilde{\chi}_1^0\ \tilde{\chi}_1^0$, $\tilde{\chi}_1^0\ \tilde{\chi}_2^0$ and $\tilde{\chi}_1^+\ \tilde{\chi}_1^-$ events decaying via the $LQ\bar{D}$ coupling. All selections except the $4J + \not{E}$ selection were taken from previous searches carried out at centre-of-mass energies of 130 GeV to 172 GeV and optimized. Previous searches were carried out to cover only the regions $m_0 = 500\,\mathrm{GeV}/c^2$ and $\tan\beta = \sqrt{2}$ for all μ and M_2. In this

analysis, the searches were extended to cover μ, $\tan\beta$, m_0 and M_2 as explained in section 5.1 at centre-of-mass energies 189 GeV to 208 GeV. $\tilde{\chi}_1^0\ \tilde{\chi}_1^0$ searches were carried out using the $4J + \not{E}$ selection. $\tilde{\chi}_1^0\ \tilde{\chi}_2^0$ searches were carried out using the $4J + 2\tau$ and *Broadjet + Lepton* selections, and $\tilde{\chi}_1^+\ \tilde{\chi}_1^-$ searches were carried out using the $4J + 2\tau$ and *Multijet + Lepton* selections. The results of the searches are presented in chapter 7.

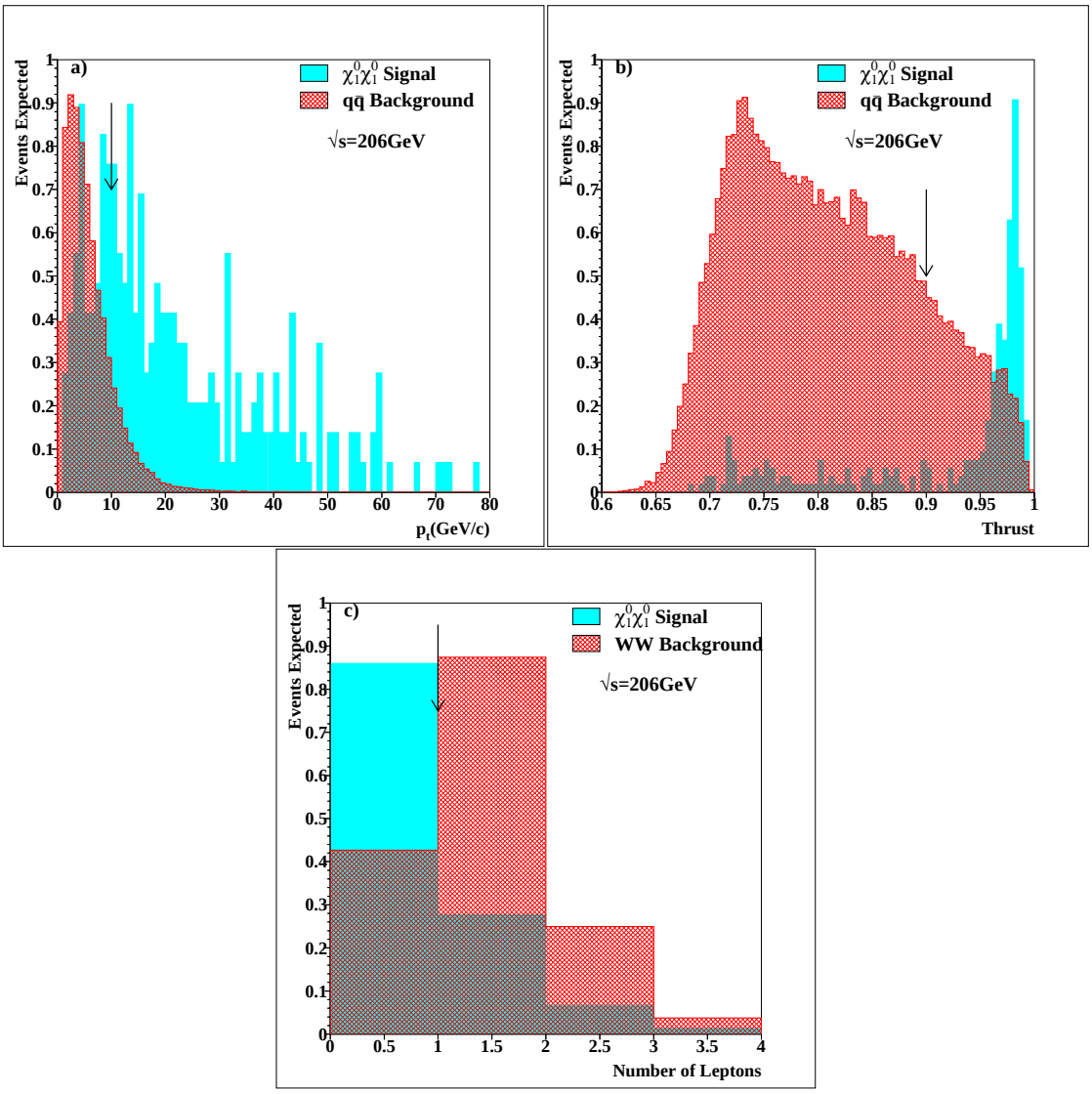

Figure 6.6: The $\tilde{\chi}_1^0$ $\tilde{\chi}_1^0$ signal for direct decays via the $LQ\bar{D}$ coupling compared to the $q\bar{q}$ and WW backgrounds after a preselection on the number of charged tracks, the visible energy and the total jet energy, in terms of the following variables: (a) Transverse momentum. (b) Thrust. (c) The number of identified leptons. The arrows indicate the position of the cuts. All backgrounds have been normalised to the luminosity of the data. The vertical axis normalization is arbitrary.

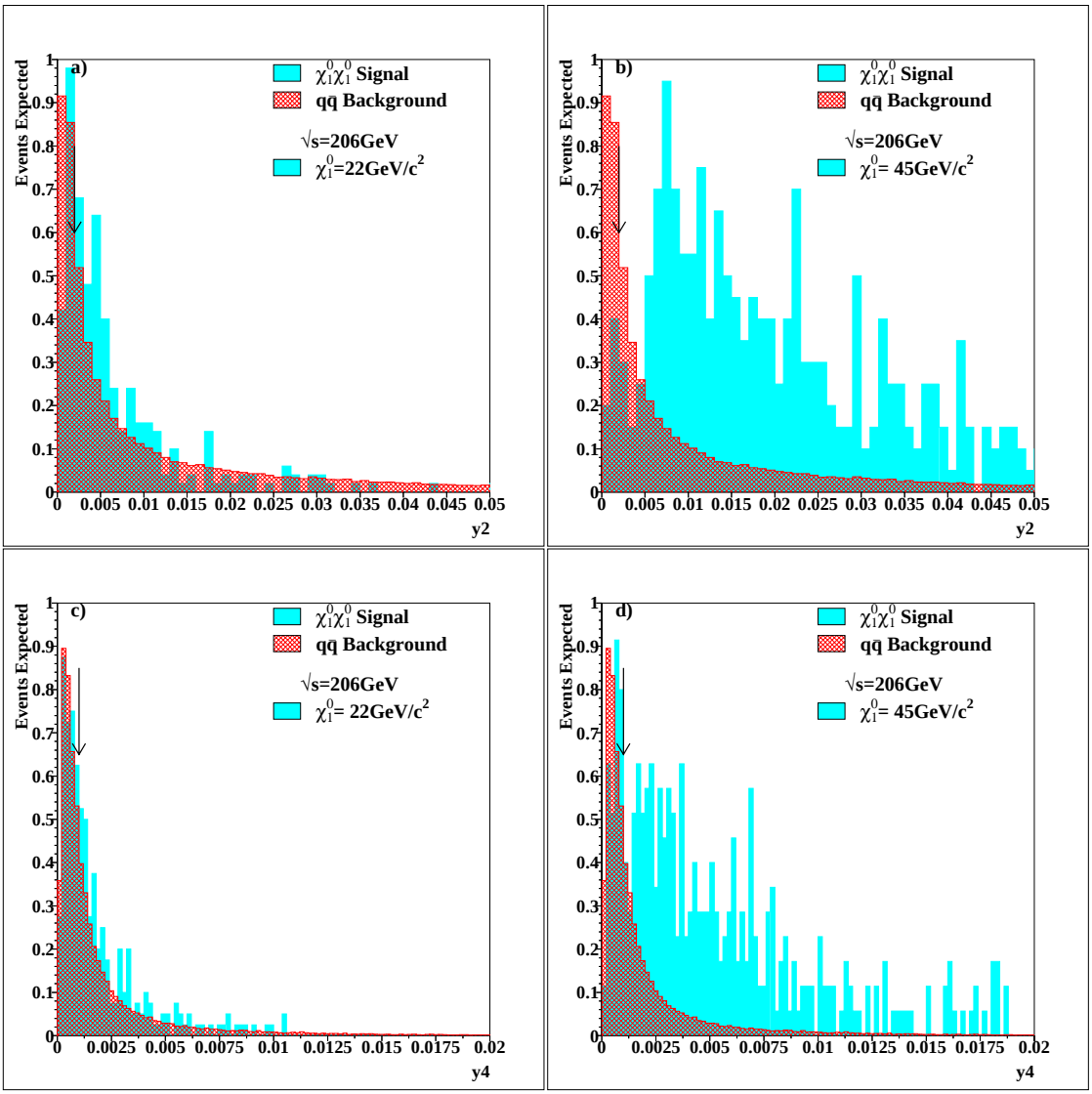

Figure 6.7: The $\tilde{\chi}_1^0$ $\tilde{\chi}_1^0$ signal for events at two different points in parameter space decaying directly via the $LQ\bar{D}$ coupling for which $m_{\tilde{\chi}_1^0} = 22\,\mathrm{GeV}/c^2$ and $45\,\mathrm{GeV}/c^2$, and compared to the $q\bar{q}$ background after a preselection on number of charged tracks, the visible energy and the total jet energy. The signal and backgrounds are compared in terms of y_2 and y_4. In (a) and (c), the low neutralino mass results in the topology acquiring a 2jet-like structure. This makes the signal difficult to extract from the $q\bar{q}$ background. This is not the case in (b) and (d) where the neutralino has a higher mass. In order to have a flexible selection, y_2 and y_4 were made loose, i.e. were required to accept events for which $y_2 > 0.002$ and $y_4 > 0.001$. The arrows indicate the position of the cuts. The $q\bar{q}$ background has been normalised to the luminosity of the data. The vertical axis normalization is arbitrary.

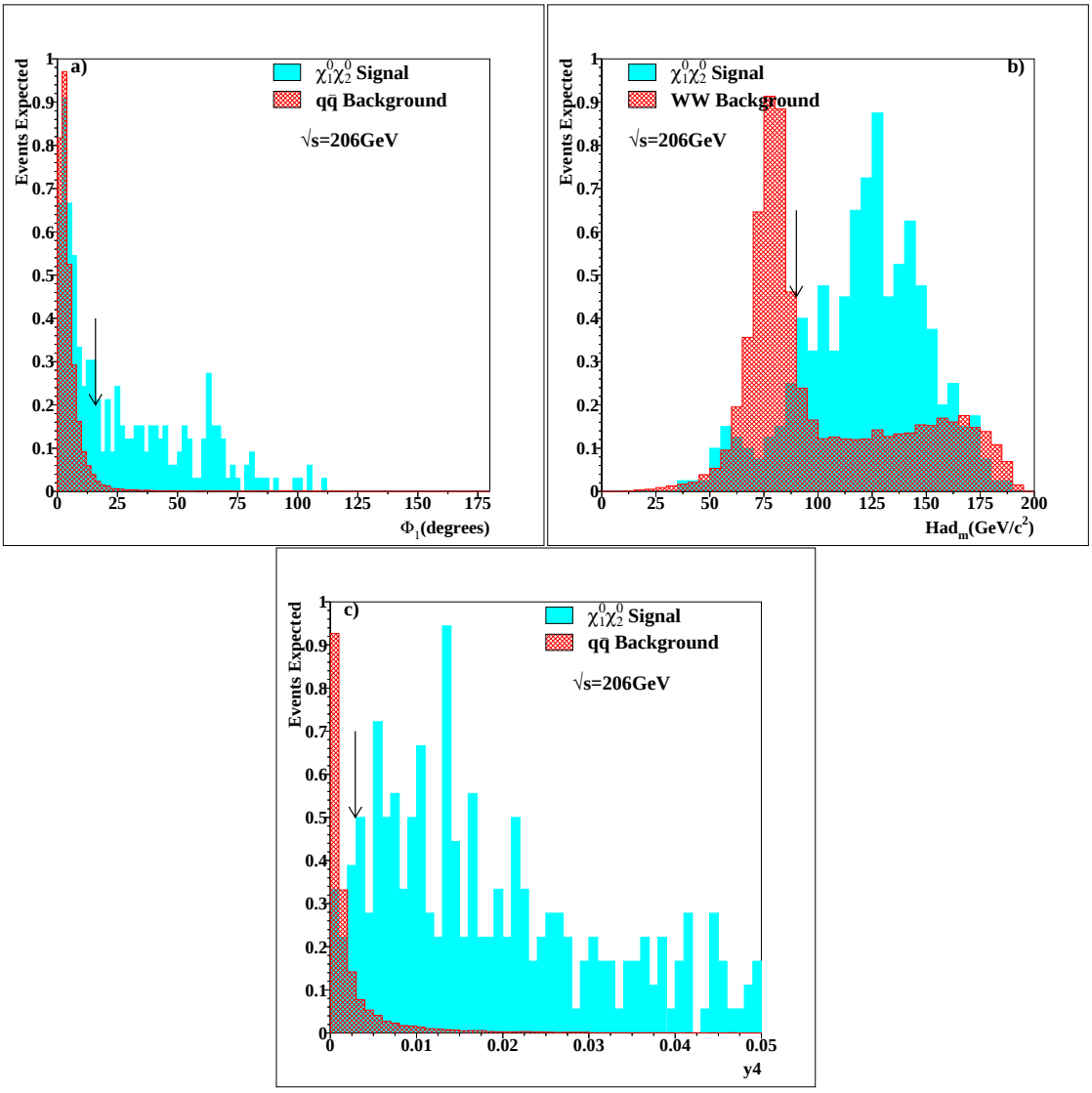

Figure 6.8: The $\tilde{\chi}_1^0\ \tilde{\chi}_1^0$ and $\tilde{\chi}_1^0\ \tilde{\chi}_2^0$ signals for events decaying directly via the $LQ\bar{D}$ coupling compared to the $q\bar{q}$ and WW backgrounds after a preselection on number of charged tracks, the total energy of charged tracks and the visible energy, in terms of the following variables: (a) The Φ angle of the isolated lepton with respect to the nearest charged track.(b) The invariant hadronic mass for the process $W \to \tau\nu qq$. (c) The jet finding variable, y_4. The arrows indicate the position of the cuts. All backgrounds have been normalised to the luminosity of the data. The vertical axis normalization is arbitrary.

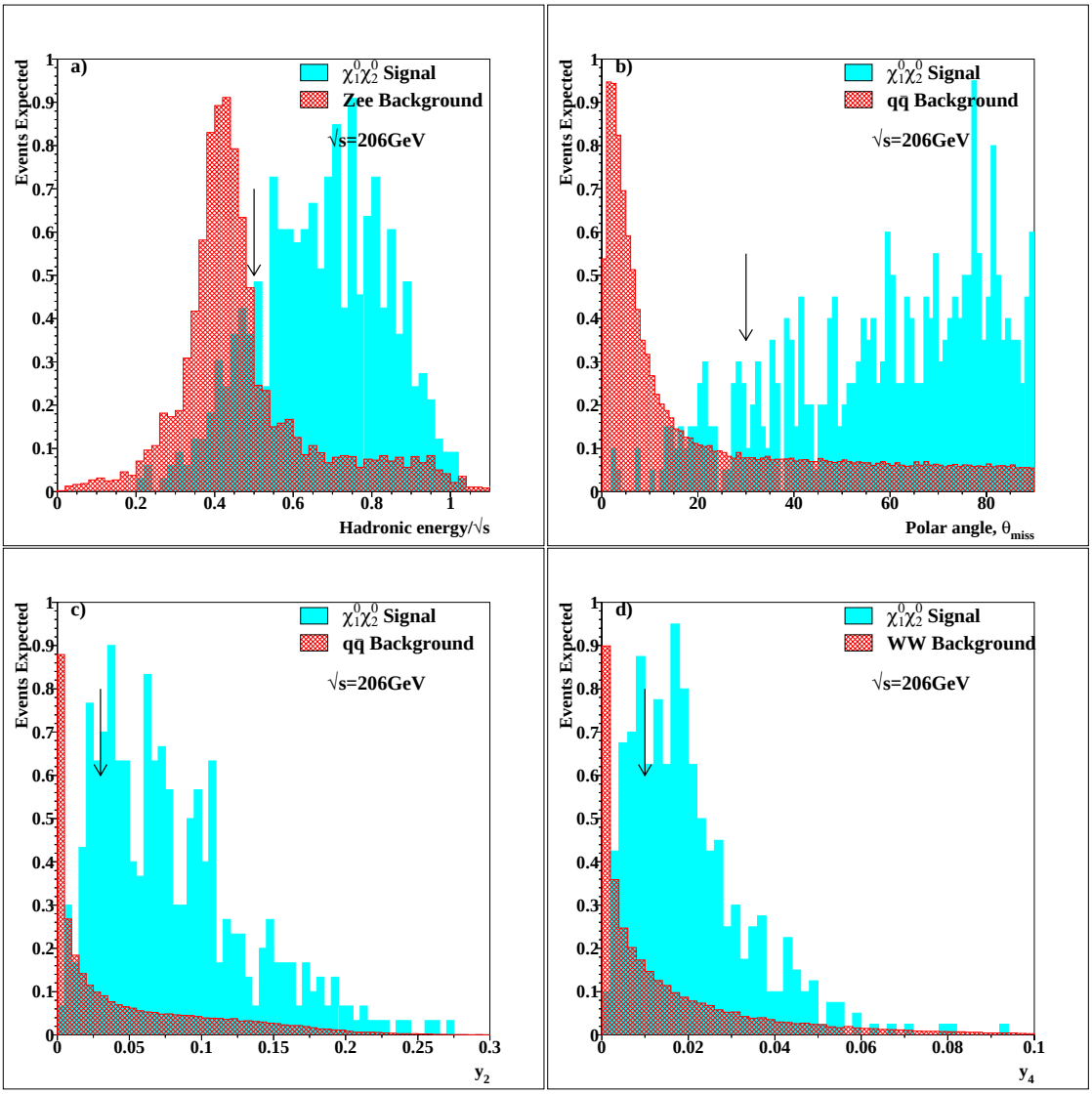

Figure 6.9: The $\tilde{\chi}_1^0$ $\tilde{\chi}_2^0$ signal for events decaying indirectly via the $LQ\bar{D}$ coupling compared to the $q\bar{q}$ and WW backgrounds after a preselection on number of charged tracks and the visible energy, in terms of the following variables: (a) The visible hadronic energy. (b) The polar angle. (c) The jet finding variable, y_2. (d) The jet finding variable, y_4. The arrows indicate the position of the cuts. All backgrounds have been normalised to the luminosity of the data. The vertical axis normalization is arbitrary.

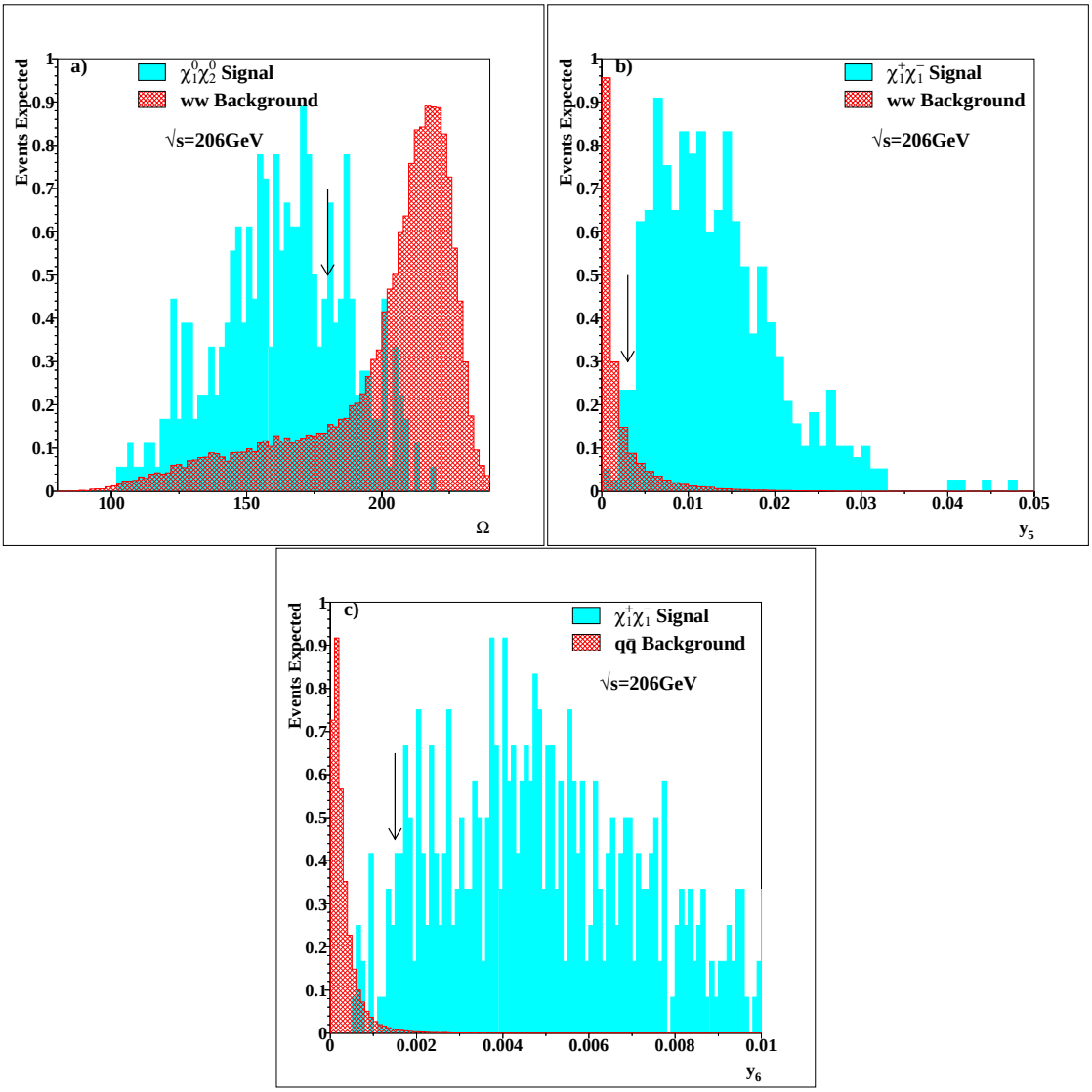

Figure 6.10: The $\tilde{\chi}_1^0$ $\tilde{\chi}_2^0$ and $\tilde{\chi}_1^+$ $\tilde{\chi}_1^-$ signals for events decaying indirectly via the $LQ\bar{D}$ coupling compared to the WW and $q\bar{q}$ backgrounds after a preselection on number of charged tracks and the visible energy, in terms of the following variables: (a) a one dimensional representation, Ω, of the distribution, $\Phi'_{acop} + (E_{vhad} - 120) \times 0.55$. (b) and (c) the jet finding variables y_5 and y_6. The arrows indicate the position of the cuts. All backgrounds have been normalised to the luminosity of the data. The vertical axis normalization is arbitrary.

6.5 Decays via a dominant $\bar{U}\bar{D}\bar{D}$ coupling

For decays via a dominant $\bar{U}\bar{D}\bar{D}$ operator, the final states are characterized by topologies with many hadronic jets, possibly associated with leptons and missing energy. Direct decays give rise to a purely hadronic topology (Table 6.1). Indirect decays result in topologies that are a combination of hadrons, leptons and missing energy (Table 6.2). For $\tilde{\chi}_1^0\ \tilde{\chi}_1^0$ and $\tilde{\chi}_1^+\ \tilde{\chi}_1^-$ events decaying directly, the $4Jet$ and $6Jet$ selections were used, while the $6Jets + Leptons$ selection was developed for $\tilde{\chi}_1^0\ \tilde{\chi}_2^0$ events that decay indirectly. The selections implemented for decays via this coupling are listed in Table 6.5.

<table>
<tr><th colspan="2">$\bar{U}\bar{D}\bar{D}$</th></tr>
<tr><th>4Jets – broad</th><th>4Jets – broad(soft)</th></tr>
<tr><td colspan="2">$Min(N_{ch1},\ N_{ch2}) > 7,\ Min(E_{j1},\ E_{j2}) > 25\%\sqrt{s}$
$Min(M_{j1},\ M_{j2}) > 7\%\sqrt{s},\ |M_{j1} - M_{j2}| < 3\%\sqrt{s}$</td></tr>
<tr><td>$T > 0.95$</td><td>$T > 0.9$
$0.25 < InvB$</td></tr>
<tr><td colspan="2">$y_3 > 0.002$
$y_4 > 0.001$
$y_6 > 0.0003$</td></tr>
<tr><td colspan="2">$\Theta_{Thrust} < 0.97,\ E_{12^\circ} < 1\,\text{GeV},\ |p_Z| < 5\%\sqrt{s}$
$E_{jet}^{em} < 90\%E_{jet},\ \Phi_{aco} > 175^\circ$</td></tr>
<tr><th>6Jets + Leptons</th><th>6Jets</th></tr>
<tr><td>$N_{ch} > 15,\ E_{ch} > 30\%\sqrt{s},\ E_1^1 < 40\,\text{GeV}$
≥ 1 ID lepton with $\phi > 10^\circ$
$60\%\sqrt{s} < E_{vis} < 97\%\sqrt{s}$
$M_W > 90\,\text{GeV},\ |\cos\theta_{miss}| < 0.96$</td><td>$Min(N_{ch1},\ N_{ch2}) > 10,\ E_{12^\circ} < 1\,\text{GeV}$
$Min(E_{j1},\ E_{j2}) > 25\%\sqrt{s}$
$Min(M_{j1},\ M_{j2}) > 14\%\sqrt{s}$
$P_T > 2.5\%\sqrt{s},\ \Theta_{Thrust} < 0.97$</td></tr>
<tr><td>$y_4 > 0.002$
$y_6 > 0.0015$</td><td>$y_4 > 0.01$
$y_6 > 0.002$</td></tr>
<tr><td></td><td>$InvB > 0.55,\ \Phi_{aco} > 170^\circ$</td></tr>
</table>

Table 6.5: Selections for direct and indirect decays via an R-parity violating $\bar{U}\bar{D}\bar{D}$ coupling.

6.5.1 4Jets-broad

This selection is designed for events in which the lightest neutralino has a mass of less than $50\,\mathrm{GeV}/c^2$. The boost on the neutralino results in a non-spherical multi-jet topology. A preselection of at least fourteen charged tracks with seven in each jet and a minimum jet energy of at least $50\%\sqrt{s}$ with $25\%\sqrt{s}$ in each jet was required. A di-jet mass ($m_{q_1,q_2} + m_{q_3,q_4}$) was required to be at least $14\%\sqrt{s}$ with at least $7\%\sqrt{s}$ in each jet. This was also effective in rejecting $q\bar{q}$ events as illustrated in Fig. 6.11a. A cut requiring the di-jet mass difference to be no greater than $3\%\sqrt{s}$ was implemented to ensure that only events with an evenly distributed 4Jet topology were selected. To reject WW backgrounds, the event thrust was required to be at least 0.95 (Fig. 6.11b). Events were clustered into three, four and six jets and kept if $y_3,\ y_4,\ y_6$ were greater than 0.002, 0.001 and 0.0003 respectively. Fig. 6.11c shows the effect of the y_4 cut on reducing the $q\bar{q}$ background. Since the 4Jet topology was similar to the $q\bar{q}$ background, the y_i cuts were made loose in order to preserve the signal. To remove far-forward events that may arise from low energy processes, it was required that all events found around the thrust axis within 14° of the beam axis be rejected. Background arising from low energy events were further reduced by rejecting all events detected with an energy deposit greater than 1 GeV in the luminosity calorimeters, i.e. within 12° of the beam axis. To reduce background from ISR photons seen in the detector, the electromagnetic energy, E_{jet}^{em}, in any jet was required to be less than 90% of the jet energy, E_{jet}. Finally, events with a di-jet acoplanarity of less than 175° are vetoed. This selection is particularly effective for $m_{\tilde{\chi}_1^0} < 35\,\mathrm{GeV}/c^2$. The remaining background is composed mainly of $q\bar{q}$ events and can be seen in Table 6.6.

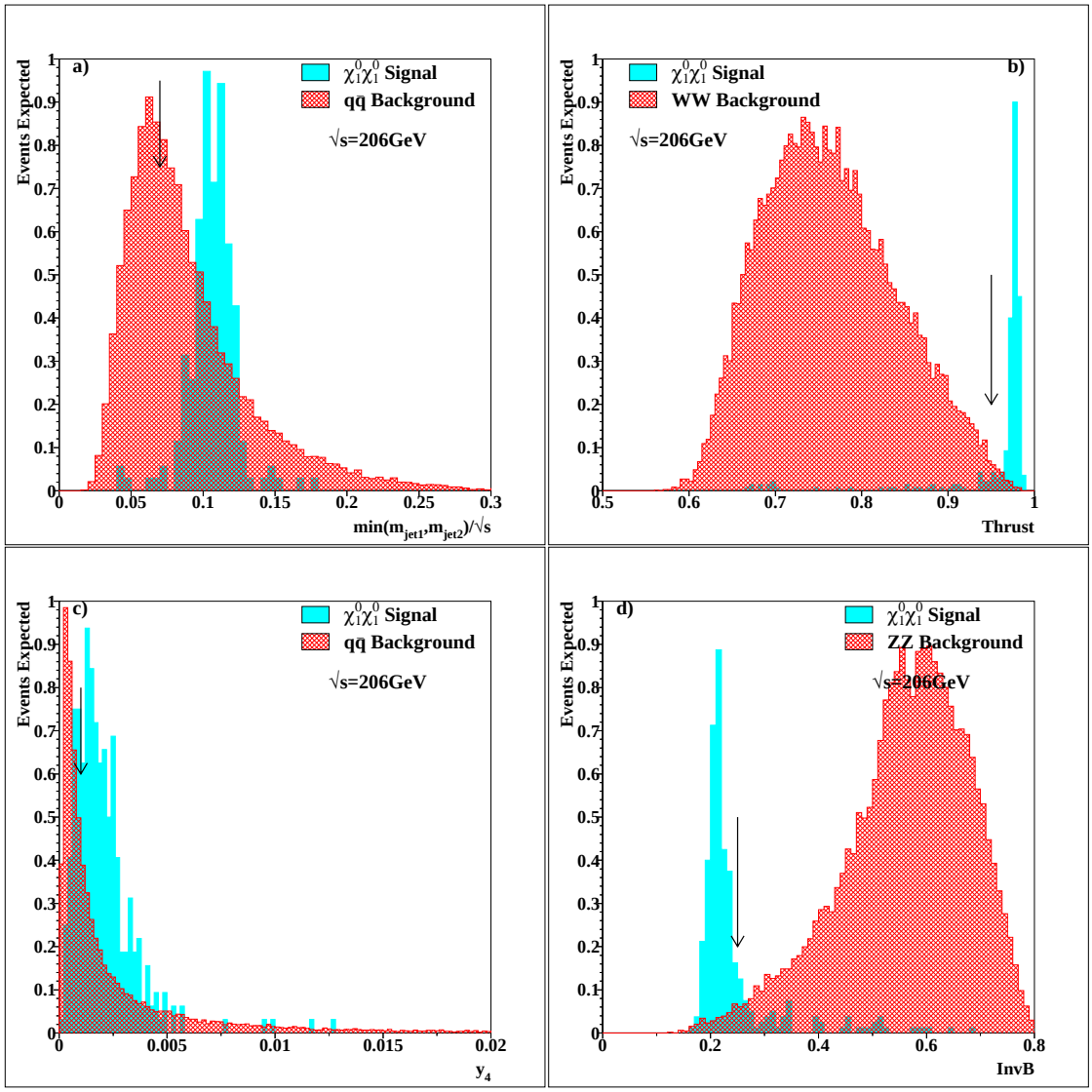

Figure 6.11: The $\tilde{\chi}_1^0$ $\tilde{\chi}_1^0$ signal for events decaying directly via the $\bar{U}\bar{D}\bar{D}$ coupling compared to the WW, $q\bar{q}$ and ZZ backgrounds after a preselection on number of charged tracks and the total jet energy, in terms of the following variables: (a) the di-jet mass. (b) The thrust. (c) The jet finding variable y_4. (d) The inverse boost. The arrows indicate the position of the cuts. All backgrounds have been normalised to the luminosity of the data. The vertical axis normalization is arbitrary.

6.5.2 4Jets-broad(soft)

This selection is effective for neutralino masses in the range $30\,\mathrm{GeV}/c^2 < m_{\tilde{\chi}_1^0} < 45\,\mathrm{GeV}/c^2$. In this range, the final state particles will not be so heavily boosted and as such, cuts on the thrust can be made less stringent. This selection is similar to the 4jets-broad selection with a few exceptions. Events with a thrust value of at least 0.9 were accepted. The inverse boost of the di-jet system was required to be not more than 0.25. This was also effective in reducing the four fermion ZZ background (Fig. 6.11d). The remaining background is composed mainly of $q\bar{q}$ events as seen in Table 6.6.

6.5.3 6Jets plus leptons

This selection was taken from [81] and optimized. A preselection of at least fifteen charged tracks with a total energy of at least $30\%\sqrt{s}$ was implemented. At least one well-isolated lepton was demanded. The leading lepton was required to have a maximum energy of not more than 40 GeV. To reduce the WW background, the hadronic mass was required to be at least $90\,\mathrm{GeV}/c^2$ (Fig. 6.12a). The visible energy was required to have a minimum energy of $60\%\sqrt{s}$ and a maximum energy of $97\%\sqrt{s}$. Events with a missing momentum vector within a 16° cone around the beam axis were rejected. This was also effective in reducing the ZZ background (Fig. 6.12b). Finally, to reject events from the $q\bar{q}$ background, the jet finding variables y_4 and y_6 were required to be greater than 0.002 and 0.0015 respectively. Fig. 6.12c illustrates the effectiveness of y_6 in rejecting $q\bar{q}$ events. The remaining background is composed of mainly WW events as shown in Table 6.6.

6.5.4 6Jets

For this selection, a preselection of least 20 charged tracks, and a total energy of at least $50\%\sqrt{s}$ was implemented. The di-jet mass was required to be at least $28\%\sqrt{s}$ with $14\%\sqrt{s}$ in each jet. This was also effective in rejecting events from the four fermion Zee background (Fig. 6.13a). To reject events from low energy background processes, the energy detected in the luminosity monitors within a 12° cone around the beam axis was required to be less than 1 GeV. To remove far-forward events from low energy processes, all events found within a 14° cone around the thrust axis were rejected. A transverse momentum of at least $2.5\%\sqrt{s}$ was required. Events from the $q\bar{q}$ background were rejected by requiring that the inverse boost be high (Fig. 6.13b). It was reduced further by clustering events into four and six jets and rejecting those for which y_4 and y_6 were less than 0.01 and 0.002 respectively. Fig. 6.13c illustrates the effectiveness of the y_6 cut in rejecting $q\bar{q}$ events. Finally, the di-jet acoplanarity was required to be greater than 170°. The remaining background was composed mainly of WW events as shown in Table 6.6.

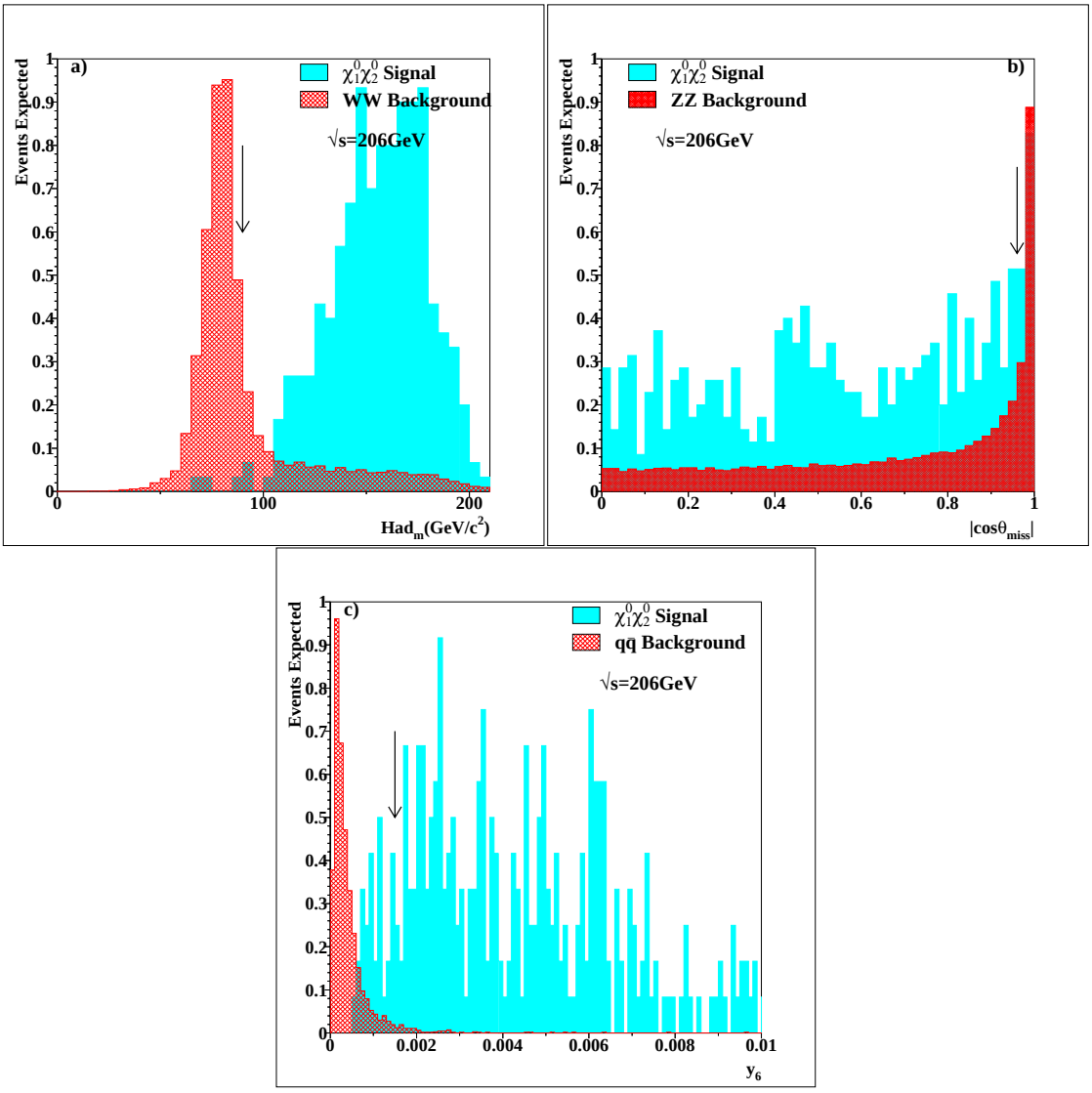

Figure 6.12: The $\tilde{\chi}_1^0$ $\tilde{\chi}_2^0$ signal for events decaying indirectly via the $\bar{U}\bar{D}\bar{D}$ coupling compared to the WW, ZZ and $q\bar{q}$ backgrounds after a preselection on number of charged tracks, the total energy of charged tracks and the number of identified leptons, in terms of the following variables: (a) The invariant hadronic mass for the process W $\rightarrow \tau\nu$qq. (b) The angle of the missing momentum vector in a cone around the beam axis. (c) The jet finding variable y_6. The arrows indicate the position of the cuts. All backgrounds have been normalised to the luminosity of the data. The vertical axis normalization is arbitrary.

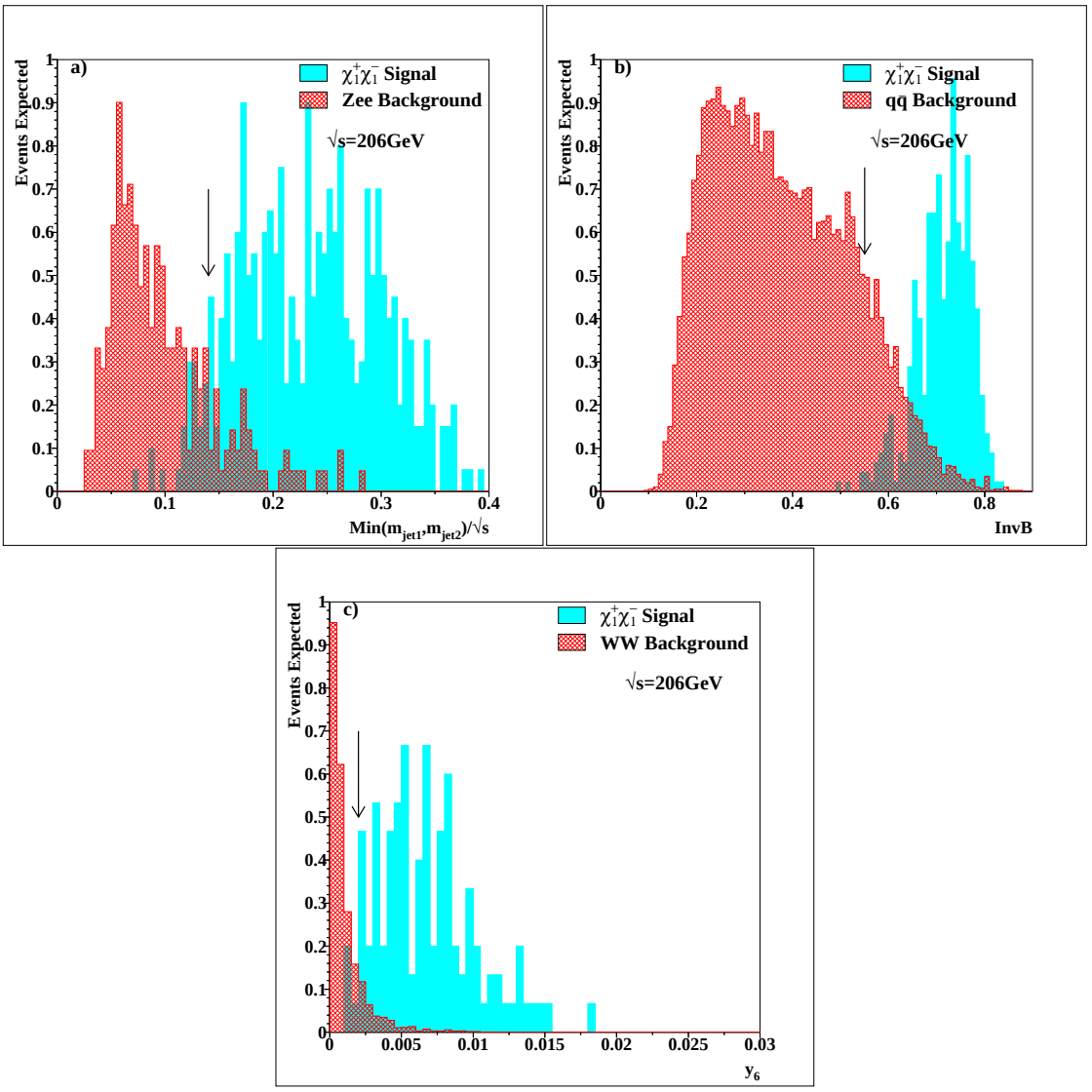

Figure 6.13: The $\tilde{\chi}_1^+$ $\tilde{\chi}_1^-$ signal for events decaying indirectly via the $\bar{U}\bar{D}\bar{D}$ coupling compared to the Zee, $q\bar{q}$ and WW backgrounds after a preselection on number of charged tracks and the total energy of charged tracks, in terms of the following variables: (a) The di-jet mass. (b) The inverse boost. (c) The jet finding variable y_6. The arrows indicate the position of the cuts. All backgrounds have been normalised to the luminosity of the data. The vertical axis normalization is arbitrary.

6.5.5 Summary

The selections listed above were used to carry out searches for $\tilde{\chi}_1^0\ \tilde{\chi}_1^0$, $\tilde{\chi}_1^0\ \tilde{\chi}_2^0$ and $\tilde{\chi}_1^+\ \tilde{\chi}_1^-$ events decaying via the $\bar{U}\bar{D}\bar{D}$ coupling. The selections were designed for searches at centre-of-mass energies from 189 GeV to 208 GeV. $\tilde{\chi}_1^0\ \tilde{\chi}_1^0$ searches were carried out using the $4Jet$ selections. $\tilde{\chi}_1^0\ \tilde{\chi}_2^0$ searches were carried out using the $6Jets + Leptons$ selection, and $\tilde{\chi}_1^+\ \tilde{\chi}_1^-$ searches were carried out using the $6Jets$ selection. The results are presented in chapter 7.

Selections	Standard Model Processes							
	ee	$\mu+\tau$	2-photon	$q\bar{q}$	WW	Weν	Zee	ZZ
$4L + \not{E}$	0	0.5	1.5	0	1.3	0	4.7	6.1
$6L + \not{E}$	0	0.1	0	0.8	0.9	0	0.6	1.3
$4J + \not{E}$	0	0.1	3.7	109.5	67.2	18.1	1.5	21.3
$4J + 2\tau$	0	0	0	6.6	25.3	0.1	1.7	4.9
$4J\!:\!Broad$	0	0	0	110.0	0.5	0	0	0.6
$4J\!:\!Broad(S)$	0	0	0	158.5	11.7	0	0.1	3.1
$6J$	0	0	0	12.0	112.5	0	0	14.1
$6J + L$	0	0	0	8.0	29.3	0	0.6	5.1
$BroadJ + L$	0	0	0	7.1	110.7	0.1	5.9	17.4
$MultiJ + L$	0	0	0	1.3	15.9	0	0.7	2.4

Table 6.6: The number of events that passed the various selections for each of the major backgrounds that was considered in this analysis. Results from the $\mu\mu$ and $\tau\tau$ backgrounds (third column) and all the 2-photon backgrounds (fourth column) have been added together. The results were obtained by running the selections on the backgrounds over a centre-of-mass energy range from 189 GeV through 208 GeV. The backgrounds were normalised to the luminosity of the data.

6.6 Conclusion

All the selections were applied to data and background Monte Carlo samples. The data and background are in good agreement. All selections were optimized to give the minimum expected 95% confidence level excluded cross section in the absence of signal for masses close to the high end of the expected sensitivity region. Selection efficiencies were determined as a function of the supersymmetric particle

Selections	$LL\bar{E}$				$LQ\bar{D}$			
	$\sqrt{s} < 199.5$ (GeV)		$\sqrt{s} > 199.5$ (GeV)		$\sqrt{s} < 199.5$ (GeV)		$\sqrt{s} > 199.5$ (GeV)	
	SM	Data	SM	Data	SM	Data	SM	Data
$4L + \not{E}$	6.6	6	7.8	10	-	-	-	-
$6L + \not{E}$	1.8	3	2.1	0	-	-	-	-
$4J + \not{E}$	-	-	-	-	102.6	127	119.0	117
$4J + 2\tau$	-	-	-	-	17.5	14	21.2	17
$L + H$ $.OR.$								
$6L + \not{E}$	13.1	15	15.0	18	-	-	-	-
$BroadJ + L$	-	-	-	-	63.2	72	78.0	64
$MultiJ + L$	-	-	-	-	9.1	18	11.2	14
	UDD							
$4J : Broad$	54.1	52	56.9	50				
$4J : Broad$ $(soft)$	83.9	91	89.5	84				
$6J$	62.2	66	76.4	75				
$6J + L$	19.5	27	23.5	25				

Table 6.7: The selections, the number of background events expected and the number of candidate events selected in the data - where J=jets, L=leptons and H=hadrons.

masses and the generation structure of the R-parity violating couplings λ_{ijk}, λ'_{ijk} and λ''_{ijk}. The systematic uncertainties on the selection efficiencies were of the order of $4-5\%$ and were dominated by the statistical uncertainty of Monte Carlo signal samples, with small additional contributions from lepton identification and energy flow reconstruction. They were taken into account by reducing the selection efficiencies by one standard deviation of the statistical error.

When setting limits, the systematic uncertainties in the background Monte Carlo were taken into consideration by [70]

- reducing the the two-fermion processes by one standard deviation of their statistical error;
- reducing the four-fermion Weν and Zee a further 20% in addition to their statistical error;

- assuming a 100% error for $\gamma\gamma \to f\bar{f}$ processes.

The Weν and Zee processes were reduced further to take into account the poor knowledge of the production cross sections in the kinematic region selected by this analysis. A 100% error is assumed for $\gamma\gamma \to f\bar{f}$ processes because of the difficulty in Monte Carlo simulation due to poor knowledge of the processes. The number of events for each Standard Model process that passed the selections taking into account the effects due to systematic uncertainties, were computed by modifying Eq. 5.1 such that

$$N_{bkg(SM)} = \frac{(100 - X)}{100} \frac{(N_{pass(SM)} - \sqrt{N_{pass(SM)}})}{N_{gen(SM)}} \times \sigma_{bkg(SM)} \times \mathcal{L}, \qquad (6.8)$$

where X is the % error introduced as a result of inefficiency of the background Monte Carlo simulation due to poor knowledge of the Standard Model process and $\sqrt{N_{pass(SM)}}$ is the standard deviation of the statistical error. Limits were then obtained as described in section 5.3 but using $N_{bkg(SM)}$ as computed in Eq. 6.8. Table 6.8 shows the number of background events after taking into account the systematic uncertainties in the Monte Carlo. On comparison with Table 6.6, it is seen that the overall effects are small. It is seen that even though a 100% error is assumed for the $\gamma\gamma$ processes, the effects on the total number of background events that pass selection is not significant. This is because the $\gamma\gamma$ processes do not dominate any channel (Table 6.6). Table 6.9 shows the comparison of Table 6.8 with data. Table 6.9 shows that even though there is a reduction in the number of background events that pass the selections, there is still good agreement between background and data. All the background processes used in this analysis were produced by various working groups in the ALEPH Collaboration.

Selections	Standard Model Processes							
	ee	$\mu+\tau$	2-photon	$q\bar{q}$	WW	Weν	Zee	ZZ
$4L+\not{E}$	0	0.3	0	0	0.9	0	4.0	5.6
$6L+\not{E}$	0	0	0	0.3	0.7	0	0.3	1.1
$4J+\not{E}$	0	0.1	0	102.6	64.5	17.5	1.0	20.5
$4J+2\tau$	0	0	0	5.0	23.7	0	1.2	4.6
$4J:Broad$	0	0	0	103.0	0.3	0	0	0.5
$4J:Broad(S)$	0	0	0	150.1	10.6	0	0	2.8
$6J$	0	0	0	9.7	109.0	0	0	13.5
$6J+L$	0	0	0	6.1	27.6	0	0.3	4.8
$BroadJ+L$	0	0	0	5.3	107.3	0	4.9	16.7
$MultiJ+L$	0	0	0	0.6	14.6	0	0.4	2.2

Table 6.8: The number of events for each of the major backgrounds that was used to set limits in this analysis. Results from the $\mu\mu$ and $\tau\tau$ backgrounds (third column) and all the 2-photon backgrounds (fourth column) have been added together.

Selections	LLE				LQD			
	$\sqrt{s}<199.5$ (GeV)		$\sqrt{s}>199.5$ (GeV)		$\sqrt{s}<199.5$ (GeV)		$\sqrt{s}>199.5$ (GeV)	
	SM	Data	SM	Data	SM	Data	SM	Data
$4L+\not{E}$	4.6	6	5.5	10	-	-	-	-
$6L+\not{E}$	1.0	3	1.2	0	-	-	-	-
$4J+\not{E}$	-	-	-	-	93.9	127	108.5	117
$4J+2\tau$	-	-	-	-	15.4	14	18.71	17
$L+H$ $.OR.$ $6L+\not{E}$	13.1	15	15.0	18	-	-	-	-
$BroadJ+L$	-	-	-	-	59.6	72	73.7	64
$MultiJ+L$	-	-	-	-	7.9	18	9.8	14
	UDD							
$4J:Broad$	50.54	52	53.2	50				
$4J:Broad$ $(soft)$	79.1	91	84.3	84				
$6J$	59.2	66	72.92	75				
$6J+L$	17.5	27	21.2	25				

Table 6.9: The selections, the number of background events expected af ter taking the systematic uncertainty of the background Monte Carlo and the number of candidate events selected in the data - where J=jets, L=leptons and H=hadrons.

Chapter 7

Results from topological searches

In the last chapter, the selections used in this analysis for neutralino and chargino searches for decays via $LL\bar{E}$, $LQ\bar{D}$ and $\bar{U}\bar{D}\bar{D}$ couplings were presented. The selections were applied to the background and data and the results show that they are in good agreement. The selections used to carry out searches were sensitive to the mass of the gauginos and also to the branching ratios of the final state particles. This dependency resulted in regions of parameter space in which the efficiency dropped to very low values. In such cases alternative searches were carried out in order to extend the neutralino mass reach.

In this chapter, results of searches are presented in three sections. In each section, results from searches for decays via a single coupling are presented. Each section is divided into two parts. In the first part, results from selection efficiencies are presented and illustrated with appropriate plots. In the second part, the limits obtained are discussed and presented in appropriate tables. For the purpose of clarity and easy comparison of results for decays via each coupling, plots showing the absolute limits for direct and indirect decays, the mass limits as a function of $\tan\beta$ and $\mu - M_2$ exclusion zones for all couplings, are grouped together at the end of chapter.

7.1 Results: $LL\bar{E}$ searches

Selection efficiency

At low m_0, searches for direct decays via $LL\bar{E}$ couplings were carried out by combining results from $\tilde{\chi}_1^0\ \tilde{\chi}_1^0$ and $\tilde{\chi}_1^0\ \tilde{\chi}_2^0$ decays. The direct decay of $\tilde{\chi}_1^0\ \tilde{\chi}_1^0$ and $\tilde{\chi}_1^0\ \tilde{\chi}_2^0$ give rise to a topology of $4L + \not{E}$ (Fig. 6.1). Application of the $4L + \not{E}$ selection to $\tilde{\chi}_1^0\ \tilde{\chi}_1^0$ events resulted in efficiencies between 23% and 45%. This was improved by considering $\tilde{\chi}_1^0\ \tilde{\chi}_2^0$ direct decays for regions of parameter space where the production cross section of $\tilde{\chi}_1^0\ \tilde{\chi}_1^0$ was not sensitive to signal and combining the results. Fig. 7.1 illustrates how this combination was implemented. Searches carried out for $\tilde{\chi}_1^0\ \tilde{\chi}_1^0$ decays via $LL\bar{E}$ couplings at centre-of-mass energies from 189 GeV to 208 GeV using the $4L + \not{E}$ selection, showed that $m_{\tilde{\chi}_1^0}$ is excluded for masses less than 39 GeV/c^2 [85]. This corresponds to an exclusion for $\sigma(\tilde{\chi}_1^0\ \tilde{\chi}_1^0) > 0.03$pb. A two dimensional scan was carried out over $\sigma(\tilde{\chi}_1^0\ \tilde{\chi}_1^0)$ and $\sigma(\tilde{\chi}_1^0\ \tilde{\chi}_2^0)$ and searches were restricted to the area for which both cross sections were less than 1pb. The value of 1pb was chosen to be as conservative as possible. The $4L + \not{E}$ selection was applied to $\tilde{\chi}_1^0\ \tilde{\chi}_2^0$ events generated at the points selected from the scan giving the improved efficiency figures of 40% and 60% shown in Fig. 7.2a.

In the case of indirect decays, the $6L + \not{E}$ selection gave efficiency values between 30% and 70% with a subset of points in parameter space yielding efficiency figures of $\approx 10\%$ (Fig. 7.2b). At these points the χ_2^0 decayed into χ_1^0 and jets resulting in more charged tracks. The low efficiency was the result of the requirement on the number of charged tracks in the $6L + \not{E}$ selection. Fig. 7.2c shows a comparison between the number of charged tracks for events at two points in parameter space for different masses of $\tilde{\chi}_1^0$ in which $\tilde{\chi}_1^0\ \tilde{\chi}_2^0$ decays indirectly. When the mass of $\tilde{\chi}_1^0$ is low, $\tilde{\chi}_2^0$ decays predominantly into $\tilde{\chi}_1^0$ and leptons. When the $\tilde{\chi}_1^0$ mass is high, $\tilde{\chi}_2^0$ decays predominantly into χ_1^0 and jets. The former gives a high efficiency and

the latter low efficiency. The points with low efficiency were found to occur in the region m_0: 0 — 50 GeV/c^2 with majority of the points occurring in the region where $\tan\beta$: 5 — 7.

At high m_0, the production cross sections of $\tilde{\chi}_1^0\ \tilde{\chi}_1^0$ and $\tilde{\chi}_1^0\ \tilde{\chi}_2^0$ are low. The low cross sections meant that it was not possible to obtain limits because σ_{95} is always greater than σ_{pr} (section 5.3). As a result searches were carried out in a manner analogous to neutralino searches but using $\tilde{\chi}_1^+\ \tilde{\chi}_1^-$ decays. In this region of parameter space the chargino decays predominantly in an indirect mode. However to be as model independent as possible, searches were carried out for both direct and indirect decays. For direct decays, searches were carried out using the $4L + \not{E}$ selection. This resulted in efficiencies of 40% to 50%. For indirect decays, an inclusive combination of the $6L + \not{E}$ selection and the Leptons+Hadrons selection was used resulting in efficiencies of 40% to 60%. Fig. 7.3 shows the selection efficiency as a function of $m_{\tilde{\chi}_1^\pm}$ for both direct and indirect decays.

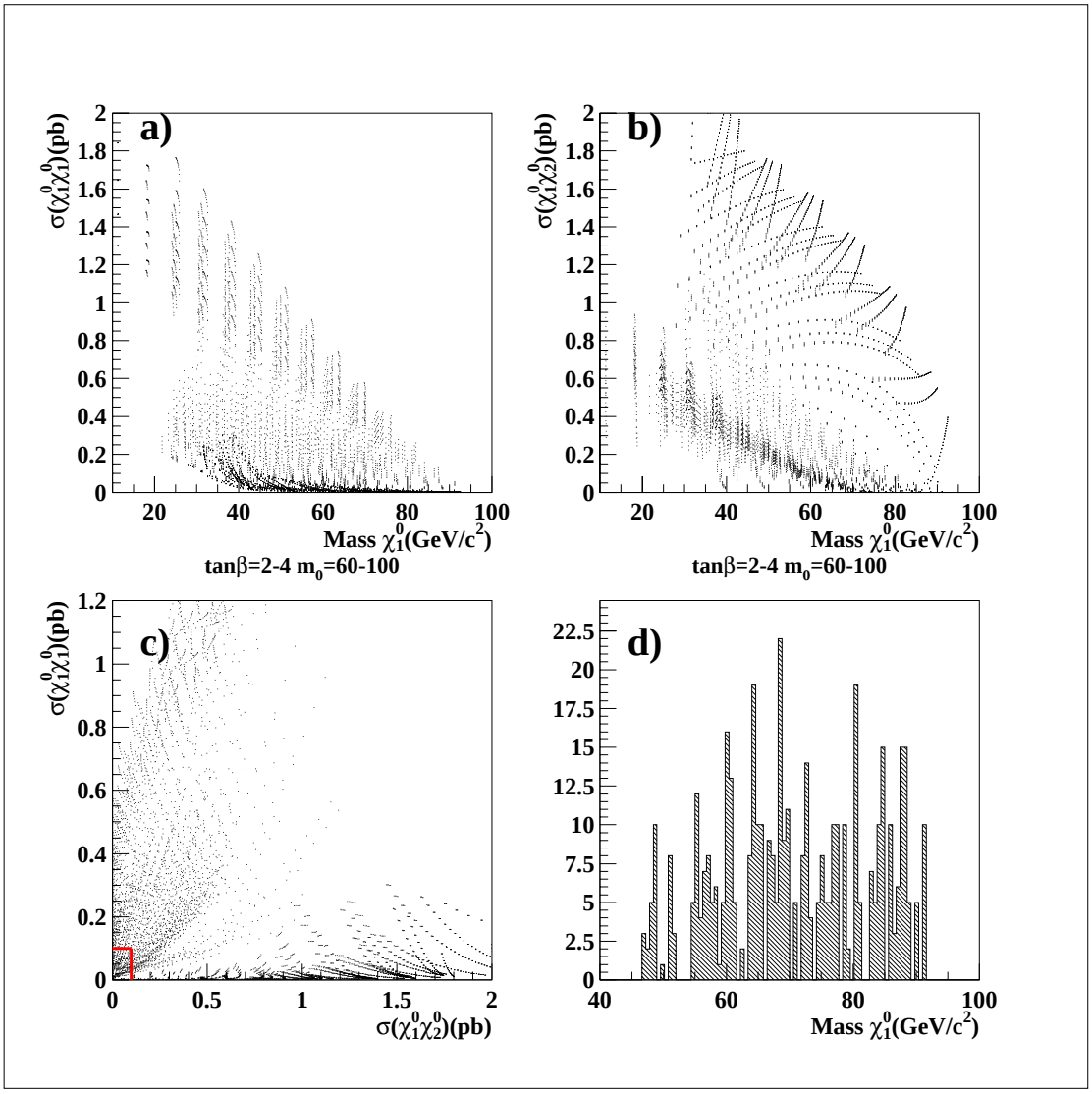

Figure 7.1: Searches for direct decays via $LL\bar{E}$ coupling by combination of $\tilde{\chi}_1^0$ $\tilde{\chi}_1^0$ and $\tilde{\chi}_1^0$ $\tilde{\chi}_2^0$ cross sections. (a) The production cross section of $\tilde{\chi}_1^0$ $\tilde{\chi}_1^0$ as a function of the lightest neutralino mass taken from Fig. 5.3. (b) The production cross section of $\tilde{\chi}_1^0$ $\tilde{\chi}_2^0$ as a function the lightest neutralino mass taken from Fig. 5.5. (c) A two dimensional combination of $\sigma(\tilde{\chi}_1^0\ \tilde{\chi}_1^0)$ and $\sigma(\tilde{\chi}_1^0\ \tilde{\chi}_2^0)$ with the marked out area in the lower left corner selected for analysis. (d) The mass of the lightest neutralino in the area selected in (c).

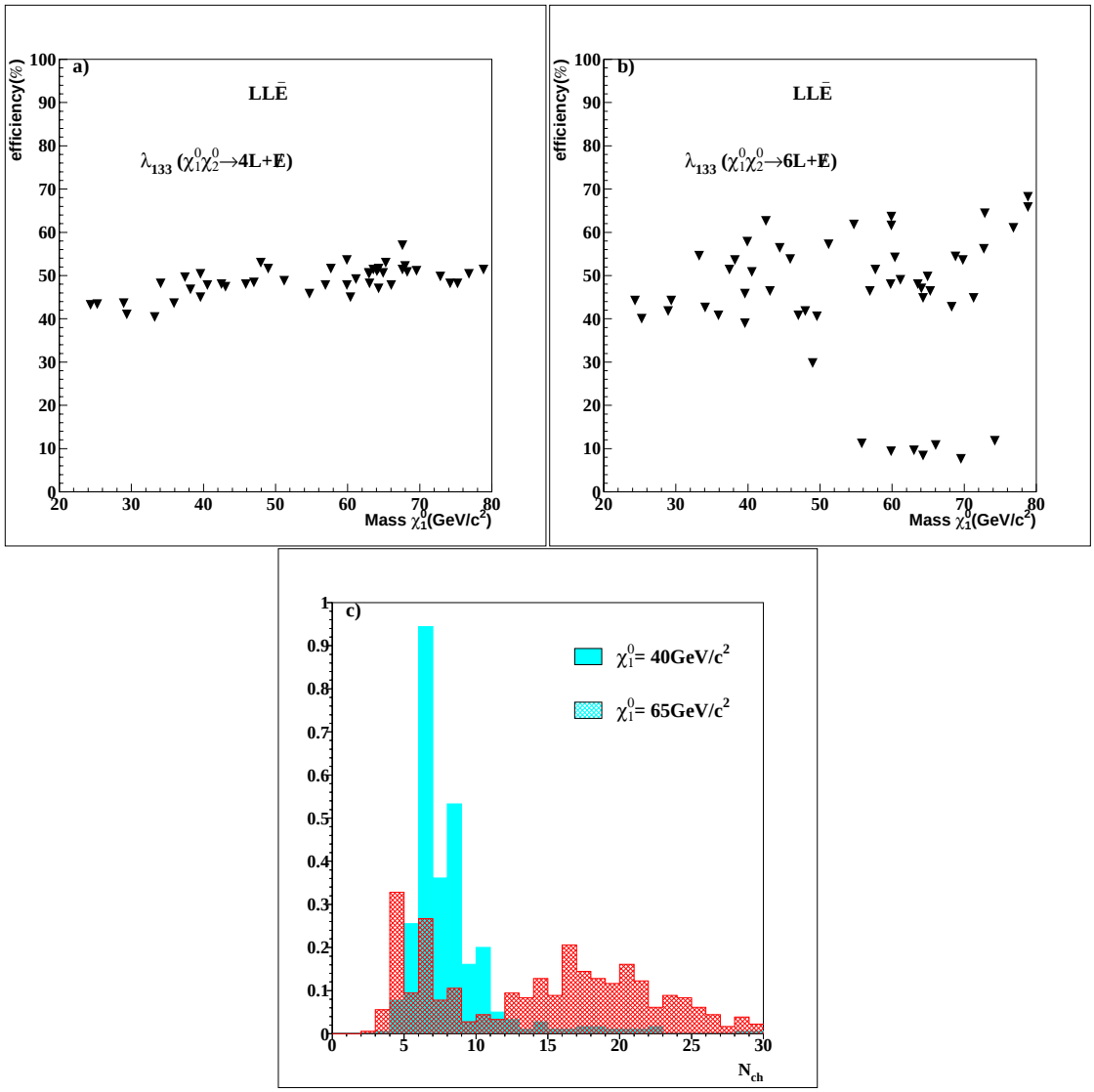

Figure 7.2: (a) The efficiency as a function of the lightest neutralino mass for direct decays via $LL\bar{E}$ coupling. At each point, 500 events were generated. (b) The efficiency as a function of the lightest neutralino mass for indirect decays via $LL\bar{E}$ coupling. At each point, 500 events were generated. A subset of points give poor efficiency due to the requirement on the number of charged tracks in the selection. (c) A comparison of the number of charged tracks for events generated at two points in parameter space taken from (b). In the first point for which $m_{\tilde{\chi}_1^0} = 40\,\mathrm{GeV}/c^2$, good selection efficiency was obtained. In the second for which $m_{\tilde{\chi}_1^0} = 65\,\mathrm{GeV}/c^2$, poor selection efficiency was obtained. In the first point, $\tilde{\chi}_2^0$ decays predominantly into $\tilde{\chi}_1^0$ plus leptons, while in the second, $\tilde{\chi}_2^0$ decays predominantly into $\tilde{\chi}_1^0$ plus jets.

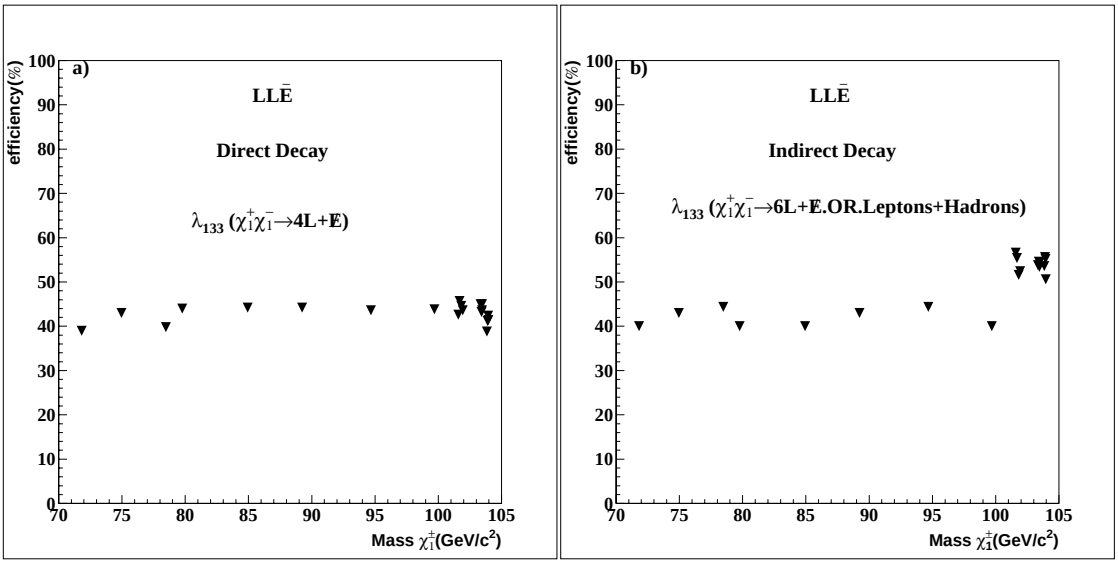

Figure 7.3: The efficiency as a function of the lightest chargino mass for (a) direct decays via $LL\bar{E}$ coupling, (b) indirect decays via $LL\bar{E}$ coupling. At each point, 500 events were generated.

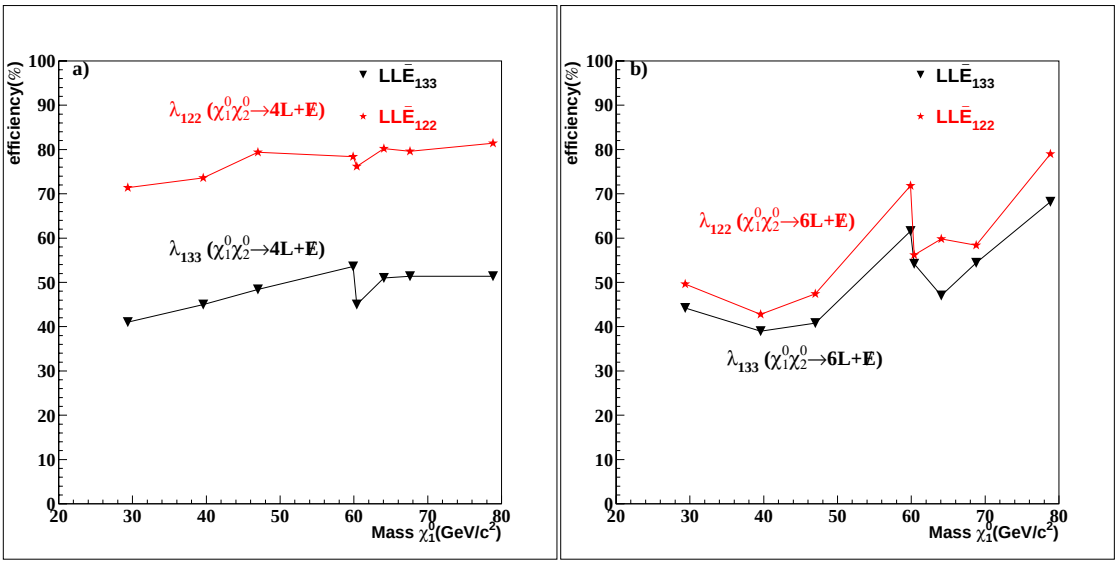

Figure 7.4: Comparison of selection efficiencies for λ_{122} and λ_{133} for (a) direct $\tilde{\chi}_1^0$ $\tilde{\chi}_2^0$ decays, (b) indirect $\tilde{\chi}_1^0$ $\tilde{\chi}_2^0$ decays.

Limits

Limits on $m_{\tilde{\chi}_1^0}$ were set using decays via λ_{133} coupling as these gave the worst efficiencies because of the presence of taus in the final state which are difficult to identify. This is illustrated in Fig. 7.4 by comparing the selection efficiency for $LL\bar{E}$ decays via λ_{133} and λ_{122}.

$LL\bar{E}$							
		direct decay		direct decay		indirect decay	
		$\tilde{\chi}_1^0\ \tilde{\chi}_1^0$		$\tilde{\chi}_1^0\ \tilde{\chi}_2^0$		$\tilde{\chi}_1^0\ \tilde{\chi}_2^0$	
$\tan\beta$	$\mathbf{m_0}$	**eff**	**limit** $\tilde{\chi}_1^0$	**eff**	**limit** $\tilde{\chi}_1^0$	**eff**	**limit** $\tilde{\chi}_1^0$
	(GeV/c^2)	(%)	(GeV/c^2)	(%)	(GeV/c^2)	(%)	(GeV/c^2)
2 - 4	0 - 50	23 - 42	39.1	49 - 57	73.5	64 - 66	77.4
2 - 4	60 - 100	28 - 39	38.9	41 - 53	60.2	47 - 54	64.3
5 - 7	0 - 50	36 - 43	47.9	47 - 48	63.4	9 - 11	58.7
5 - 7	60 - 100	31 - 44	47.8	49 - 51	62.9	45 - 54	64.8
8 - 10	0 - 50	36 - 45	49.5	47 - 50	65.7	11 - 50	65.3
8 - 10	60 - 100	36 - 42	49.4	51 - 53	64.1	48 - 56	67.3
20 - 50	0 - 50	38 - 45	50.8	51 - 52	68.1	8 - 48	64.3
20 - 50	60 - 100	40 - 42	42.1	50 - 51	67.8	43 - 45	69.6

Table 7.1: The mass limits obtained in different regions of parameter space for which $\tilde{\chi}_1^0\ \tilde{\chi}_1^0$ and $\tilde{\chi}_1^0\ \tilde{\chi}_2^0$ events decayed via the λ_{133} ($LL\bar{E}$) coupling. The efficiencies were obtained by applying the various selections shown in Table 6.3 to the signal. The absolute mass limits of 38.9 GeV/c^2 and 60.2 GeV/c^2 were obtained for the direct decay of $\tilde{\chi}_1^0\ \tilde{\chi}_1^0$ and $\tilde{\chi}_1^0\ \tilde{\chi}_2^0$ in the region $\tan\beta$: 2 — 4, m_0: 60 — 100 GeV/c^2, and 58.7 GeV/c^2 for the indirect decay of $\tilde{\chi}_1^0\ \tilde{\chi}_2^0$ in the region $\tan\beta$: 5 — 7, m_0: 0 — 50 GeV/c^2.

In each section of parameter space scanned, the mass limits were derived by obtaining the upper limit on the cross section at 95% confidence level σ_{95}, as described in section 5.3. This was compared to the production cross section, σ_{pr}, and the limit on the mass was obtained at the point where $\sigma_{95} < \sigma_{pr}$. Tables 7.1 and 7.2 show the mass limit obtained in all regions of parameter space scanned for $\tilde{\chi}_1^0\ \tilde{\chi}_1^0$, $\tilde{\chi}_1^0\ \tilde{\chi}_2^0$ and $\tilde{\chi}_1^+\ \tilde{\chi}_1^-$ decays. The absolute limit is obtained in the region with the lowest mass limit. Fig. 7.11 shows plots of the efficiency as a function of mass in the region where the absolute mass limit is obtained. The corresponding plots

$LL\bar{E}$					
decay mode	$\tan\beta$	$\mathbf{m_0}$ (GeV/c^2)	**eff** (%)	**limit** $\tilde{\chi}_1^+$(GeV/c^2)	**bound** $\tilde{\chi}_1^0$(GeV/c^2)
direct	2 - 4	200 - 500	41 - 47	102.7	50.9
	5 - 7	200 - 500	35 - 45	103.3	50.9
	8 - 10	200 - 500	43 - 45	103.0	50.9
	20 - 50	200 - 500	41 - 46	102.8	50.9
Indirect	2 - 4	200 - 500	54 - 56	102.7	50.9
	5 - 7	200 - 500	51 - 54	103.5	50.9
	8 - 10	200 - 500	54 - 57	103.1	50.9
	20 - 50	200 - 500	52 - 55	102.9	50.9

Table 7.2: Results obtained from searches for $\tilde{\chi}_1^+$ $\tilde{\chi}_1^-$ events decaying directly and indirectly via the λ_{133} ($LL\bar{E}$) couplings. Bounds indicate limits on the neutralino mass obtained by excluding chargino masses. The efficiency figures correspond to points that were selected after doing a fine scan in Fig. 5.6.

of σ_{95} superimposed over σ_{pr} to obtain the absolute mass limits of 60.2 GeV/c^2 for direct decays and 58.7 GeV/c^2 for indirect decays, are shown in Fig. 7.12.

Though indirect decays in general gave better limits as a result of greater sensitivity in production cross section, there were some regions which gave worse limits compared to the direct decays due to the drop in efficiency at points in the region $\tan\beta$: 5 — 7, m_0: 0 — 60 GeV/c^2 where the lightest neutralino mass was greater than 50 GeV/c^2. This anomaly can be seen clearly when the mass limits are plotted as a function of $\tan\beta$, as illustrated in Fig. 7.15a. The peaks are a result of the difference in limits in the two separate regions of low m_0 for the same $\tan\beta$.

The absolute limit of 60.2 GeV/c^2 was mapped onto the $\mu - M_2$ plane and is illustrated in Figs. 7.16 and 7.17. In addition, limits obtained in the region $\tan\beta$: 20 — 50, , were also mapped onto the $\mu - M_2$ plane. This is shown in Figs. 7.18 and 7.19. Apart from a small increase in the LEP I excluded gaugino mass region for $+\mu$, there are no significant differences in the distribution of the excluded $\mu - M_2$ regions at low $\tan\beta$ and high $\tan\beta$ for $m_0 = 60$ GeV/c^2. For $m_0 = 100$ GeV/c^2, the excluded $\mu - M_2$ distribution at high $\tan\beta$ is almost symmetrical about μ, with

more area excluded compared to the distribution at low $\tan\beta$.

7.2 Results: $LQ\bar{D}$ searches

Selection efficiency

In the low m_0 region $\tilde{\chi}_1^0\ \tilde{\chi}_1^0$ events decaying via an $LQ\bar{D}$ coupling gave rise to a predominantly $4J + \not{E}$ topology. Searches were carried out for these decays using the $4J + \not{E}$ selection (Table 6.4). Resulting efficiencies were low - between 2% and 30%. At low $m_{\tilde{\chi}_1^0}$, the jets and missing momentum vectors have a significant boost in the centre-of-mass frame. This results in two broad jets being formed rather than four distinct jets with the missing momentum vector lying very close to the jet. This makes resolution of the vector quite difficult. Thus the topology is very much like the $q\bar{q}$ and WW background, making it difficult to extract a signal.

It was not possible to set a limit in the region $\tan\beta$: 2 — 4, m_0: 60 — 100 GeV/c^2 using searches for $\tilde{\chi}_1^0\ \tilde{\chi}_1^0$ decays. Alternate searches were carried out using $\tilde{\chi}_1^0\ \tilde{\chi}_2^0$ decays, which provided better sensitivity as a result of higher cross sections. In the direct decay of $\tilde{\chi}_1^0\ \tilde{\chi}_2^0$ events, the χ_1^0 decays predominantly into a jet and missing energy while the χ_2^0 decays into a jet and a τ. The $4J+2\tau$ selection was used to search for signal with a selection efficiency of $\approx 10\%$ (Fig. 7.5a). The low efficiency is the result of the presence of missing energy and the absence of leptons. However, the increased sensitivity in production cross section resulted in improved limits being obtained in all regions of parameter space scanned. It was not possible to use the method of combining results from $\tilde{\chi}_1^0\ \tilde{\chi}_1^0$ and $\tilde{\chi}_1^0\ \tilde{\chi}_2^0$ direct decay searches as was done in the case of $LL\bar{E}$ couplings since the direct decays of both the $\tilde{\chi}_1^0\ \tilde{\chi}_1^0$ and $\tilde{\chi}_1^0\ \tilde{\chi}_2^0$ channels produced a variety of topologies (Table 6.1) unlike the $LL\bar{E}$ case where the $\tilde{\chi}_1^0\ \tilde{\chi}_1^0$ and $\tilde{\chi}_1^0\ \tilde{\chi}_2^0$ channels produced only one topology - $4L + \not{E}$. Unless the $\tilde{\chi}_1^0\ \tilde{\chi}_1^0$ and $\tilde{\chi}_1^0\ \tilde{\chi}_2^0$ events are generated specifically at every

point in parameter space, there is no way *a priori* that one can predict which topologies will be dominant.

Searches were carried out for indirect $\tilde{\chi}_1^0\ \tilde{\chi}_2^0$ decays using the *Broadjets+Lepton* selection. This selection yielded efficiencies between 10% and 40% and is most effective for neutralino masses between $50\,\mathrm{GeV}/c^2$ and $70\,\mathrm{GeV}/c^2$. Fig. 7.5 shows the selection efficiency as a function of mass for the various points in parameter space used in obtaining limits for both direct and indirect decays.

Selection efficiencies for both direct and indirect decays were found to have negligible dependency on the λ'_{ijk} coupling and is illustrated in Fig. 7.6. For $\tilde{\chi}_1^0\ \tilde{\chi}_1^0$ decays, the dominant topology is the $4Jets + \not{E}$ topology. The other topologies of $4Jets + 2Leptons$ and $4Jets + 1Lepton + \not{E}$ (Table 6.1) provide an insignificant contribution to the overall final state composition. For $\tilde{\chi}_1^0\ \tilde{\chi}_1^0$ decays, χ_1^0 decays into a quark jet plus missing energy and χ_2^0 into χ_1^0 plus leptons, makes it difficult to establish which couplings lead to the worst efficiencies as the selection is more jet-dependent than lepton dependent. As a result, there was no significant difference in selection efficiencies obtained from decays via λ'_{211} and λ'_{311} couplings. For the purpose of consistency, decays via λ'_{311} were used to set limits.

In the high m_0 region, chargino searches were carried out and used to set bounds on the mass of the neutralino. In this region of parameter space, the chargino decays predominantly via the indirect decay mode. However, searches were carried out for both direct and indirect decays in order to be as model independent as possible. For direct decays, the $4J + 2\tau$ selection was used while the $Multijets + Leptons$ selection was used for indirect decays. Selection efficiencies were between 12% and 20% for direct decays and 20% and 50% for indirect decays (Fig. 7.7).

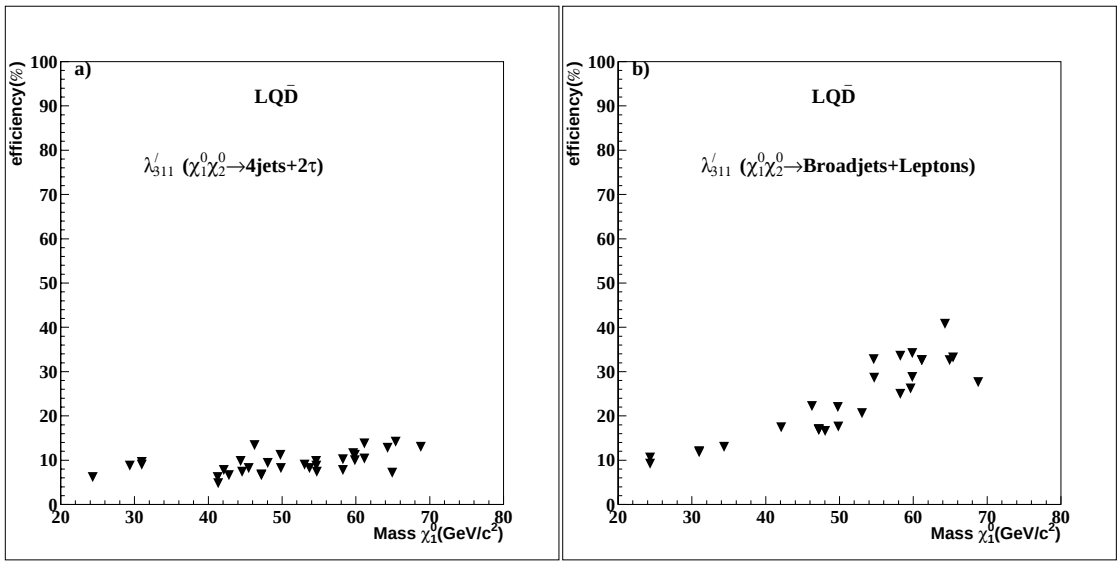

Figure 7.5: The efficiency as a function of the lightest neutralino mass for (a) direct decays via $LQ\bar{D}$ coupling, (b) indirect decays via $LQ\bar{D}$ coupling. At each point, 500 events were generated.

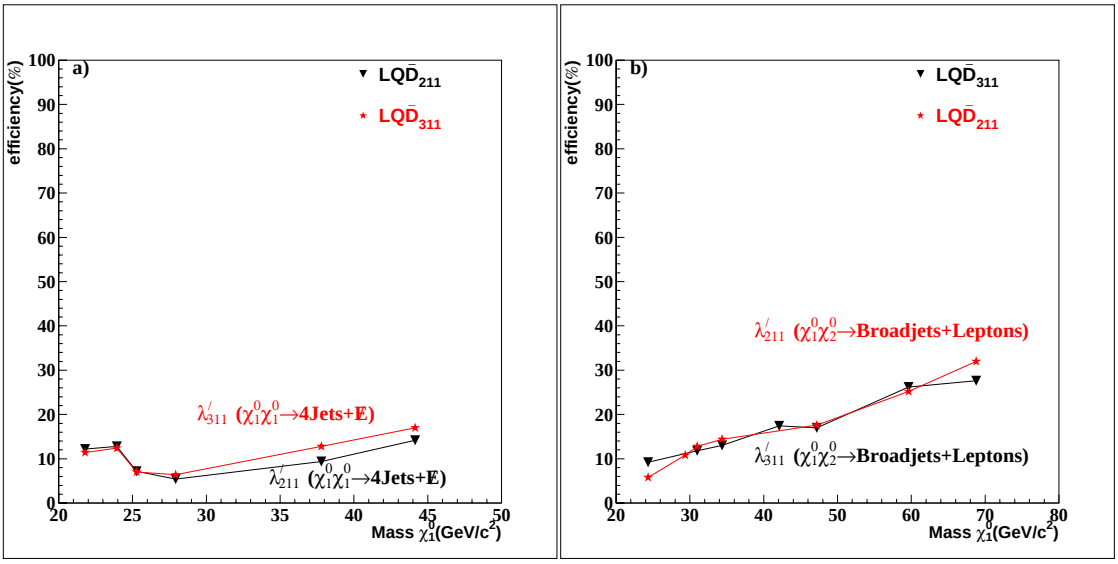

Figure 7.6: Comparison of selection efficiencies for λ'_{211} and λ'_{311} for (a) direct $\tilde{\chi}^0_1$ $\tilde{\chi}^0_1$ decays, (b) indirect $\tilde{\chi}^0_1$ $\tilde{\chi}^0_2$ decays.

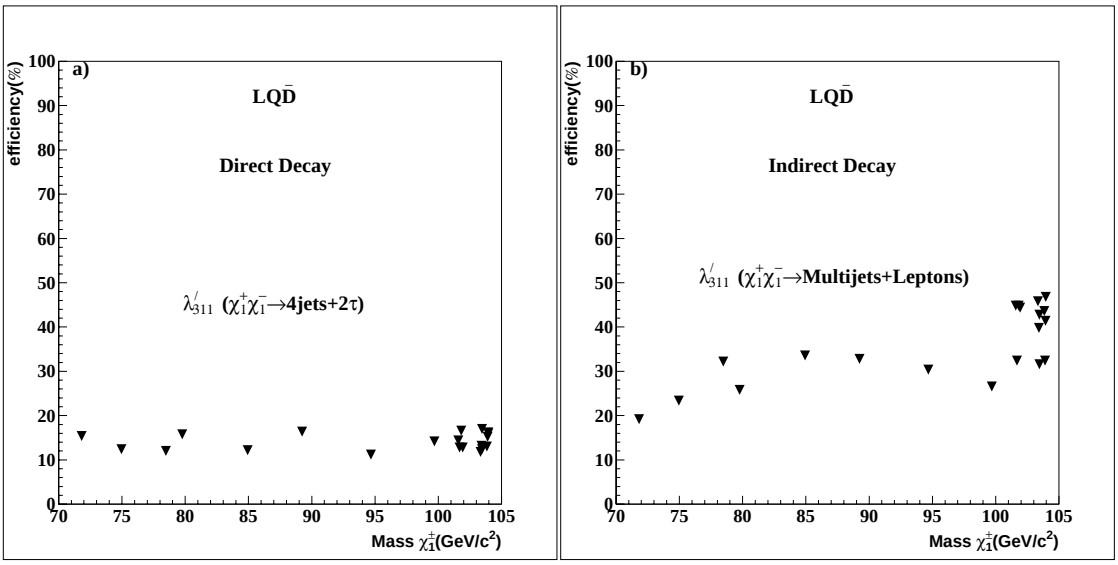

Figure 7.7: The efficiency as a function of the lightest chargino mass for (a) direct decays via $LQ\bar{D}$ coupling, (b) indirect decays via $LQ\bar{D}$ coupling. At each point, 500 events were generated.

Limits

In each section of parameter space scanned, the mass limits were derived by obtaining the upper limit on the cross section at 95% confidence level σ_{95}. This was compared to the production cross section - σ_{pr}, and the limit on the mass was obtained at the point where $\sigma_{95} < \sigma_{pr}$. Tables 7.3 and 7.4 show the mass limit obtained for $\tilde{\chi}_1^0\ \tilde{\chi}_1^0$, $\tilde{\chi}_1^0\ \tilde{\chi}_2^0$ and $\tilde{\chi}_1^+\ \tilde{\chi}_1^-$ decays. The absolute limit is obtained in the region with the lowest mass limit. Fig. 7.11 shows plots of the efficiency as a function of mass in the region where the absolute mass limit is obtained. The corresponding plots of σ_{95} superimposed over σ_{pr} to obtain the absolute mass limits of 42.3 GeV/c^2 for direct decays and 44.2 GeV/c^2 for indirect decays, are shown in Fig. 7.13.

$LQ\bar{D}$							
		direct decay		direct decay		indirect decay	
		$\tilde{\chi}_1^0\ \tilde{\chi}_1^0$		$\tilde{\chi}_1^0\ \tilde{\chi}_2^0$		$\tilde{\chi}_1^0\ \tilde{\chi}_2^0$	
$\tan\beta$	$\mathbf{m_0}$	**eff**	**limit** $\tilde{\chi}_1^0$	**eff**	**limit** $\tilde{\chi}_1^0$	**eff**	**limit** $\tilde{\chi}_1^0$
	(GeV/c^2)	(%)	(GeV/c^2)	(%)	(GeV/c^2)	(%)	(GeV/c^2)
2 - 4	0 - 50	10 - 16	24.0	6 -10	44.3	10 - 28	48.8
2 - 4	60 - 100	6 - 13	-	6 - 13	42.3	9 - 27	44.2
5 - 7	0 - 50	9 - 22	33.8	9 - 13	51.4	20 - 40	60.5
5 - 7	60 - 100	8 - 13	29.6	5 - 11	45.3	16 - 28	48.5
8 - 10	0 - 50	8 - 20	32.5	7 - 10	54.2	32 - 33	61.4
8 - 10	60 - 100	8 - 20	31.1	6 - 11	45.2	22 - 25	51.0
20 - 50	0 - 50	4 - 21	34.5	10 - 14	56.1	32 - 33	61.4
20 - 50	60 - 100	2 - 23	30.5	10 - 13	48.7	22 - 32	54.3

Table 7.3: The mass limit obtained in different regions of parameter space for which $\tilde{\chi}_1^0\ \tilde{\chi}_1^0$ and $\tilde{\chi}_1^0\ \tilde{\chi}_2^0$ events decayed via the λ'_{311} ($LQ\bar{D}$) coupling. The efficiencies were obtained by applying the various selections shown in Table 6.4 to the signal. The absolute mass limits of 42.3 GeV/c^2 and 44.2 GeV/c^2 were obtained for the direct and indirect decay of $\tilde{\chi}_1^0\ \tilde{\chi}_2^0$ in the region $\tan\beta$: 2 — 4, m_0: 60 — 100 GeV/c^2. No absolute mass limit for $\tilde{\chi}_1^0\ \tilde{\chi}_1^0$ decays was obtained due to poor selection efficiency.

Fig. 7.15b shows the neutralino mass limits as a function of $\tan\beta$. As illustrated, indirect decays gave slightly better limits compared to direct decays due to the more

$LQ\bar{D}$					
decay mode	$\tan\beta$	$\mathbf{m_0}$ (GeV/c^2)	**eff** (%)	**limit** $\tilde{\chi}_1^+$(GeV/c^2)	**bound** $\tilde{\chi}_1^0$(GeV/c^2)
direct	2 - 4	200 - 500	12 - 15	101.8	50.9
	5 - 7	200 - 500	12 - 17	102.3	50.9
	8 - 10	200 - 500	13 - 15	101.9	50.9
	20 - 50	200 - 500	13 - 17	102.1	50.9
indirect	2 - 4	200 - 500	31 - 33	102.3	50.9
	5 - 7	200 - 500	45 - 47	102.9	50.9
	8 - 10	200 - 500	40 - 45	102.8	50.9
	20 - 50	200 - 500	41 - 44	102.8	50.9

Table 7.4: Results obtained from searches for $\tilde{\chi}_1^+\ \tilde{\chi}_1^-$ events decaying directly and indirectly via the λ'_{311} ($LQ\bar{D}$) couplings. Bounds indicate limits on the neutralino mass obtained by excluding chargino masses. The efficiency figures correspond to points that were selected after doing a fine scan in Fig. 5.6.

robust requirements of the indirect decay selection which was designed to accept a combination of topologies in contrast to the direct decay selection which was designed to select a single topology. The peaks are as a result of the difference in limits in the two separate regions of the low m_0 for the same $\tan\beta$.

The limits were also mapped onto the $\mu - M_2$ plane as shown in Figs. 7.16 and 7.17. In addition, limits obtained in the region $\tan\beta$: 20 — 50, were also mapped onto the $\mu - M_2$ plane. This is shown in Figs. 7.18 and 7.19. Apart from a small increase in the LEP I excluded gaugino mass region for $+\mu$, there are no significant differences in the distribution of the excluded $\mu - M_2$ regions at low $\tan\beta$ and high $\tan\beta$ for $m_0 = 60\,\mathrm{GeV}/c^2$. For $m_0 = 100\,\mathrm{GeV}/c^2$, the excluded $\mu - M_2$ distribution at high $\tan\beta$ is almost symmetrical about μ, with more area excluded compared to the distribution at low $\tan\beta$.

7.3 Results: $\bar{U}\bar{D}\bar{D}$ searches

Selection efficiency

In the low m_0 region, $\tilde{\chi}_1^0\ \tilde{\chi}_1^0$ decays directly via the $\bar{U}\bar{D}\bar{D}$ coupling into six jets. However, when the mass of the lightest neutralino is low, $\tilde{\chi}_1^0\ \tilde{\chi}_1^0$ decays directly into four broad jets rather than six distinct jets due to the boost acting on the neutralino in the centre-of-mass frame. Events in this region of parameter space for which $20\,\mathrm{GeV}/c^2 < m_{\tilde{\chi}_1^0} < 45\,\mathrm{GeV}/c^2$ are characterized by high thrust. The thrust, T, fluctuates for masses in the range $20\,\mathrm{GeV}/c^2$ to $35\,\mathrm{GeV}/c^2$. Fig. 7.8c shows a comparison of T for events generated at two points in parameter space for which $\Delta m_{\tilde{\chi}_1^0} < 15\,\mathrm{GeV}/c^2$. In order to accommodate the thrust fluctuation, two selections - the 4Jets-broad and 4Jets-broad (soft) were used to carry out searches. The soft 4Jet selection required less stringent cuts on the thrust. Fig. 7.8a shows the efficiency distribution as a function of mass for points selected. The selection efficiency varied between 10% and 40% for masses less than $45\,\mathrm{GeV}/c^2$ and was less than 10% for masses greater than $45\,\mathrm{GeV}/c^2$.

For indirect $\tilde{\chi}_1^0\ \tilde{\chi}_2^0$ decays, the 6Jets+Lepton selection was used. Selection efficiencies obtained were in the range 10% to 30%. This is illustrated in Fig. 7.8b.

For direct decays, the selection efficiencies were found to have negligible dependency on the λ''_{ijk} coupling. As illustrated in Fig. 7.9a, comparison of decays via λ''_{112} and λ''_{223} couplings show insignificant dependence on selection efficiency. For indirect decays, the selection efficiencies exhibit dependency on the λ''_{ijk} couplings. Decays via λ''_{112} coupling gave better selection efficiencies compared to decays via the λ''_{223} coupling (Fig. 7.9b).

In the high m_0 region, chargino ($\tilde{\chi}_1^+\ \tilde{\chi}_1^-$) searches were carried out. In this region of parameter space, the chargino decays predominantly via the indirect mode. However searches were carried out for both direct and indirect decays in

order to be as model independent as possible. For direct decays, the chargino decays into six jets. The 6Jets selection was used to carry out searches. This resulted in efficiencies between 13% and 20%. For indirect decays, the chargino decays into a multijet or multijet plus lepton topologies. The 6Jets selection was used to carry out searches, resulting in efficiencies between 22% and 31%. Fig. 7.10 shows the selection efficiency as a function of $m_{\tilde{\chi}_1^\pm}$ for both direct and indirect decays.

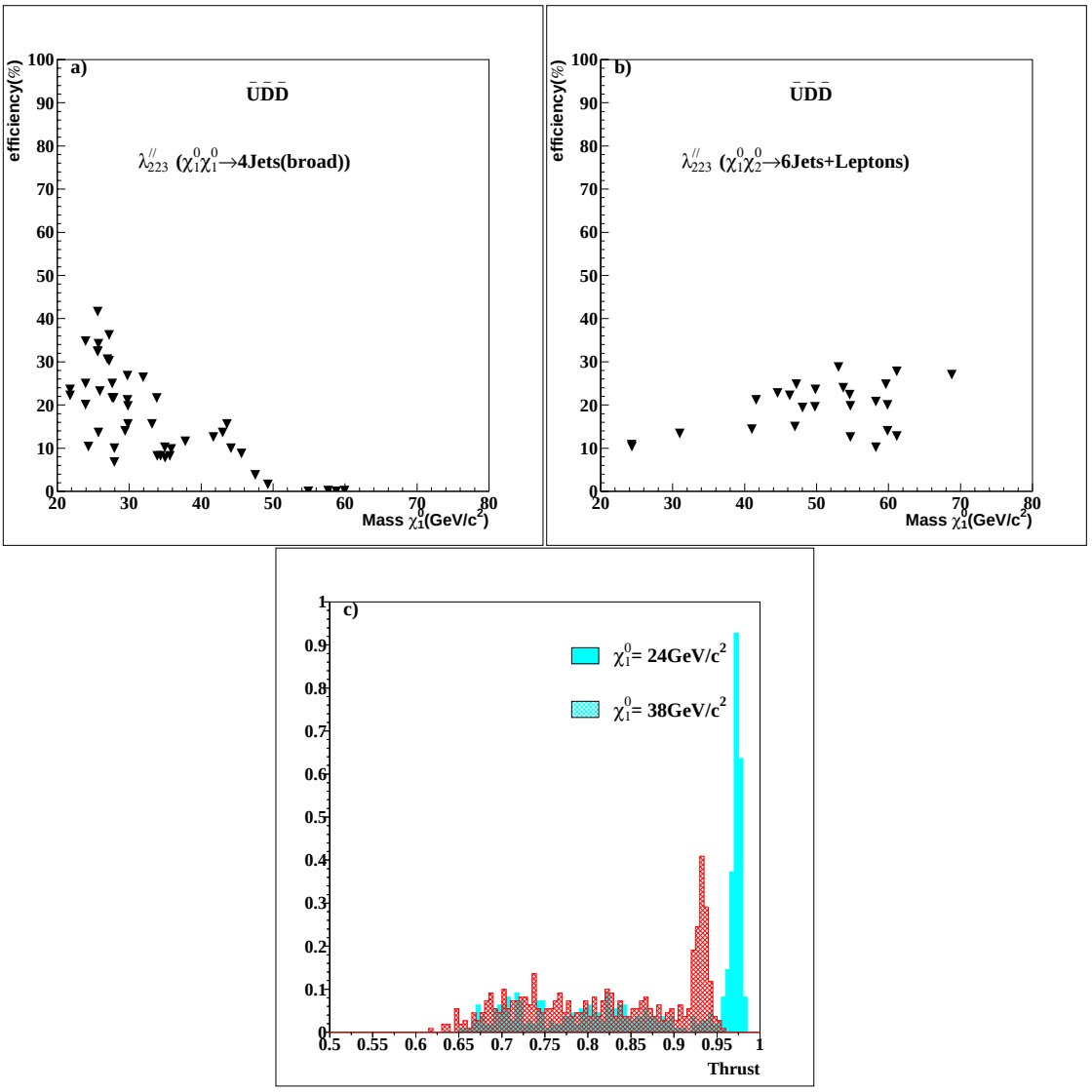

Figure 7.8: (a) The efficiency as a function of the lightest neutralino mass for direct decays via $\bar{U}\bar{D}\bar{D}$ coupling. At each point, 500 events were generated. (b) The efficiency as a function of the lightest neutralino mass for indirect decays via $\bar{U}\bar{D}\bar{D}$ coupling. At each point, 500 events were generated. (c) A comparison of the thrust for events generated at two points taken from (a) for which $\Delta m_{\tilde{\chi}^0_1} < 15\,\text{GeV}$. The y-axis normalization is arbitrary.

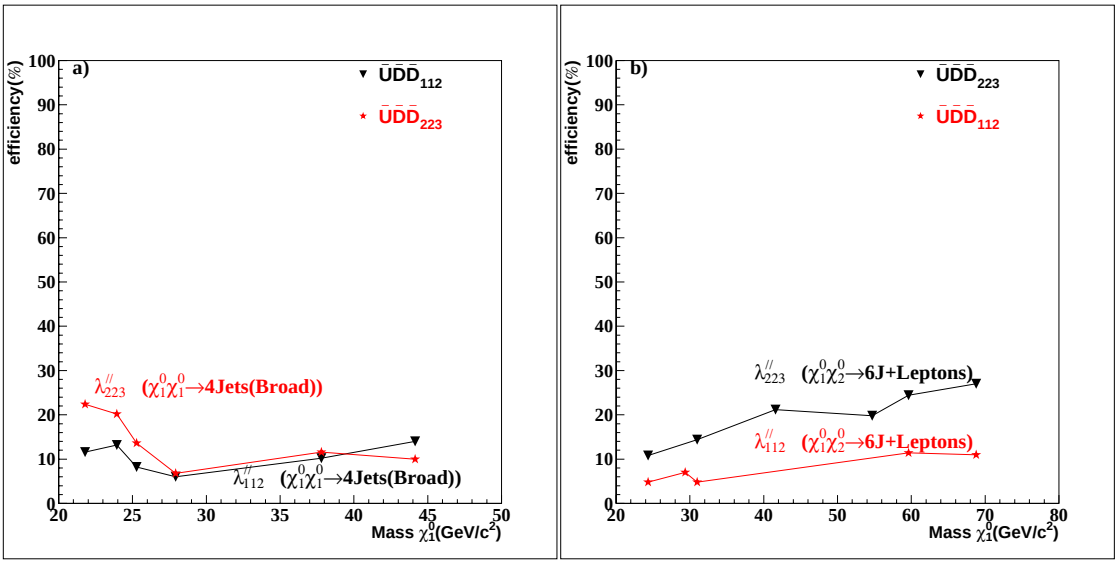

Figure 7.9: Comparison of selection efficiencies for λ''_{112} and λ''_{223} for (a) direct $\tilde{\chi}^0_1$ $\tilde{\chi}^0_1$ decays, (b) indirect $\tilde{\chi}^0_1$ $\tilde{\chi}^0_2$ decays.

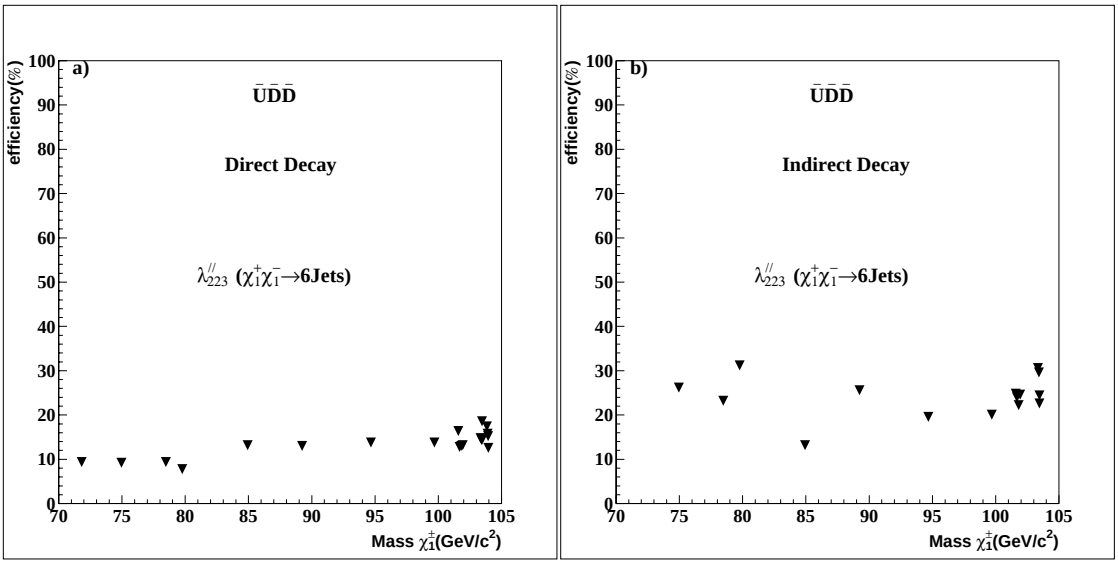

Figure 7.10: The efficiency as a function of the lightest chargino mass for (a) direct decays via $\bar{U}\bar{D}\bar{D}$ coupling, (b) indirect decays via $\bar{U}\bar{D}\bar{D}$ coupling. At each point, 500 events were generated.

$\bar{U}\bar{D}\bar{D}$					
		direct decay		indirect decay	
		$\tilde{\chi}_1^0\ \tilde{\chi}_1^0$		$\tilde{\chi}_1^0\ \tilde{\chi}_2^0$	
$\tan\beta$	$\mathbf{m_0}$ (GeV/c^2)	**eff** (%)	**limit** $\tilde{\chi}_1^0$ (GeV/c^2)	**eff** (%)	**limit** $\tilde{\chi}_1^0$ (GeV/c^2)
2 - 4	0 - 50	10 - 25	27.9	10 - 24	49.5
2 - 4	60 - 100	7 - 22	25.9	10 - 27	42.2
5 - 7	0 - 50	8 - 34	34.5	14 - 28	55.5
5 - 7	60 - 100	8 - 23	31.9	19 - 23	51.8
8 - 10	0 - 50	10 - 32	34.0	10 - 24	54.3
8 - 10	60 - 100	8 - 32	33.4	15 - 20	50.4
20 - 50	0 - 50	10 - 36	35.7	12 - 22	57.0
20 - 50	60 - 100	8 - 42	35.0	22 - 27	54.8

Table 7.5: The mass limit obtained in different regions of parameter space for which $\tilde{\chi}_1^0\ \tilde{\chi}_1^0$ and $\tilde{\chi}_1^0\ \tilde{\chi}_2^0$ events decayed via the λ''_{223} ($\bar{U}\bar{D}\bar{D}$) coupling. The efficiencies were obtained by applying the various selections shown in Table 6.5 to the signal. The absolute mass limits of 25.9 GeV/c^2 and 42.2 GeV/c^2 were obtained for the direct and indirect decay of $\tilde{\chi}_1^0\ \tilde{\chi}_1^0$ and $\tilde{\chi}_1^0\ \tilde{\chi}_2^0$ in the region $\tan\beta$: 2 — 4, m_0: 60 — 100 GeV/c^2.

$\bar{U}\bar{D}\bar{D}$					
decay mode	$\tan\beta$	$\mathbf{m_0}$ (GeV/c^2)	**eff** (%)	**limit** $\tilde{\chi}_1^+$(GeV/c^2)	**bound** $\tilde{\chi}_1^0$(GeV/c^2)
direct	2 - 4	200 - 500	13 - 16	101.8	50.9
	5 - 7	200 - 500	13 - 15	102.0	50.9
	8 - 10	200 - 500	14 - 18	102.0	50.9
	20 - 50	200 - 500	13 - 19	101.3	50.9
indirect	2 - 4	200 - 500	23 - 24	101.9	50.9
	5 - 7	200 - 500	22 - 31	102.4	50.9
	8 - 10	200 - 500	25 - 30	102.2	50.9
	20 - 50	200 - 500	24 - 25	102.2	50.9

Table 7.6: Results obtained from searches for $\tilde{\chi}_1^+\ \tilde{\chi}_1^-$ events decaying directly and indirectly via the λ''_{223} ($\bar{U}\bar{D}\bar{D}$) couplings. Bounds indicate limits on the neutralino mass obtained by excluding chargino masses. The efficiency figures correspond to points that were selected after doing a fine scan in Fig. 5.6.

Limits

For $\tilde{\chi}_1^0\ \tilde{\chi}_2^0$, $\tilde{\chi}_1^0\ \tilde{\chi}_2^0$ and $\tilde{\chi}_1^+\ \tilde{\chi}_1^-$ decays via the $\bar{U}\bar{D}\bar{D}$ coupling, the derivation of the upper limit on the cross section at 95% confidence level and subsequent mass limits was carried out the same manner as that used for decays via $LL\bar{E}$ and $LQ\bar{D}$. Fig. 7.11 shows plots of the efficiency as a function of mass in the region where the absolute mass limit is obtained. The corresponding plots of σ_{95} superimposed over σ_{pr} to obtain the absolute mass limits of 25.9 GeV/c^2 for direct decays and 42.2 GeV/c^2 for indirect decays, are shown in Fig. 7.14. Tables 7.5 and 7.6 show the mass limit obtained in all regions of parameter space scanned for $\tilde{\chi}_1^0\ \tilde{\chi}_1^0$, $\tilde{\chi}_1^0\ \tilde{\chi}_2^0$ and $\tilde{\chi}_1^+\ \tilde{\chi}_1^-$ decays. The absolute limit is obtained in the region with the lowest mass limit.

Indirect decays gave better limits compared to direct decays (Fig. 7.15c) due to better sensitivity to signal resulting from higher production cross sections. The peaks are as a result of the difference in mass limits in the two separate regions of the low m_0 for the same $\tan\beta$.

The absolute mass limit was mapped onto the $\mu - M_2$ plane as illustrated in Figs. 7.16 and 7.17. In addition, limits obtained in the region $\tan\beta$: 20 — 50, were also mapped onto the $\mu - M_2$ plane. This is shown in Figs. 7.18 and 7.19. Apart from a small increase in the LEP I excluded gaugino mass region for $+\mu$, there are no significant differences in the distribution of the excluded $\mu - M_2$ regions at low $\tan\beta$ and high $\tan\beta$ for $m_0 = 60$ GeV/c^2. For $m_0 = 100$ GeV/c^2, the excluded area in the $\mu - M_2$ plane is larger at high $\tan\beta$ than at low $\tan\beta$.

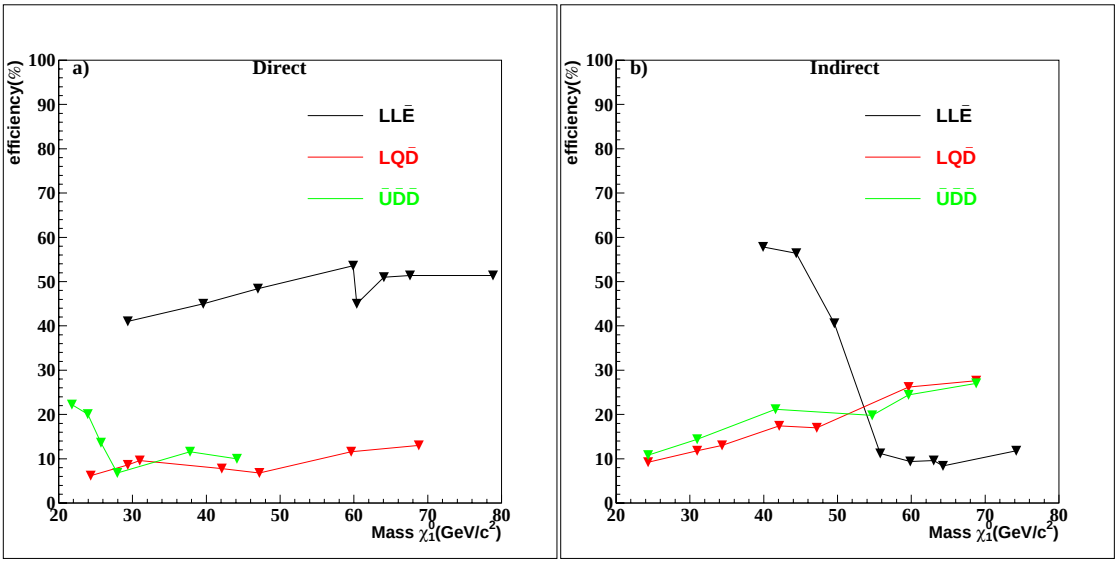

Figure 7.11: The efficiency as a function of mass for all points used to obtain the absolute mass limit for (a) direct decays and (b) indirect decays.

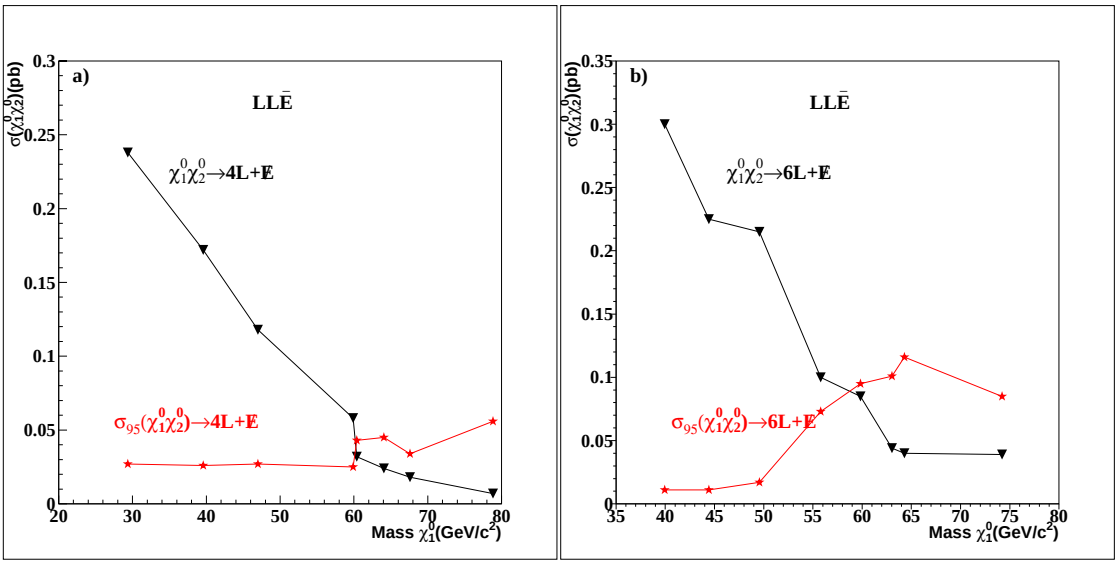

Figure 7.12: σ_{95} $(\tilde{\chi}_1^0\ \tilde{\chi}_2^0)$ superimposed over the production cross section $(\tilde{\chi}_1^0\ \tilde{\chi}_2^0)$ to obtain the absolute mass limits at (a) 60.2 GeV/c^2 for direct decays and (b) 58.2 GeV/c^2 for indirect decays. The efficiency results in Fig. 7.11 were used to derive σ_{95} $(\tilde{\chi}_1^0\ \tilde{\chi}_2^0)$.

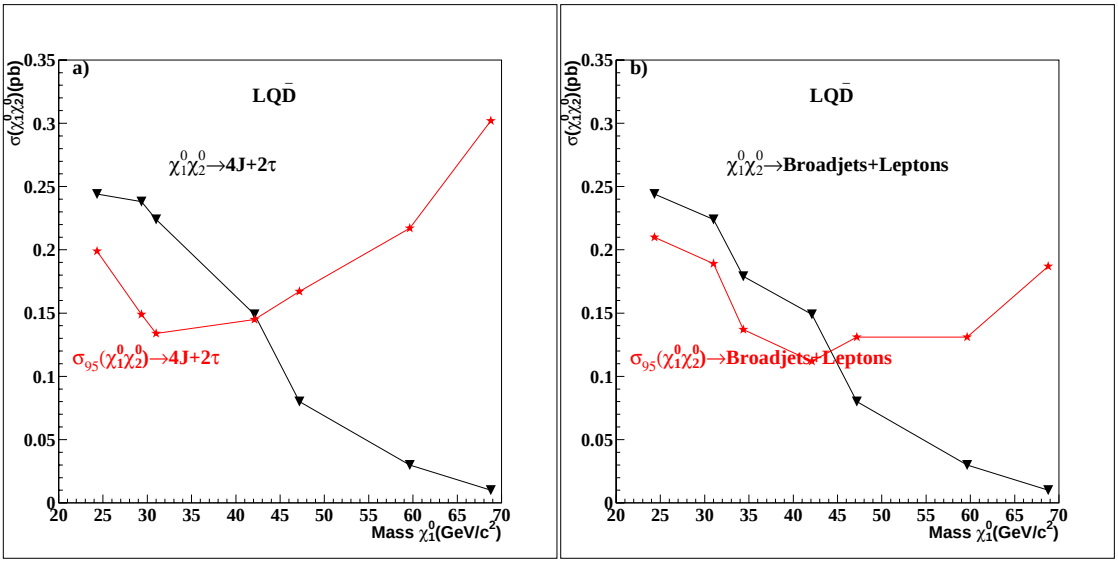

Figure 7.13: σ_{95} $(\tilde{\chi}_1^0\ \tilde{\chi}_2^0)$ superimposed over the production cross section $(\tilde{\chi}_1^0\ \tilde{\chi}_2^0)$ to obtain the absolute mass limits at (a) 42.3 GeV/c^2 for direct decays and (b) 44.2 GeV/c^2 for indirect decays. The efficiency results in Fig. 7.11 were used to derive σ_{95} $(\tilde{\chi}_1^0\ \tilde{\chi}_2^0)$.

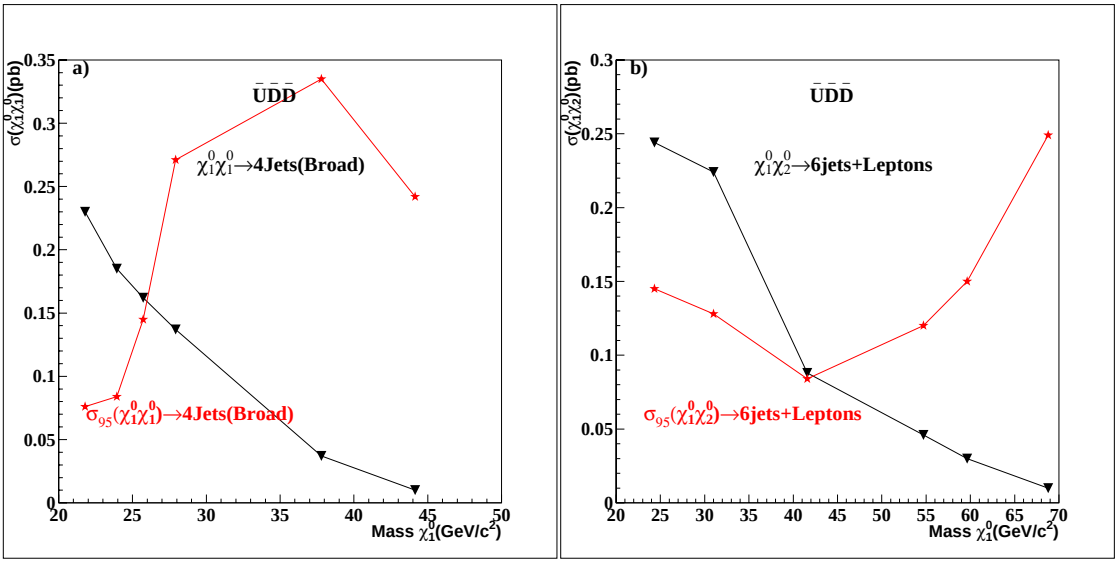

Figure 7.14: (a) σ_{95} $(\tilde{\chi}_1^0\ \tilde{\chi}_1^0)$ superimposed over the production cross section $(\tilde{\chi}_1^0\ \tilde{\chi}_1^0)$ to obtain the absolute mass limit at 25.9 GeV/c^2 for direct decays. The efficiency results in Fig. 7.11a were used to derive σ_{95} $(\tilde{\chi}_1^0\ \tilde{\chi}_1^0)$ (b) σ_{95} $(\tilde{\chi}_1^0\ \tilde{\chi}_2^0)$ superimposed over the production cross section $(\tilde{\chi}_1^0\ \tilde{\chi}_2^0)$ to obtain the absolute mass limit at 42.2 GeV/c^2 for indirect decays. The efficiency results in Fig. 7.11b were used to derive σ_{95} $(\tilde{\chi}_1^0\ \tilde{\chi}_2^0)$.

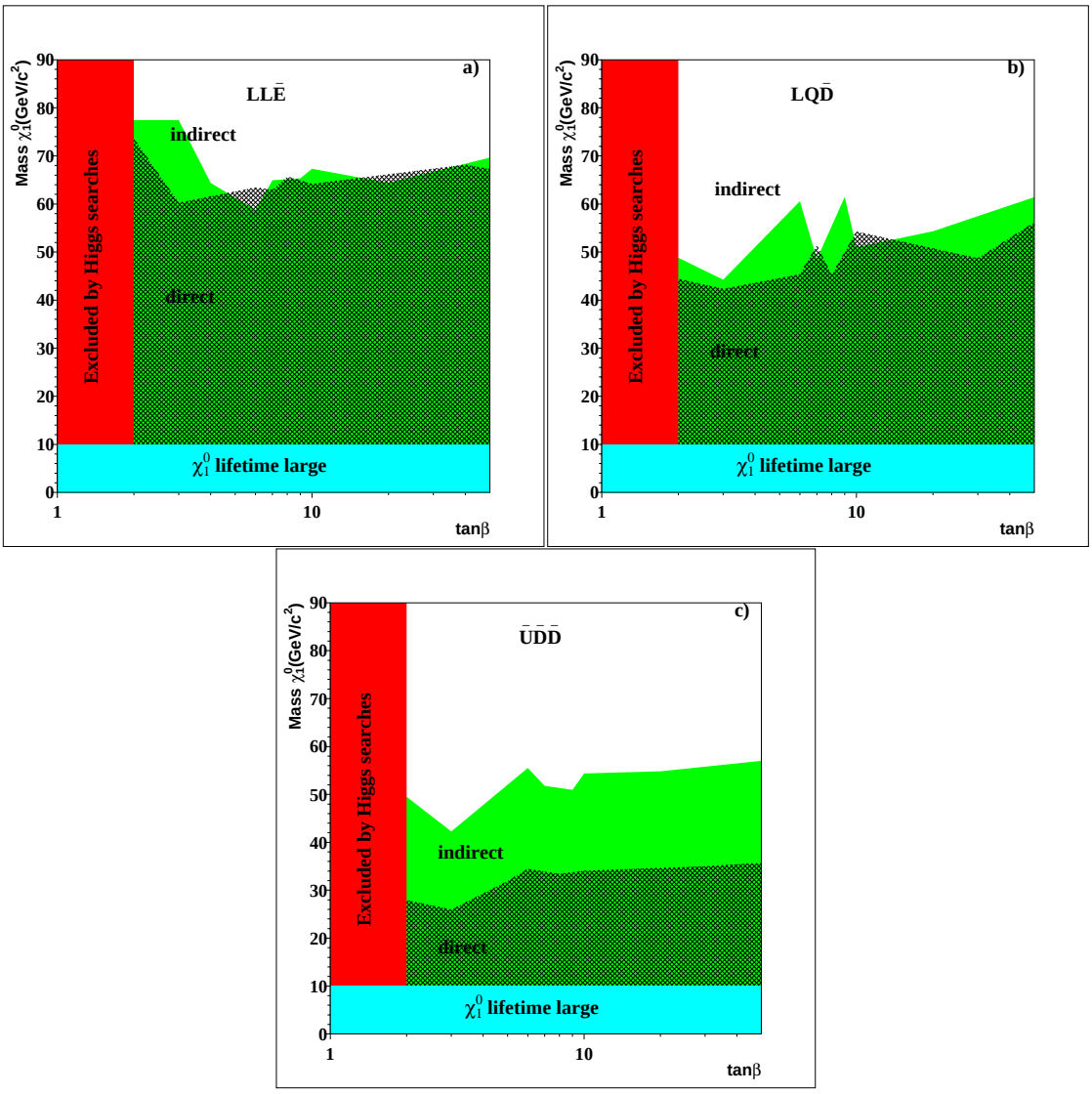

Figure 7.15: The lightest neutralino mass as a function of $\tan\beta$ for regions of parameter space in which the limits were obtained for decays via $LL\bar{E}$, $LQ\bar{D}$ and $\bar{U}\bar{D}\bar{D}$ couplings respectively. In this analysis, the neutralino is restricted to a sensitivity of $\gtrsim 10\,\mathrm{GeV}/c^2$ as explained in section 4.1. $\tan\beta$ is also restricted to a lower limit of $\gtrsim 2$ as explained in section 5.1.

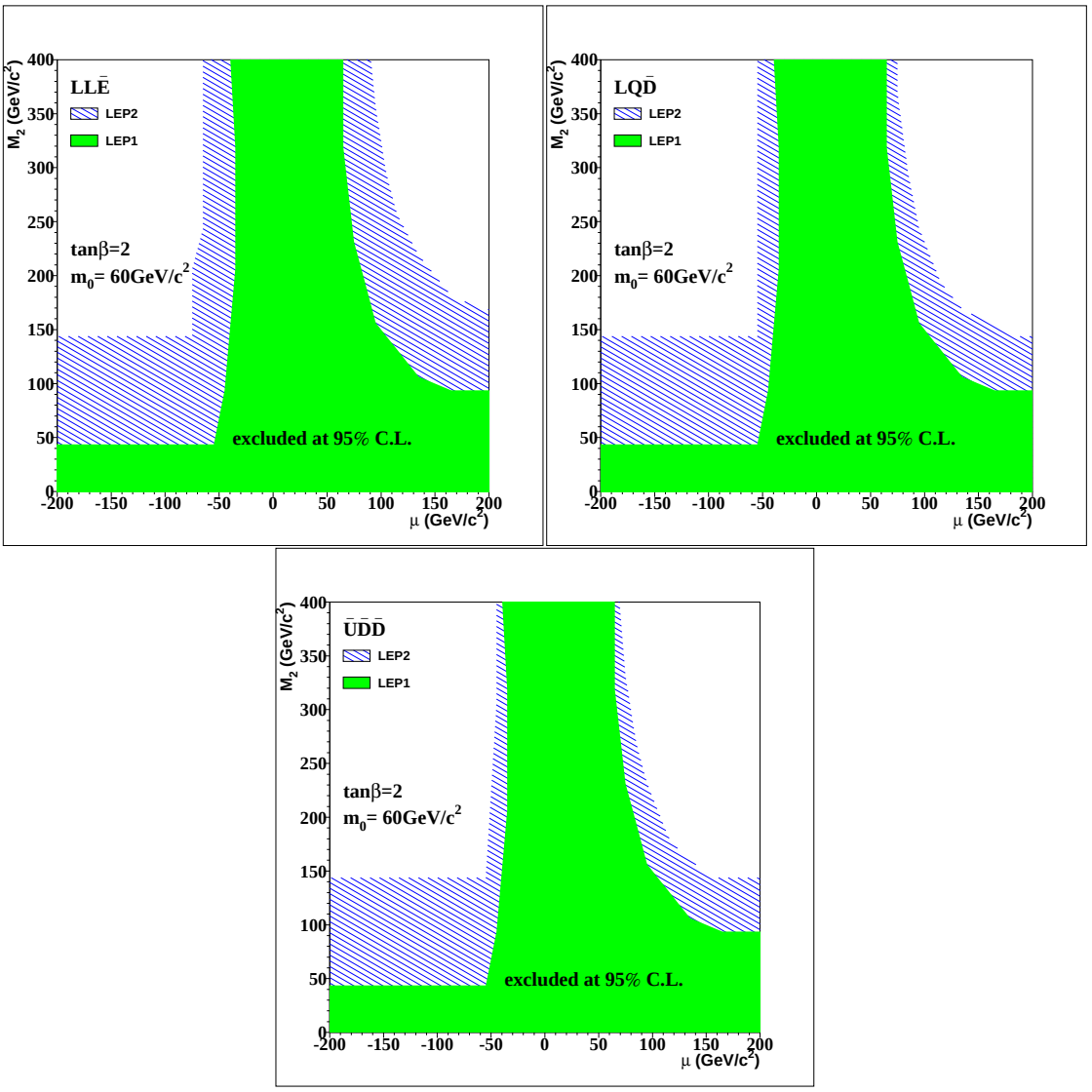

Figure 7.16: The regions in the (μ, M_2) plane excluded at 95% C.L. at $\tan\beta = 2$ and $m_0 = 60$ GeV/c^2 for each of the three R-parity violating operators using the neutralino mass limits of 60.2 GeV/c^2 ($LL\bar{E}$), 44.2 GeV/c^2 ($LQ\bar{D}$) and 42.2 GeV/c^2 ($\bar{U}\bar{D}\bar{D}$) respectively.

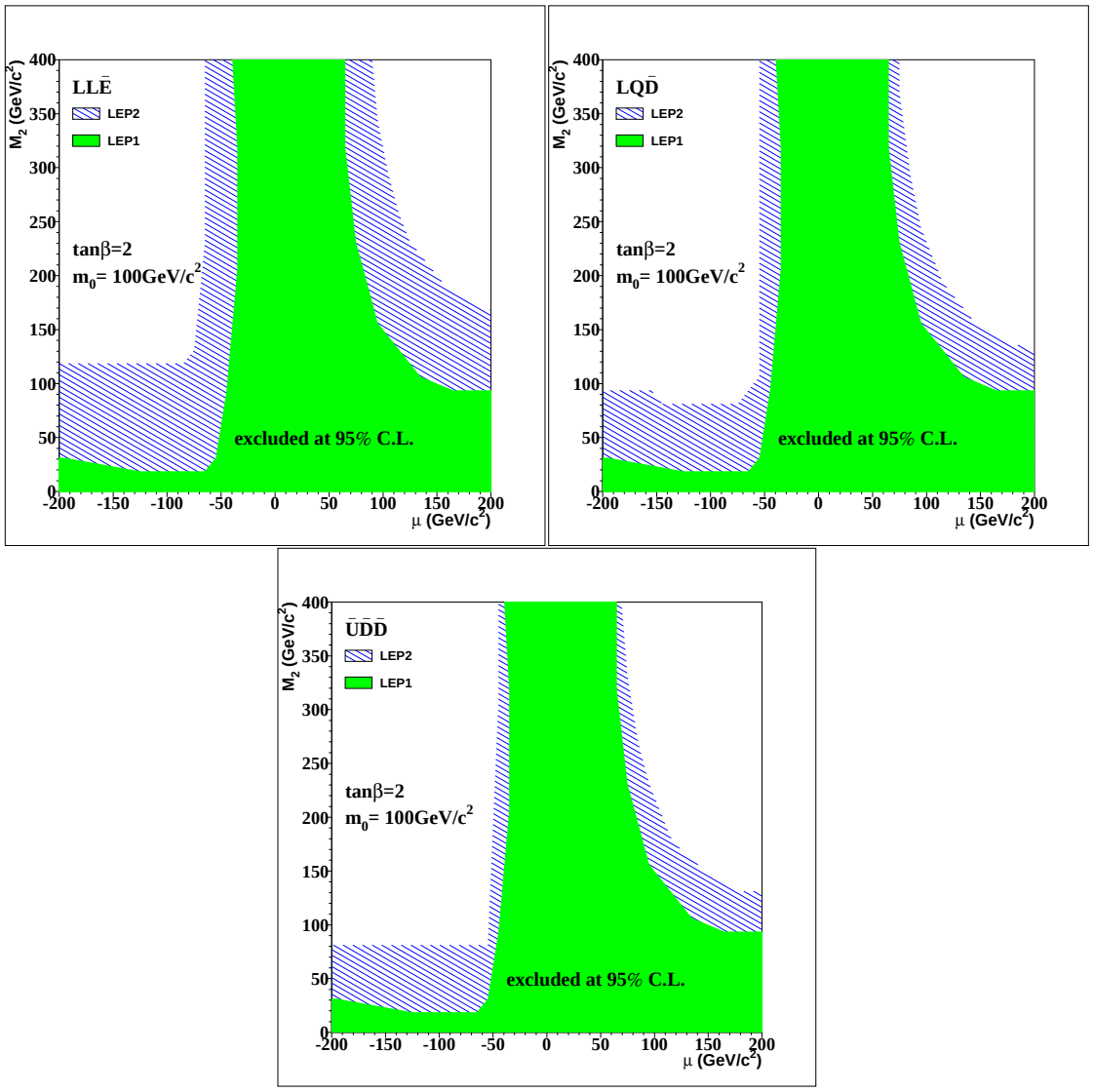

Figure 7.17: The regions in the (μ, M_2) plane excluded at 95% C.L. at $\tan\beta = 2$ and $m_0 = 100$ GeV/c^2 for each of the three R-parity violating operators using the neutralino mass limits of 60.2 GeV/c^2 ($LL\bar{E}$), 44.2 GeV/c^2 ($LQ\bar{D}$) and 42.2 GeV/c^2 ($\bar{U}\bar{D}\bar{D}$) respectively.

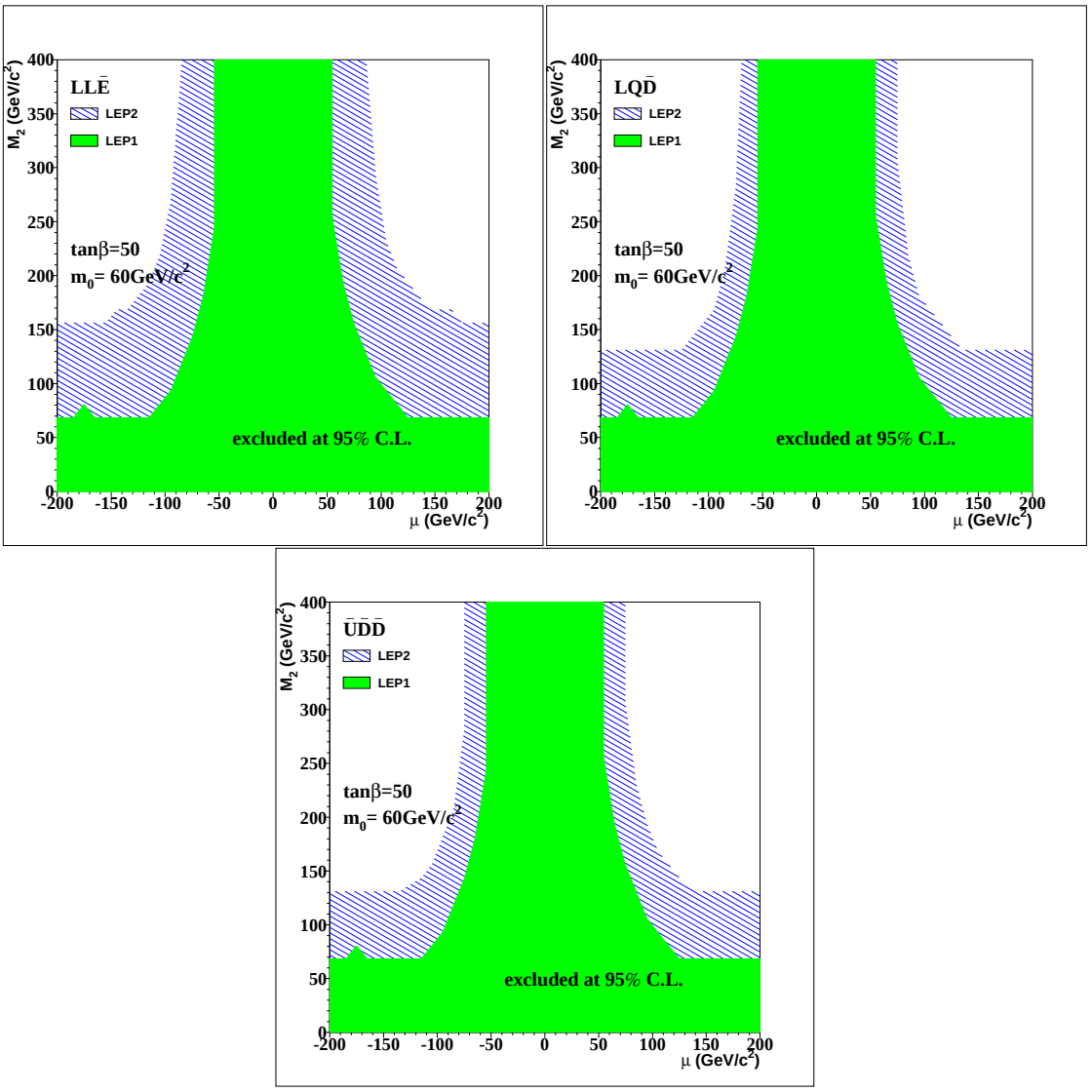

Figure 7.18: The regions in the (μ, M_2) plane excluded at 95% C.L. at $\tan\beta = 50$ and $m_0 = 60$ GeV/c^2 for each of the three R-parity violating operators using the neutralino mass limits of 69.6 GeV/c^2 ($LL\bar{E}$), 54.3 GeV/c^2 ($LQ\bar{D}$) and 54.8 GeV/c^2 ($\bar{U}\bar{D}\bar{D}$) respectively.

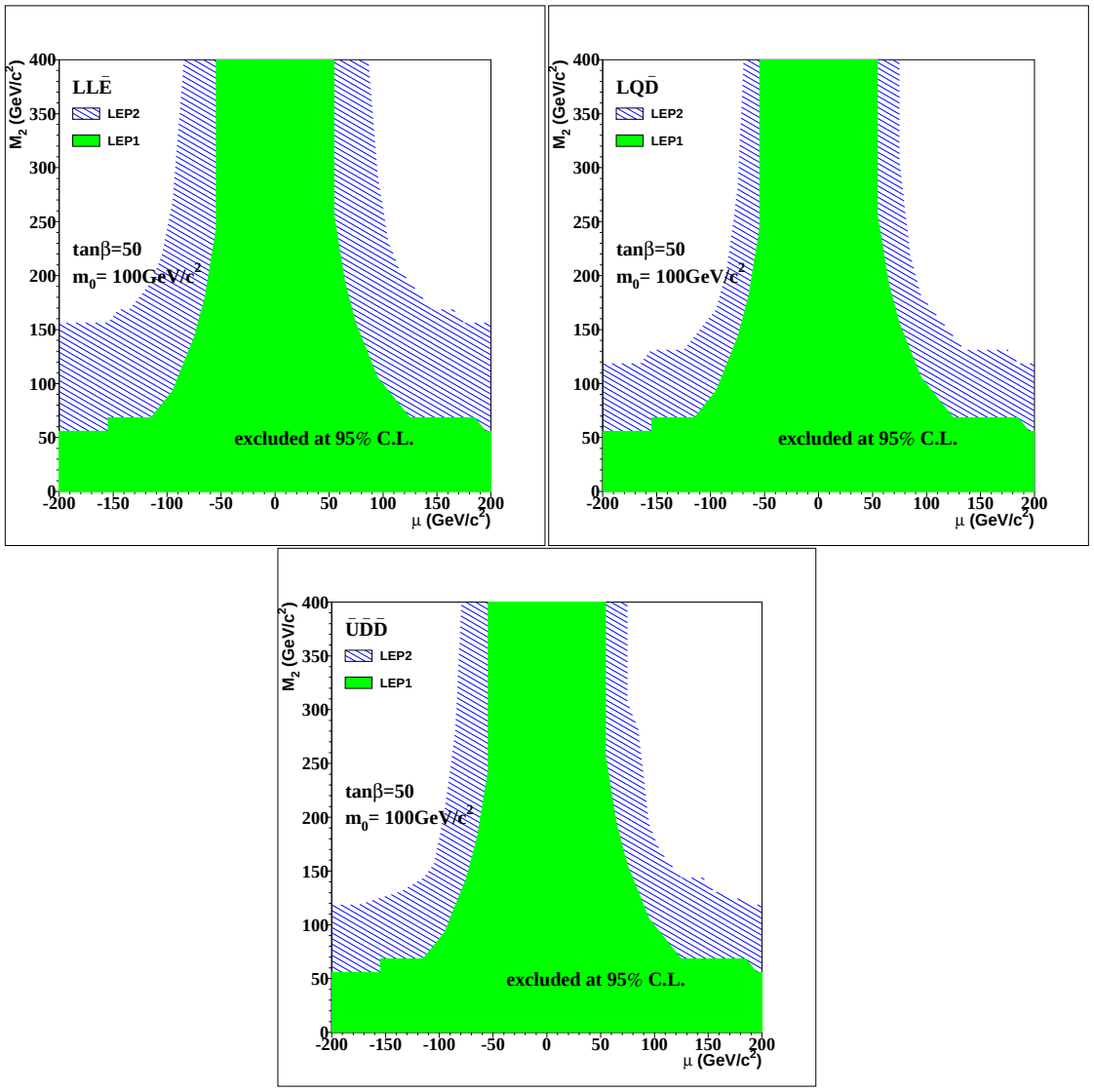

Figure 7.19: The regions in the (μ, M_2) plane excluded at 95% C.L. at tanβ = 50 and m_0 = 100 GeV/c^2 for each of the three R-Parity violating operators using the neutralino mass limits of 69.6 GeV/c^2 ($LL\bar{E}$), 54.3 GeV/c^2 ($LQ\bar{D}$) and 54.8 GeV/c^2 ($\bar{U}\bar{D}\bar{D}$) respectively.

Chapter 8

Conclusions

The objective of this analysis was to carry out searches for an LSP which decays via an R-parity violating $LL\bar{E}$, $LQ\bar{D}$ or $\bar{U}\bar{D}\bar{D}$ coupling and in the absence of signal, to constrain parameter space by obtaining a mass limit for the LSP. A number of searches were used to extract signal from topologies resulting from the decay of supersymmetric particles via the $LL\bar{E}$, $LQ\bar{D}$ and $\bar{U}\bar{D}\bar{D}$ couplings. The searches were run over data collected by the ALEPH detector from e^+e^- collisions at centre-of-mass energies between $189\,\mathrm{GeV}/c^2$ and $208\,\mathrm{GeV}/c^2$ with an integrated luminosity of $628.3\mathrm{pb}^{-1}$. No evidence of signal was found and limits were obtained at 95% confidence level. A number of assumptions were made while implementing the searches.

- Only one λ_{ijk} coupling is non-zero at any one time.
- The LSP candidates are the neutralino, the sneutrino and the slepton.
- The LSP has a negligible lifetime and this restricts the sensitivity of the searches to neutralino masses of $\gtrsim 10\,\mathrm{GeV}/c^2$.
- There is no mixing between direct and indirect decay modes.
- All limits are set within the MSSM framework.

LSP Mass Limit		
Coupling	Decay Mode	
	Direct $\tilde{\chi}_1^0$ (GeV/c^2)	Indirect $\tilde{\chi}_1^0$ (GeV/c^2)
$LL\bar{E}$	60.2	58.7
$LQ\bar{D}$	42.3	44.2
$\bar{U}\bar{D}\bar{D}$	25.9	42.2

Table 8.1: The absolute mass limits for the lightest neutralino which decays via $LL\bar{E}$, $LQ\bar{D}$ and $\bar{U}\bar{D}\bar{D}$ couplings. Limits are valid for all μ, $\tan\beta$, m_0 and M_2.

- The gauge unification condition holds.

In this chapter, the limits obtained are summarized.

8.1 Summary

The implementation of limits from the Z width, sfermion and gaugino searches (section 5.1), show that the lightest neutralino is the only LSP candidate. The absolute mass limits obtained from neutralino searches described in chapter 7, are given in Table 8.1. Using the limit of 60.2 GeV/c^2, a bound of 71.9 GeV/c^2 was obtained on the mass of the lightest chargino, i.e. all points in parameter space are excluded for chargino masses less than 71.9 GeV/c^2. Such limits obtained are valid for all μ, $\tan\beta$, m_0 and M_2. Chargino searches were carried out and the absolute mass limits obtained are given in Table 8.2. These results were used to set a bound of 50.9 GeV/c^2 on the mass of the lightest neutralino at high m_0. This implies that at high m_0 all points in parameter space are excluded for neutralino masses less than 50.9 GeV/c^2. Chargino searches were not carried out at low m_0 since the purpose of this analysis was to carry out searches for the LSP for which the neutralino is the only candidate. Chargino searches are only necessary to set bounds on the mass of the neutralino because at high m_0, the neutralino cross section is low. This makes it insensitive to signal.

Coupling	Decay Mode		Bound
	Direct	Indirect	
	$\tilde{\chi}_1^{\pm}$ (GeV/c^2)	$\tilde{\chi}_1^{\pm}$ (GeV/c^2)	$\tilde{\chi}_1^0$ (GeV/c^2)
$LL\bar{E}$	102.7	102.7	50.9
$LQ\bar{D}$	101.8	102.3	50.9
$\bar{U}\bar{D}\bar{D}$	101.3	101.9	50.9

Table 8.2: The absolute mass limits for the lightest chargino which decays via $LL\bar{E}$, $LQ\bar{D}$ and $\bar{U}\bar{D}\bar{D}$ couplings. Bounds indicate limits on the neutralino mass obtained by excluding chargino masses. The limits and bounds are valid for all μ, $\tan\beta$, M_2 and $m_0 \geq 200\,\mathrm{GeV}/c^2$.

Bibliography

[1] D. E. Groom et al., Particle Data Group, Eur. Phys. Jour. **C15** (2000) 1.

[2] For elementary introductions to particle physics, see: D. Griffiths, *"Introduction to Elementary Particles"*, John Wiley and Sons, 1987;
F. Halzen and A. D. Martin, *"Quarks and Leptons: An Introductory Course in Modern Particle Physics"*, John Wiley and Sons, 1984.

[3] P. W. Higgs, Phys. Lett. **12** (1964) 132;
F. Englert and R. Brout, Phys. Rev. Lett. **13** (1964) 321;
G. S. Guralnik, C. R. Hagen and T. W. Kibble, Phys. Rev. Lett. **13** (1964) 585.

[4] S. Glashow, Nucl. Phys. **B22** (1961) 579;
A. Salam in *"Elementary Particle Theory"*, ed. N. Svartholm (1968) 367;
S. Weinberg, Phys. Rev. Lett. **419** (1967) 1264.

[5] H. P. Nilles in *"Phenomenological Aspects of Supersymmetry"*, eds. W. Hollick, R. Ruckl and J. Wess. Proceedings: Munich, Springer-Verlag (1991).

[6] H. P. Nilles, Phys. Rep. **110** (1984) 1.

[7] E. Farhi and L. Susskind, Phys. Rep. **74** (1981) 277.

[8] N. Arkani-Hamed, S. Dimopoulos, and G. Dvali, Phys. Lett. **B429** (1998) 263.

I. Antoniadis, N. Arkani-Hamed, S. Dimopoulos, and G. Dvali, Phys. Lett. **B436** (1998) 257.

[9] J. F. Gunion, *"A Simplified Summary of Supersymmetry"*, hep-ph/9704349.

[10] J. L. Lopez, D. V. Nanopoulos and A. Zichichi, Prog. Part. Nucl. Phys. **33** (1994) 303.

[11] G. G. Ross, *"Grand Unified Theories"*, Frontiers in Physics 60, Benjamin Cummings, (1984).

[12] G. Börner, *"The Early Universe"*, Springer Verlag (1991).

[13] W. de Boer, Prog. Part. Nucl. Phys. **33** (1994) 201.

[14] H. Murayama, *"Supersymmetry Phenomenology"*, hep-ph/0002232.

[15] P. Fayet, Phys. Lett. **B64** (1976) 159;
P. Fayet, Phys. Lett. **B69** (1977) 489;
for modern reviews see, M. Drees, *"An Introduction to Supersymmetry"*, hep-ph/9611409 and J. A. Bagger, *"Weak Scale Supersymmetry: Theory and Practice"*, hep-ph/9604232.

[16] M. Kaku, *"Quantum Field Theory: A Modern Introduction"*, Oxford University Press, (1993).

[17] E. Accomando et al., in *"Physics at LEP2"*, Volume 1, eds. G. Altarelli, T. Sjostrand and F. Zwirner, CERN 96-01;
J. F. Gunion, H. E. Haber, G. L. Kane and S. Dawson, *"The Higgs Hunters Guide"*, Addison-Wesley, 1990.

[18] M. Drees, *"An Introduction to Supersymmetry"*, hep-ph/9611409.

[19] J. L. Lopez, Rep. Prog. Phys. **59** (1996) 819.

[20] S. P. Martin, *"A Supersymmetry Primer"*, hep-ph/9709356.

[21] A. Bartl, H. Fraas, W. Majerotto and B. Mosslächer, Z. Phys. **C55** (1992) 257.

[22] H. E. Haber and G. L. Kane, Phys. Rep. **117** (1985) 75.

[23] C. Kounnas et al., Phys. Lett. **B132** (1983) 95;
L. J. Hall, J. Polchinski, Phys. Lett. **B152** (1985) 335;
H. C. Cheng, L. J. Hall, LBL-35950, UCB-PTH-94/21 (1994);
L. E. Ibanez, C. Lopez, Nucl. Phys. **B233** (1984) 511;
L. E. Ibanez, C. Lopez, C. Munoz, Nucl. Phys. **B256** (1985) 218;
J. Ellis, F. Zwirner, Nucl. Phys. **B338** (1990) 317.

[24] G. Farrar, P. Fayet, Phys. Lett. **B76** (1978) 575.

[25] H. Dreiner *"An Introduction to Explicit R-Parity Violation"*, hep-ph/9707435.

[26] J. L. Goity, Marc Sher, Phys. Lett. **B346** (1995) 69;
erratum-ibid. Phys. Lett. **B385** (1996) 500.

[27] J. Ellis, J. S. Hagelin, D. V. Nanopoulos, K. Olive and M. Srednicki, Nucl. Phys. **B238** (1984) 453.

[28] The LEP collaborations *"combination of Preliminary Electroweak Measurements and Constraints on the Standard Model"* CERN-EP-2001-021.

[29] D. Buskulic et at., ALEPH collaboration, Nucl. Instr. Meth. **A360** (1995) 481.

[30] D. Decamp et al., ALEPH collaboration, Nucl. Instr. Meth. **A294** (1990) 121.

[31] D. Creanza et al., Nucl. Instr. Meth. **A409** (1998) 157.

[32] D. Decamp et, al,. ALEPH Collaboration, Z. Phys. **C54** (1992) 211.

[33] G. J. Barber et, al,. Nucl. Instr. Meth. **A270** (1989) 212.

[34] D. Buskulic et al., ALEPH Collaboration, Nucl. Instr. Meth. **A346** (1994) 461.

[35] E. Longo and I. Sestili, Nucl. Instr. Meth. **A128** (1987) 283.

[36] See *"Final* 2000 *Run Selection and Luminosity"*, in http://alephwww.cern.ch/ sical/Wlumi/.

[37] J. Knobloch, E. Lançon *"JULIA User's Guide and ALEPH Programmers hints"*, http://alephwww.cern.ch/ALEPHGENERAL/jul/doc/html/julia.html.

[38] V. Blobel, *" The BOS System"* II Institut für Experimentalphysik Universität Hamburg 2001, http://alephwww.cern.ch/LIGHT/BosManualHome.html.

[39] B. Bloch-Devaux, *"KINGAL User's Guide"*, ALEPH-91-082, PHYSIC 91-075; B. Bloch-Devaux, *"KINLIB Documentation"*, ALEPH-91-078, PHYSIC 91-071.

[40] T. J. Sjöstrand, Comp. Phys. Comm **82** (1994) 74.

[41] E. Barberio, B. van Eijk and Z. Wąs, Comp. Phys. Comm. **66** (1991) 115.

[42] F. Ranjard, *"GALEPH User's Guide"*, ALEPH note # 119, version # 9, March 1995.

[43] R. Brun et al., *"GEANTS3"*, CERN-DD/EE/84-1 (1987).

[44] S. Katsanevas and P. Morawitz, *"SUSYGEN 2.2 - A Monte Carlo event generator for MSSM sparticle production at e^+e^- colliders"*, Comp. Phys. Comm. **112** (1998) 227-269.

[45] S. Jadach, W. Placzek and B. F. L. Ward, Phys. Lett. **B390** (1997) 298.

[46] S. Jadach and Z. Wąs, Comp. Phys. Comm. **36** (1985) 191.

[47] J. A. M. Vermaseren in *"Proceedings of the IVth International Workshop on Gamma Gamma Interactions"*, eds. G. Cochard and P. Kessler, Springer Verlag, 1980.

[48] M. Skrzypek, S. Jadach, W. Placzek and Z. Wąs, Comm. Phys. Comm. **94** (1996) 216.

[49] *"The PYTHIA 5.7 and JETSET 7.4 manual"*, Comp. Phys. Comm. **82** (1994) 74.

[50] G. Bhattacharyya, Nucl. Phys. Proc. Suppl. **A52** (1997) 83.

[51] I. Hinchcliffe and T. Kaeding, Phys. Rev. **D47** (1992) 279.

[52] A. Y. Smirnov and F. Vissani, Phys. Lett. **B 380** (1996) 317.

[53] B. C. Allanach, A. Dedes and H. K. Dreiner, *"Bounds on R-parity Violating Couplings at the Weak Scale and at the GUT Scale"*, hep-ph/9906209.

[54] B. C. Allanach et al., *"Searching for R-parity at Run-II of the Tevatron"*, hep-ph/9906224.

[55] V. Barger, G. F. Giudice, T. Han, Phys. Rev. **D40**, (1989) 2987.

[56] R. M. Godbole, R. P. Roy and X. Tata, Nucl. Phys. **B401** 67.

[57] M. Hirsch, H. V. Klapdor-Kleingrothaus and S. G. Kovalenko, Phys. Rev. Lett. **75** (1995) 17;
M. Hirsch, H. V. Klapdor-Kleingrothaus and S. G. Kovalenko, Phys. Rev. **D53** (1996) 1329.

[58] S. C. Bennett, C.E. Wieman, Phys. Rev. Lett. **82** (1999) 2484.

[59] J. Ellis, G. Bhattacharyya and K. Sridhar, Mod. Phys. Lett. **B355** (1995) 193.

[60] F. Zwirner, Phys. Lett. **B132** (1983) 103.

[61] G. Bhattacharyya, D. Choudhury and K. Sridhar, Phys. Lett. **B355** (1995) 193.

[62] ALEPH Collaboration, Eur. Phys. Jour. **C4** (1998) 433.

[63] ALEPH Collaboration, Eur. Phys. Jour. **C13** (2000) 29.

[64] DELPHI Collaboration, Eur. Phys. Jour. **C13** (2000) 591.

[65] OPAL Collaboration, Eur. Phys. Jour. **C11** (1999) 619.

[66] OPAL Collaboration, Eur. Phys. Jour. **C12** (2000) 1.

[67] L3 Collaboration, Phys. Lett. **B414** (1997) 373.

[68] L3 Collaboration Phys. Lett. **B459** (1999) 354.

[69] ALEPH Collaboration, Eur. Phys. Jour. **C19** (2001) 415.

[70] ALEPH Collaboration, *"Search for Supersymmetric Particles with R-Parity Violating Decays in* e^+e^- *Collisions at Centre-of-Mass energies up to 209 GeV"*, CERN-EP-2002-071.

[71] D. Bardin et al., Z. Phys. **C44** (1989) 493;
D. Bardin et al., Comp. Phys. Comm. **59** (1990) 303;
D. Bardin et al., Nucl. Phys. **B351** (1991) 1;
D. Bardin et al., Phys. Lett. **B255** (1991) 290 and CERN-TH 6443/92 (MAY 1992); DESY Report 99-070, hep-ph/9908433 (1999).

[72] CDF Collaboration, W. Tao, *"t Mass at CDF"*, talk presented at ICHEP 98, Vancouver, B.C., Canada, 23-29 July 1998.

[73] The Top Averaging Group, L. Demortier et al., for the CDF and DØ Collaborations, FERMILAB-TM-2084 (1999).

[74] B. Abbott et al., DØ Collaboration, Phys. Rev. Lett. **84** (2000) 222.

[75] D. Buskulic et al., ALEPH collaboration, Phys. Lett. **B349** (1995) 238.

[76] H. Albrecht, E. Blucher, J. Boucrot, *"ALPHA Users's Guide, Versions* $\geq$ 125*"*, Tech. Rep. ALEPH-99-087 (1999).

[77] *"HBOOK user guide: CERN computer center program library long writeup: version 4.22"* http://wwwinfo.cern.ch/asdoc/hbook_html3/hboomain.html.

[78] A. Heister et al., ALEPH Collaboration, Phys. Lett. **B526** (2002) 191.

[79] A. Bartl, H. Fraas, W. Majerotto, Z. Phys. **C30** (1986) 411;
A. Bartl, H. Fraas, W. Majerotto, Z. Phys. **C34** (1987) 411:
A. Bartl, H. Fraas, W. Majerotto, Z. Phys. **C41** (1988) 475;
A. Bartl, H. Fraas, W. Majerotto, Nucl. Phys. **B278** (1986) 1;
A. Bartl, H. Fraas, W. Majerotto, Z. Phys. **C55** (1992) 257.

[80] H. Dreiner and P. Morawitz, Nucl. Phys. **B428** (1994) 31;
H. Dreiner, S. Lola, P. Morawitz, Phys. Lett. **B389** (1996) 62.

[81] ALEPH collaboration, Euro. Phys. Jour. **C7** (1999) 383.

[82] S. Bethke et al., JADE collaboration, Phys. Lett. **B213** (1988) 235.

[83] W. J. Stirling in Proceedings of the Durham Workshop, 1990, Ed. M.R. Pennington, DTP 91-04;
N. Brown and W. J. Stirling, Phys. Lett. **B252** (1990) 657;
S. Bethke et al., Nucl. Phys. **370** (1992) 310.

[84] R. Barate et al., ALEPH collaboration, Phys. Rep. **294** (1998) 1.

[85] O. Awunor, *"Limit on the LSP mass in R-parity Violating Supersymmetric Scenario"*, ALEPH-NOTE-2001-063.